Luminescence from lanthanide ions and the effect of co-doping in silica and other hosts

by

Hassan Abdelhalim Abdallah Seed Ahmed

M.Sc.

A thesis submitted in fulfilment of the requirement for the degree

PHILOSOPHIAE DOCTOR

in the

Department of Physics

Faculty of Natural and Agricultural Sciences

at the

University of the Free State

***Supervisor*: Dr. R.E. Kroon**

***Co-supervisor*: Prof O.M. Ntwaeaborwa**

***Date*: July 2012**

ACKNOWLEDGEMENTS

The author wishes to thank the following individuals and institutions:

- My supervisor Dr RE Kroon who has supported me throughout my thesis with his patience and knowledge.
- My co-supervisor Prof OM Ntwaeaborwa for providing advice when I needed it.
- Prof HC Swart for giving me opportunity to come here, suggesting the problems and giving useful recommendations.
- Prof WD Roos for discussing the XPS principles and helping me to use the XPS spectrometer.
- The phosphor group at the Free State University for their good discussion.
- Ms MM Duvenhage for assistance with CL and FTIR measurements.
- Dr Liza Coetzee for measuring XPS and Auger spectra and SEM images.
- Prof RJ Botha and his crew from the Nelson Mandela Metropolitan University for their technical support during using their PL system.
- The experimental station SUPERLUMI for their equipment facilities.
- Dr Weon-Sik Chae from Korea Basic Science Institute for performing the lifetime measurements.
- Prof L Venter for reviewing some part of my thesis.
- The NRF for financial assistance.

ABSTRACT

Amorphous silica powders doped with lanthanide ions were synthesised by the sol-gel method and their cathodoluminescence (CL) and photoluminescence (PL) emissions were compared. Interesting differences depending on the type of excitation were observed for Tb and Ce-doped samples. For Tb-doped samples blue $^5D_3 \rightarrow {}^7F_J$ emission was measured during CL in samples for which PL results showed this emission to be concentration quenched due to cross-relaxation, while for Ce-doped samples luminescence occurred for CL but not during PL measurements. Unlike the other lanthanides, Tb and Ce ions are sometimes found in the tetravalent rather than the trivalent state, and these differences were attributed to the possibility of electron capture of tetravalent ions possible during CL but not PL.

A scheme for the energy levels of divalent and trivalent lanthanide ions relative to the conduction and valence bands in silica was proposed, making use of experimental data and the known relative positions of the energy levels for the lanthanides. Although the location of the divalent europium ion f-level above the valence band can be located by using the charge transfer energy of trivalent europium, this process cannot be generalized to find the location of the trivalent cerium ion f-level above the valence band using the charge transfer energy of tetravalent cerium as has been suggested.

Initial investigations of the luminescence properties of Ce doped silica were complicated by overlapping luminescence from oxygen deficiency defects from the host itself and the fact that Ce took the tetravalent state which is nonluminescent for PL measurements. Spectra obtained using a wide variety of excitation methods, including synchrotron radiation, were compared and evaluated in the light of previously published data. Radically improved results were obtained by annealing in a reducing atmosphere instead of air. X-ray photoelectron spectroscopy as well as ultraviolet reflectance spectroscopy provided evidence of the conversion of Ce from the tetravalent to trivalent state and this was accompanied by strong luminescence of these sample during PL measurements.

Ce,Tb co-doped silica was used to study the energy transfer from Ce to Tb ions. Initial results were disappointing when measurements showed that adding Ce quenched the Tb emission intensity instead of increasing it. However, after annealing the samples in a reducing atmosphere, a quantum efficiency of 97% for energy transfer from Ce to Tb was achieved. The mechanism for energy transfer was investigated by comparing experimental measurements of the changes in donor (Ce) emission intensity and lifetime as a function of the amount of acceptor (Tb) with numerical simulations of various models. Measurements correlated well to models for dipole-dipole and exchange interactions, but the critical transfer distance obtained was not appropriate for the exchange interaction, hence dipole-dipole interaction was identified as the interaction mechanism.

Nanocrystalline LaF_3 powders were synthesized by the hydrothermal method and strong luminescence was obtained from samples doped with Ce and Tb. Photoluminescence spectra from co-doped samples revealed that the emission from Ce was quenched and the emission from Tb was enhanced, showing that energy transfer from Ce to Tb occurred. The energy transfer mechanism was investigated in a similar way as for the silica samples, but in this case the experimental results fitted models for the quadrupole-quadrupole and exchange interactions. Much higher concentrations of Tb were required to significantly affect the Ce luminescence properties than in the case for silica, and the critical transfer distance obtained was appropriate for the exchange interaction. Either or both of these interaction mechanisms are therefore possible. The results show that the interaction mechanism for energy transfer between lanthanide ions depends not only on the ions themselves, but also on the lattice hosting them.

KEYWORDS AND ACRONYMS

Phosphor, silica, sol-gel, lanthanum fluoride, hydrothermal, lanthanides, cerium, terbium, annealing, photoluminescence, cathodoluminescence, energy levels, cross-relaxation, energy transfer, interaction mechanism.

***A* (*A**)**	Acceptor (Excited acceptor)
AES	Auger electron spectroscopy
BE	Binding energy
CCD	Charge coupled device
CHA	Concentric hemispherical analyser
CL	Cathodoluminescence
CTAB	Cetyltrimethylammonium bromide
***D* (*D**)**	Donor (Excited donor)
DESY	Deutsches Elektronen-Synchrotron
FWHM	Full width at half maximum
FTIR	Fourier transform infrared spectroscopy
ICDD	International Centre for Diffraction Data
IR	Infrared
JCPDS	Joint Committee on Powder Diffraction Standards
KE	Kinetic energy
OH	Hydroxyl
OR	Alkoxide
PDF	Powder Diffraction Files
PL	Photoluminescence
SEM	Scanning Electron Microscope or Microscopy
TEOS	Tetraethylorthosilicate
UHV	Ultra high vacuum
UV	Ultraviolet
UV-Vis	Ultraviolet-visible
XPS	X-ray photoelectron spectroscopy
XRD	X-ray diffraction

TABLE OF CONTENTS

Chapter I: Introduction

Chapter II: Background information regarding phosphors

Chapter III: Theory of energy transfer

Chapter IV: Research techniques

Chapter V: Photoluminescence and cathodoluminescence from lanthanide doped sol-gel silica

Chapter VI: $^5D_3 \rightarrow ^7F_J$ emission of Tb doped sol-gel silica

Chapter VII: The impurity levels of lanthanide ions in silica

Chapter VIII: Luminescence from Ce in sol-gel SiO_2

Chapter IX: Effect of annealing on Ce^{3+}/Ce^{4+} ratio measured by XPS in luminescent SiO_2:Ce

Chapter X: High efficiency energy transfer in Ce,Tb co-doped silica

Chapter XI: Interaction mechanism for energy transfer from Ce to Tb ions in silica

Chapter XII: Luminescence from Ce and Tb in LaF_3 and the energy transfer mechanism in Ce,Tb co-doped LaF_3

Chapter XIII: Summary and conclusion

Chapter I

Introduction

1. Overview

Phosphors are used in many applications such as lighting, displays, lasers and scintillators. In most cases phosphors are based on luminescent centres, called dopants or activators, located in wide-bandgap hosts. Generally, host materials should exhibit good optical, mechanical and thermal properties [1]. There are many types of hosts, such as alkali-earth sulphides, alkali-earth aluminates, rare-earth oxides, oxysulfides, lanthanides halides, silicates etc. These hosts are solid inorganic compounds that can be classified into three categories, namely crystals, amorphous materials and materials that incorporate the properties of both (glass ceramics).

Lanthanide group ions are usually used as luminescent centres [2]. A specific feature of these ions is the presence of an internal partially filled 4f electron shell, giving various electron transitions in the UV, visible and IR regions of spectrum. The outer filled 5s and 5p levels shield the 4f electrons from the host environment so that the transitions between the 4f states (and therefore the luminescence wavelengths) are relatively insensitive to the host.

Energy transfer can play an important role in phosphors. The luminescence efficiency of a phosphor can be enhanced by co-doping with a second kind of dopant (donor) as a result of energy transfer from the donor to the acceptor. The excited centre can be relaxed by direct or indirect energy transfer to the acceptor [3]. In the direct mechanism, the energy transfers directly from the donor to the acceptor by multipole interaction or exchange interaction. For the indirect mechanism there are many scenarios such as energy transfer by cooperative effects (these include such phenomena as simultaneous energy transfer from two ions to another, transfer of part of one ion's excitation energy to another ion with the energy difference being emitted as a photon (or phonon), and the inverses of these processes), or by diffusion among the donor ions until the energy

acceptor is reached. Many theoretical studies have been done on both types of mechanisms [3-19].

In this study amorphous silica (SiO_2) was used as a host lattice. SiO_2 has proved to be a good host matrix for the rare-earth elements because of its transparency, dopant solubility which leads to random distribution, high doping concentration capability [20-22]. In addition, SiO_2 was chosen to evaluate the performance of lanthanide ions in the amorphous host.

In order to investigate the influence of a crystalline host in the energy transfer, the same combination of lanthanide ions doped into a LaF_3 crystalline host was prepared by using the hydrothermal method. Fluorides have become a focus of intensive research due to their promising applications in lighting and displays, biological labels, and optical amplifiers [23-26]. In comparison with oxygen-based systems, fluorides possess very low vibrational energies and therefore the quenching of the excited states of the rare earth ions will be minimal [27]. Furthermore, they exhibit adequate thermal and environmental stability and therefore are considered as ideal host materials for luminescent lanthanide ions.

Structural and luminescence properties of the prepared phosphors were studied experimentally by using different analytical techniques, i.e. X-Ray Diffraction (XRD), Infrared spectroscopy (IR), X-ray Photoelectron Spectroscopy (XPS), Photoluminescence spectroscopy (PL) and Cathodoluminescence spectroscopy (CL). Theoretical models of energy transfer mechanisms were used in order to interpret the experimental data.

2. Problem statement

Energy transfer phenomena as a tool to develop the efficiency of the luminescence materials has been a subject for much research during the last five decades. In our research group, experimental work has been done investigating the parameters which can affect the energy transfer rate such as dopant concentration [28], but a little has been done on the theoretical aspect of energy transfer. It is important to investigate theoretically the interaction mechanisms responsible for energy transfer in certain systems. Host effects on the energy transfer mechanism also need to be investigated. In this work, theoretical

calculations were used to investigate the mechanism response of the energy transfer in the studied systems. We restrict the work to consider only direct mechanisms. Numerical calculations based on Inokuti and Hirayama models [6] were developed.

3. Research aims

Using sol-gel and hydro-thermal synthesis techniques, and analytical techniques as well as theoretical calculations, the researcher aims at realizing the following objectives:

- Synthesising different phosphors, both amorphous and crystalline;
- Using different techniques to characterise the phosphors;
- Applying theoretical models to describe the different energy transfer mechanisms;
- Analysing the experimental data in comparison with the theoretical results.

4. Thesis layout

In this first chapter the introduction and aims of the study have been stated. In chapter II more detailed background information regarding phosphors is provided. Then in chapter III the theoretical models for direct mechanisms of energy transfer are discussed. Chapter IV provides general descriptions of the analytical techniques used to characterize the synthesized phosphors, including some details of calibrations or special considerations required for this research. This is continued in chapters V to XII . Finally, a conclusion is provided in chapter XIII.

References

[1] Yehoshua Y 2006 *The physics and engineering of solid state lasers* (Washington: International society for optical engineering)

[2] Claire P, Anders H and Mikael L 2005 *J. Lumin.* **111** 265

[3] Chow HC and Powell RC 1980 *Phys. Rev. B* **9** 3785

[4] Forster Th. 1948 *Ann. Physik* **2** 55

[5] Dexter DL 1953 *J. Chem. Phys.* **21** 836

[6] Inokuti M and Hirayama F 1965 *J. Chem. Phys.* **43** 1978

[7] Walter JCG 1971 *Phys. Rev.* B **4** 648

[8] Lenth W and Huber G 1981 *Phys. Rev.* B **23** 3877

[9] Bojarski C, Grabowska J, Kulak L and Kusba J 1991 *J. Fluoresc.* **1** 183

[10] Morita M, Buddhudu S, Rau D and Murakami S 2004 *Struct. Bonding* **107** 115

[11] Stavola M and Dexter DL 1979 *Phys. Rev B.* **20** 1867

[12] Martin IR, Rodriguez VD, Rodriguez-Mendoza UR and Lavin V 1999 *J. Chem. Phys.* **111** 1191

[13] Yokota M and Tanimoto1967 O *J. Phys. Soci. Japan* 22 779

[14] Malta OL 1997 *J. Lumin.* **71** 229

[15] Smentek L and Andes Hess BJr 2001 *J. Alloys Compounds* **315** 1

[16] Grether M, Lopez-Moreno E, Murrieta HS, Hernandez JA and Rubio JO 1999 *Optical Mat.* **12** 65

[17] Soos ZG and Powell RC 1972 *Phys. Rev. B* **10** 4035

[18] Lin SH 1973 *Proc. R. Soc. Lond.* **335** 51

[19] Liao DW, Cheng WD, Bigman J, Karni Y, Speiser S and Lin SH 1995 *J. Chinese Chem. Soci.* **42** 177

[20] Guodong Q, Minquan W, Mang W, Xianping F and Zhanglian H 1997 *J. L umin.* **75** 63

[21] Jan T, Johannes Z and Rolf C 2006 *J. Mater. Sci.* **41** 8173

[22] Silversmith AJ, Boye DM, Brewer KS, Gillespie CE, Lu Y and Campbell DL 2006 *J. Lumin.***121** 14

[22] Zhang X, Fan X, Qiao X and LuoQ 2010 *Mater. Chem. Phys.* **121** 274

[23] Justel T, Nikol H and Ronda C 1998 *Angew. Chem. Int. Ed.* **37** 3085

[24] Heer S, Lehmann O, Hasse M and Gudel HU 2003 *Angew. Chem. Int. Ed.* **42** 3179

[25] Li CX, Liu XM, Yang PP, Zhang CM Lian HZ and Lin J 2008 *J. Phys. Chem.* **112** 2904.

[26] Blasse G and Grabmaimer BC 1994 *Luminescent Materials* (Berlin: Springer)

[27] Sayed FN, Grover V, Godbole SV and Tyagi AK 2012 *RSC Adv.* **2** 1161

[28] Ntwaeaborwa OM, Swart HC, Kroon RE, Holloway PH and Botha JR 2006 *J. Phys. Chem. Solids* **67** 1749

Chapter II

Background information

1. Fundamentals of phosphors

A phosphor can be defined as any material that will emit light when an external excitation source is applied. These materials are mostly inorganic and are prepared in powder form or as thin films. Phosphors are based on luminescent centres located in a wide band gap host [1,2]. The characteristic luminescence properties are obtained either directly from the host, or more often from activators. An activator is an impurity ion which, when incorporated (doped) into the host lattice, gives rise to a centre which can be excited to luminesce. If more than one dopant is used, it is possible that one (called the co-activator or sensitizer) tends to absorb energy from the primary excitation and, instead of luminescing itself, it transfers this energy non-radiatively to the other dopant (the activator) to enhance its luminescent intensity [3]. Luminescence can be produced by a variety of excitation methods using photons, electrons, heat etc. These different excitation methods having different names, the luminescence resulting from excitation by high energy electrons is called cathodoluminescence and that from the excitation by light (photons) (including ultraviolet light) is called photoluminescence. Table 1 gives examples of various types of luminescence [4].

Table 1: Examples of various types of luminescence [4].

Type	Energy Supplier	Examples
Chemi-luminescence	Chemical reactions	Glow in the dark plastic tubes, emergency light
Bio-luminescence	A form of chemi-luminescence where the energy is supplied by living organisms.	Fireflies, glow-worms
Electro-luminescence	Electric current	Certain watch, displays
Cathodoluminescence	Electron beam	CRT, televisions
Radio-luminescence	Nuclear radiation	Old glow in dark paints
Triboluminescence	Some minerals glow when rubbed or scratched	Quartz crystal
Sonoluminescence	The emission of short bursts of light from imploding bubbles in a liquid when excited by sound.	
Photoluminescence	Light energy. Commonly UV or visible light. Also includes laser induced fluorescence.	Phosphors, pressure sensitive paints.

The common representation of a phosphor is given by a formula, for example, SiO_2:Ce 0.5mol%. The first part tells us that the matrix is SiO_2 and the last part tells us that the activator is Ce. The concentration of the activator relative to that of the host can be given as a percentage of the number of atoms per mole or as a percentage of weight. If the phosphor has a co-dopant, a comma is used to separate them, for example SiO_2:Ce,Tb.

2. Host

Generally host materials should exhibit good optical, mechanical and thermal properties [5]. There are many types of host such as alkali-earth sulphides, alkali-earth aluminate, rare-earth oxides, earth fluorides, silicates etc. These different types can be categorized into three groups: crystals, amorphous and materials that incorporate the properties of both (glass ceramics). The varieties of these host materials enable them to vary according to the application. For example, for photoluminescent phosphors, it is important that the host material efficiently absorbs the UV light otherwise the energy will be wasted. For cathodoluminescent phosphors, hosts must be stable under electron bombardment. For electroluminescent phosphors, hosts must have the ability to efficiently absorb and transport high-energy electrons.

3. Luminescent centres

In phosphors, luminescence centres may result from host defects such as ion vacancies or from activators, which are specially introduced atoms or ions. Luminescent centres that result from host defects are called host-crystal centres, while those that result from activators are known as activator centres. The main characteristics of luminescent centres are their emission and absorption spectra. For example, when a phosphor is activated by ions of lanthanide elements, the spectra of the luminescent centres turn out to be line spectra produced by quantum transitions in the inner electron shells of the ions. The effect of the lattice is manifested in the shifting and splitting of the spectral lines by the crystal field for example, the Stark effect and in the superposition of additional frequencies corresponding to lattice vibrations. When a phosphor is activated by atoms of elements whose spectra are produced by transitions in an outer electron shell, the lattice causes the spectral lines to be broadened into bands. A single phosphor often contains two or more types of luminescent centres. The centres may interact with one another by

exchanging electrons and holes or directly by means of excitation energy. The first type of interaction is called a recombination interaction; the second type is known as a resonance interaction.

4. Lanthanide ions

A good description of the lanthanide ions is given by [7]: "In the periodic table of elements, lanthanides are the group of atoms ranging from lanthanum (atomic number 57) to lutetium (atomic number 71) (see Figure 1). They are characterized by a gradual filling of the 4f electron shell and are therefore called f- block elements.

1 H																	2 He
3 Li	4 Be											5 B	6 C	7 N	8 O	9 F	10 Ne
11 Na	12 Mg											13 Al	14 Si	15 P	16 S	17 Cl	18 Ar
19 K	20 Ca	21 Sc	22 Ti	23 V	24 Cr	25 Mn	26 Fe	27 Co	28 Ni	29 Cu	30 Zn	31 Ga	32 Ge	33 As	34 Se	35 Br	36 Kr
37 Rb	38 Sr	39 Y	40 Zr	41 Nb	42 Mo	43 Tc	44 Ru	45 Rh	46 Pd	47 Ag	48 Cd	49 In	50 Sn	51 Sb	52 Te	53 I	54 Xe
55 Cs	56 Ba	57 La	72 Hf	73 Ta	74 W	75 Re	76 Os	77 Ir	78 Pt	79 Au	80 Hg	81 Tl	82 Pb	83 Bi	84 Po	85 At	86 Rn
87 Fr	88 Ra	89 Ac	104 Rf	105 Db	106 Sg	107 Bh	108 Hs	109 Mt	110 Ds	111 Rg	112 Cn	113 Uut	114 Fl	115 Uup	116 Lv	117 Uus	118 Uuo

58 Ce	59 Pr	60 Nd	61 Pm	62 Sm	63 Eu	64 Gd	65 Tb	66 Dy	67 Ho	68 Er	69 Tm	70 Yb	71 Lu
90 Th	91 Pa	92 U	93 Np	94 Pu	95 Am	96 Cm	97 Bk	98 Cf	99 Es	100 Fm	101 Md	102 No	103 Lr

Figure 1: The periodic table of elements. The lanthanides are highlighted in green.

The different lanthanides have very similar chemical behaviours so that their properties can be discussed in a general way. Lanthanide ions are most frequently found in the trivalent (3+) oxidation state, although tetravalent (4+) cerium and divalent (2+) europium also occur. The f-orbitals are shielded by the 5s and 5p orbitals. Therefore, the f-electrons do not participate in chemical bonding so that the predominant interactions in lanthanide complexes are electrostatic ones. The shielding of the spectroscopically active 4f-electrons by filled 5s and 5p orbitals also results in distinct spectroscopic characteristics for the trivalent lanthanide ions. In contrast to the broad bands observed for transition metal ions, the lanthanide f-f electronic transitions exhibit typically very narrow lines in the luminescence and absorption spectra. Since changes in the local environment of the lanthanide ion has a negligible influence on the 4f-electrons,

coordination will only affect the fine structure of the absorption and emission bands, rather than result in major shifts in the peak position. Lanthanide ions can show emission in the near-UV, visible, near-infrared and infrared spectral regions. Each lanthanide ions has a characteristic absorption and emission spectra."

Dieke *et al.* [8] investigated the energy levels of 4f electrons of trivalent lanthanide ions. They showed their results in a diagram known as the Dieke diagram which is presented in Figure 2 [9].

The 4f shell of the lanthanide group is poor shielded from the nucleus, as result of this poor shielding; the ionic radius of the lanthanide ions is decreases as the atomic number is increases. This phenomenon is known as lanthanide contraction [10].

In addition to f-f transitions, f-d transitions are also observed at even higher energy or shorter wavelength, usually in the ultraviolet region. These transitions are allowed and hence more intense than f–f transitions. Due to the interaction of the 5d-electrons with the ligand ions, the bonding strength changes upon 4f–5d excitation, giving broad absorption and emission bands instead of lines [11]. This phenomenon occurs in Ce^{3+} ions.

5. Excitation and emission processes

Luminescent centres can be excited by different ways according to the source used. Here a short discussion of excitation and emission processes when photons are used as excitation source (photoluminescence) is presented. The energy levels of molecules/ atoms determined by the molecular/atomic orbitals hold the molecule/atom bound together. An electron in the valance band moves from its ground state to an excited state by absorbing a photon (Figure 3). This phenomenon is called excitation.

The excited states are not stable and will not remain indefinitely. The excited electron releases some of the absorbed energy as phonon and fall to a lower, more stable, energy level called the relaxed electronic state. Then the electrons move back from the excited states to their ground state they release the excess energy as photons (Figure 3). This is called emission (luminescence or fluorescence). The difference in photon energy of absorbed and emitted photons is known as Stokes shift. Figure 3 illustrates the energy

level diagram showing absorption, relaxation, and emission (fluorescence) processes beside the absorption and emission band and Stokes shift [12, 13].

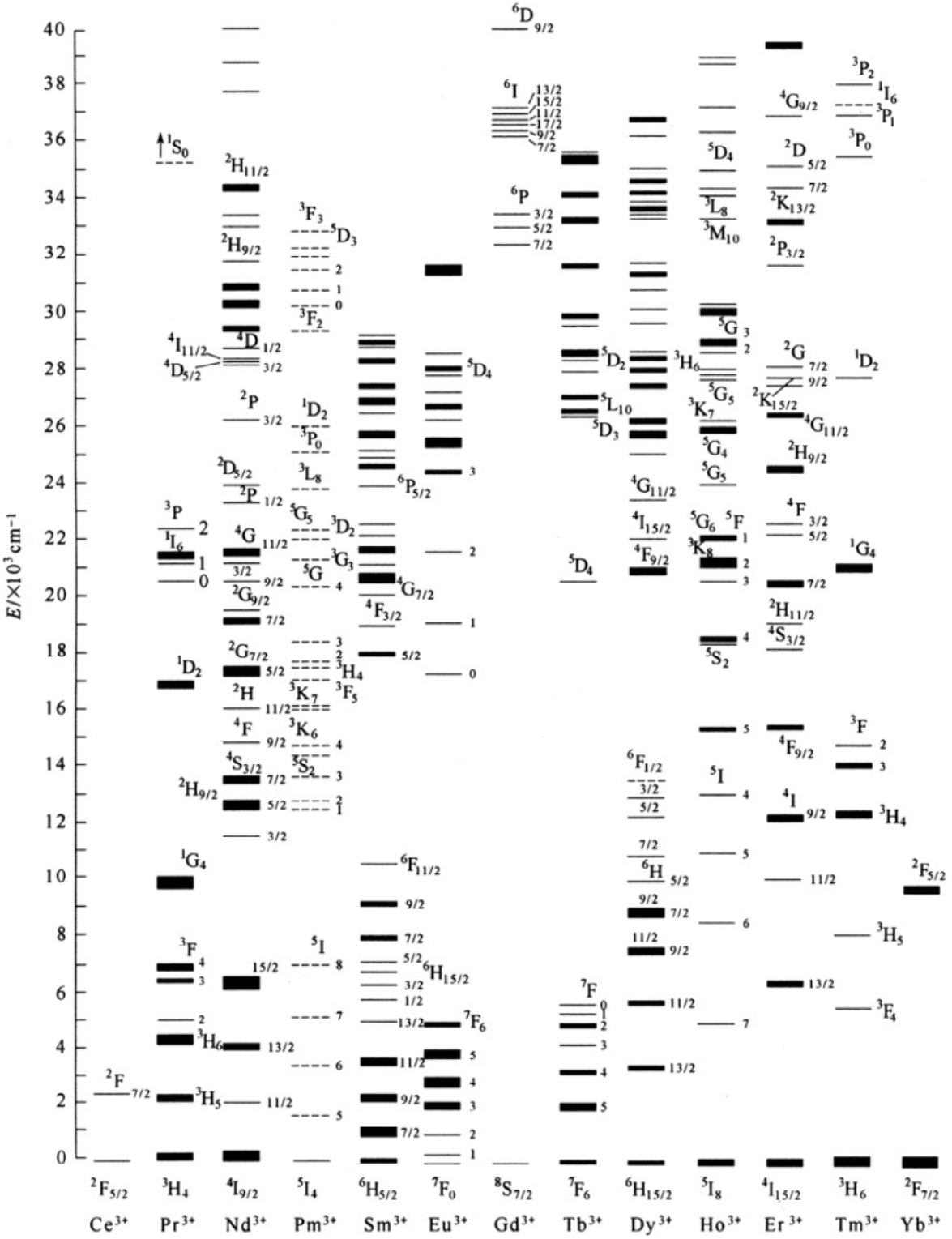

Figure 2: The Dieke diagram [9]

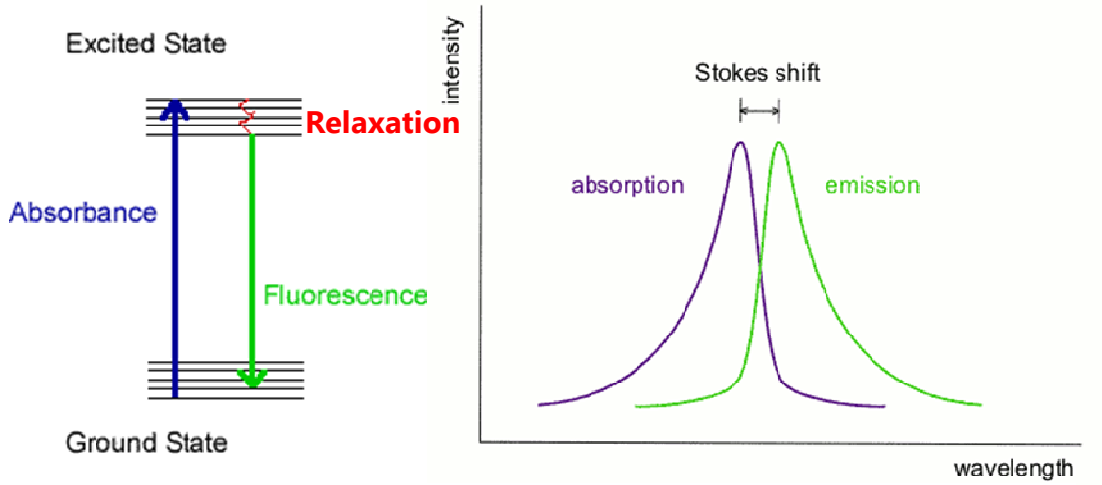

Figure 3: Energy level diagram showing absorption, relaxation, and emission processes and the Stokes shift between the absorption and emission band [11, 12].

6. Fluorescence and Phosphorescence

Photoluminescence processes are divided into two classes: fluorescence, and phosphorescence. Fluorescence involves absorbing and releasing lower energy light almost immediately in $\leq 10^{-7}$ s, while the light release of phosphorescence is delayed for $\geq 10^{-6}$ s, so these materials appear to glow in the dark. In fact, most phosphorescent materials are emitted relatively fast with lifetimes on the order of milliseconds, nevertheless, some materials have lifetimes up to minutes or even hours.

According to the quantum mechanics, in the fluorescence process, an electron does not change its spin direction. The situation where no spin flip occurs, suggests that the molecule is in a singlet state. In phosphorescence process, under the appropriate conditions, a spin-flip can occur. When the electron undergoes a spin-flip, a triplet state is created. As a result, the electron can become trapped in the triplet state. The transitions from these triplet states to the lower energy state are forbidden. Although these transitions are forbidden, yet can be occur in quantum mechanics but are unfavoured and thus takes more time. Figure 4 shows the Jablonski diagram for absorption, fluorescence, and phosphorescence [14].

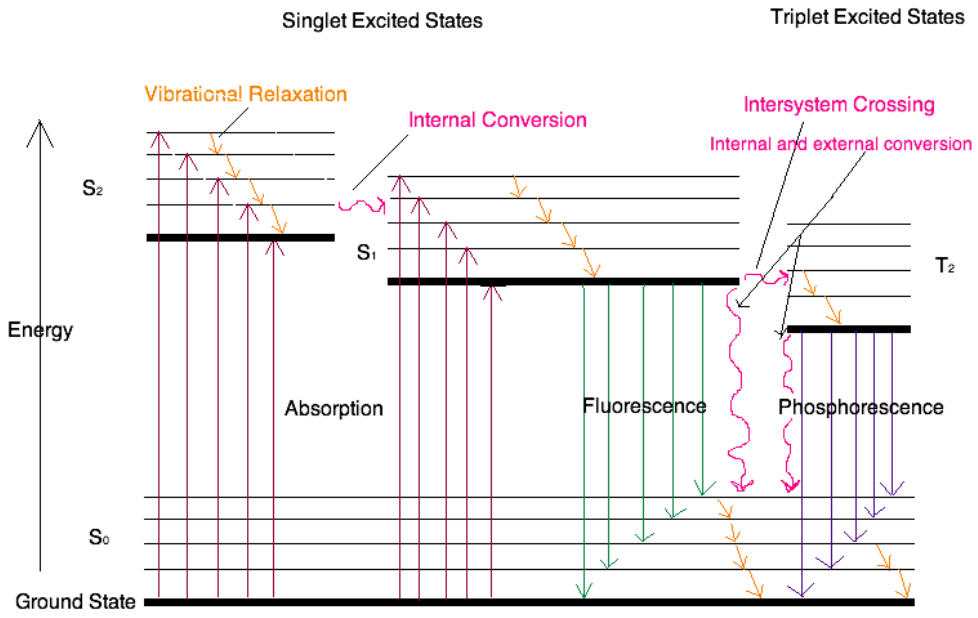

Figure 4: Jablonski diagram for absorption, fluorescence, and phosphorescence [13].

7. Applications of phosphors

The applications of phosphors in various technologies increases continuously, which necessitates more research efforts to develop these technologies and make them more efficient and cheap. Applications of phosphors , among other things, arelight sources in (1) display devices, (2) fluorescent lamps (3) detectors, and (4) other simple applications, such as luminous paint with long persistent phosphorescence, long afterglow phosphors coated pointers, signs, light switches, etc. Figure 5 shows some of these applications [15-21].

(a) Fluorescent lamp

(b) Displays

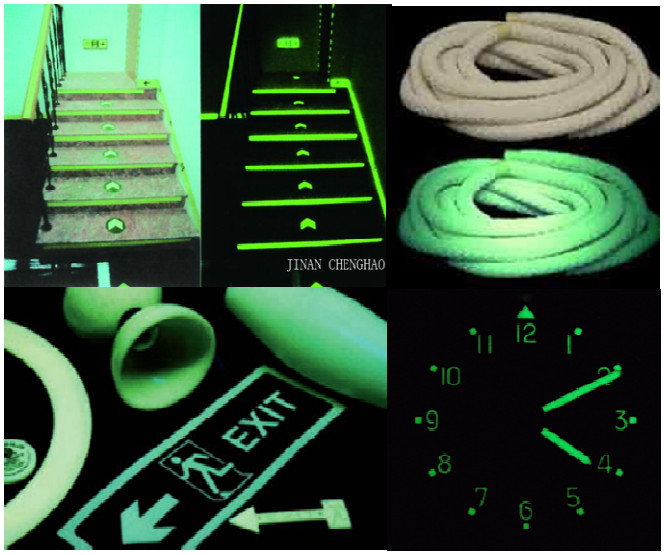

(c) Luminous paint and long afterglow coating phosphor

Figure 5: Some of phosphor applications [15-21].

8. Preparation methods of phosphors

A phosphor is composed of a host and activator(s). There are two different ways to prepare a phosphor. In the first one, activator ions are introduced into an existing host material. In the second scheme, host material synthesis and activator incorporation proceed simultaneously. Each one of these two ways has many different chemical routes of synthesis. Second scheme were applied to prepare the phosphors used in this study. We restrict ourselves to the sol-gel and hydrothermal methods which are used in this study.

8.1 Sol-gel method

The sol-gel method is a wet-chemical synthesis technique for preparing oxide gels, glasses, and ceramics at low temperature. It is based on control of hydrolysis and condensation of alkoxide precursors. It is possible to fabricate ceramic or glass materials in a variety of forms, such as ultra-fine powers, fibers, thin films, porous aerogel materials or monolithic bulky glasses and ceramics [22].

The sol-gel process, as the name implies, involves transition from a liquid 'sol' (colloidal solution) into a 'gel' phase [23]. Usually inorganic metal salts or metal organic compounds such as metal alkoxide are used as precursors. A colloidal suspension, or a 'sol' is formed after a series of hydrolysis and condensation reaction of the precursors. Then the sol particles condense into a gel. Then drying and annealing is followed converted the gel into dense ceramic or glass materials.

The sol-gel process can be described by three reactions : hydrolysis, alcohol condensation and water condensation. Because of immiscible lack between alkoxides and water, alcohol is commonly used as a solvent. Due to the presence of the co-solvent, the sol-gel precursor, alkoxide, mixes well with water to facilitate the hydrolysis reaction:

$$Si(OR)_4 + H_2O \leftrightarrows HO\text{-}Si(OR)_3 + R(OH). \qquad (1)$$

During the hydrolysis reaction, the alkoxide groups (OR) are replaced with hydroxyl group (OH) through the addition of water. Two partially hydrolysed molecules can link together in a condensation reaction such as water condensation

$$\equiv Si\text{-}OH + OH\text{-}Si\equiv \quad \leftrightarrows \quad \equiv Si\text{-}O\text{-}Si\equiv + H_2O \qquad (2)$$

or alcohol condensation

$$\equiv Si\text{-}OR + OH\text{-}Si\equiv \quad \leftrightarrows \quad \equiv Si\text{-}O\text{-}Si\equiv + R\text{-}OH. \qquad (3)$$

As the number of ≡Si-O-Si≡ group increases, they bridge with each other and a silica network is formed. Upon drying, the solvents that are trapped in the network are driven off. With further heat treatment at high temperature, the organic residue in the structure is taken out, the interconnected pores collapse and a densified glass or ceramics is formed.

Although hydrolysis can occur without an additional catalyst, it has been observed that with the help of acid or base catalyst the speed and extent of the hydrolysis reaction can be enhanced.

Heat treatment of the porous gel at high temperature is necessary for the production of dense glass or ceramics from the gel silica. After the high temperature annealing, the pores are eliminated and the density of the sol-gel materials ultimately becomes equivalent to that of the fused glass. The densification temperature depends considerably on the dimension of the pores, the degree of connection of the pores, and the surface areas in the structure [24].

8.2 Hydrothermal method

Hydrothermal synthesis generally refers to any heterogeneous reaction takes place in the presence of solvents in closed vessel under high temperature and pressure conditions to dissolve and recrystallize materials that are insoluble under normal conditions [25]. There are many different definitions for hydrothermal synthesis in the literature [26-29]. Byrappa and Yoshimura [29] define hydrothermal as any heterogeneous chemical reaction in the presence of a solvent (whether aqueous or non-aqueous) above room temperature and at pressures greater than 1 atm in a closed system.

In the hydrothermal method, the reaction usually occurs in a steel pressure vessels called autoclaves (see Figure 6). Hydrothermal procedure involve; dissolving the precursor substances (in water) and put in the reaction vessel; heating to the desired reaction

temperature; cooling the autoclave; isolating the product (by filtration or centrifugal) and washing it in order to obtain the pure product.

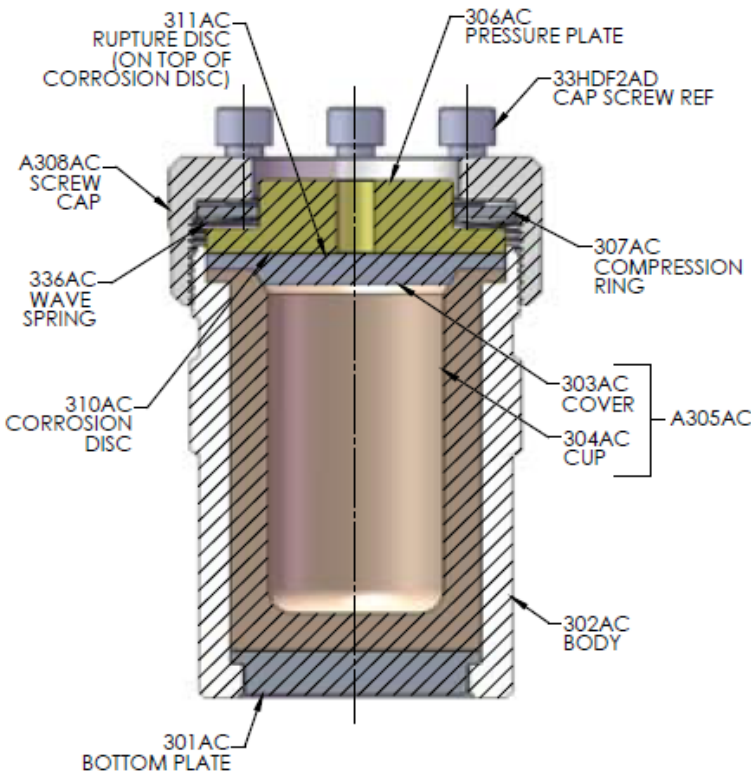

Figure 6: Schematic diagram of 4748 high pressure vessel [30]

The hydrothermal method has several advantages over traditional solid state reactions including the ability to create crystalline phases which are not stable at the melting point, high purity (> 99.5%) and chemical homogeneity, small particle size (< 5 nm possible), single step processing, low energy usage, fast reaction times, no calcination is required for many materials since they are fully crystallized by the reaction [25].

References

[1] Belsky AN and Krupa JC 1999 *Displays* **19** 185

[2] Krupa JC and Queffelec M 1997 *J. Alloys Compds* **250** 287

[3] DeLuca JA 1980 *J. Chem. Edu*. **57** 541

[4] Khalid AH and Kontis K 2008 *Sensors* **8** 5673

[5] Yehoshua Y 2006 *The physics and engineering of solid state lasers* (Washington: International society for optical engineering)

[6] Cotton S 2006 *Lanthanide and Actinide Chemistry* (Wiltshire: Wiley)

[7] Kyra Lunstroot PhD thesis , [online]. Available from https://lirias.kuleuven.be/ bitstream/1979/1921/2/PhDthesis_KyraLunstroot_sept2008.pdf [Accessed 4 June 2012]

[8] Dieke GH and Crosswhite HM 1963 *Appl. Opt.* **2** 675

[9] Chen D, Wang Y and Hong M 2012 *Nano Energy* **1** 73

[10] Modern Inorganic Chemistry , [online]. Available from http://www.chem.iitb.ac.in/ ~rmv/ch102/ic1.pdf [Accessed 28 August 2012]

[11] Ruiperez F, Barandiaran Z and Seijo L 2005 *J. Chem.Phys.* **123** 244703

[12] Fluorescence Instrumentation, [online]. Available from http://www.kutztown.edu /acad/ chem/instruments_html/fluorescence.htm [Accessed 4 June 2012]

[13] Stokes shift, [online]. Available from http://en.wikipedia.org/wiki/Stokes_shift [Accessed 4 June 2012]

[14] Electronic Spectroscopy: Theory, [online]. Available from http://chemwiki.ucdavis.edu/Physical_Chemistry/Spectroscopy/Electronic_Spectroscopy/Electronic_Spectroscopy%3A_Theory [Accessed 4 June 2012]

[15] Fluorescent lamp, [online]. Available from http://en.wikipedia.org/wiki/Fluorescent_lamp [Accessed 4 June 2012]

[16] Fluorescent Bulbs: A Proven Lighting Choice, [online]. Available from http:// edisonbulbs.org/FLUORESCENT-BULBS-A-PROVEN-LIGHTING-CHOICE [Accessed 4 June 2012]

[17] wide screen monitor line, [online]. Available from ttp://customer.decraneaerospace.com/audio/productinfo/product_information/Monitors/Wide_Screen_Monitor_Line.htm [Accessed 4 June 2012]

[18] Made-in-china.com, [online]. Available from http://www.made-in-china.com/showroom/pennywh/product-detailqeZmOJjCZErT/China-17-Normal-CRT-Monitor-726B-.html [Accessed 4 June 2012]

[19] Li2 Technologies, [online]. Available from http://products.li2.in/display/53-lcd-display.html [Accessed 4 June 2012]

[20] Water-based Luminous Paint, [online]. Available from http://www.diytrade.com/china/pd/4762099/Water_based_Luminous_Paint.html [Accessed 4 June 2012]

[21] List of Things that Glow in the Dark, [online]. Available from http://chemistry.about.com/od/glowingprojects/tp/List-Of-Things-That-Glow-In-The-Dark.htm [Accessed 4 June 2012]

[22] Roy R 1987 *Science* **238** 1664

[23] Wright JD and Sommerdijk NAJM 2001 *Sol-gel Materials: Chemistry and applications* (King's Lynn: Gordon and Breach)

[24] Hench LL and West JK 1990 *Chem. Rev.* **90** 33

[25] Byrappa K and Adschiri T 2007 *Prog. Cryst. Growth Charact. Mater.* **53** 117

[26] Morey GW and Arnor J 1953 *Ceram. Soc.* **36** 279

[27] Rabenau A 1985 *Angew. Chem., Int. Eng. Ed*. **24** 1026

[28] Roy R 1994 *J. Solid State Chem.* **111** 1

[29] Byrappa K and Yoshimura M 2001 *Handbook of Hydrothermal Technology* (New Jersey: Noyes Publications)

[30] 4744-49 Acid Digestion Vessels operating instruction manual [online]. Available from http://www.parrinst.com/ [Accessed 30 June 2012]

Chapter III

Theory of energy transfer

1. Introduction

Fluorescence energy transfer phenomena is a process whereby the excitation energy absorbed by a luminescent centre called a donor (D) is transferred to another centre called an acceptor (A). Thereafter the excited acceptor may release the energy as a photon. The phenomena can be classified into two types: direct and indirect energy transfer [1]. In the first case, the energy is transferred directly from the donor to the acceptor, while in the second case the energy is transferred to the acceptor after multistep diffusion among the donors. Both two cases were treated theoretically by many researchers [1-17]. Although both two types can contribute to the energy transfer, we restrict ourselves to the direct energy transfer.

Forster developed a theory for the rate of energy transfer by electric dipole-dipole interaction [2], which was later extended by Dexter to involve the higher multipole interactions [3]. Dexter also created a model for the shorter donor-acceptor distance based on the exchange interaction [3]. Inokuti and Hirayama [4] developed numerical methods on energy transfer that can be used to determine the mechanism responsible for energy transfer. Details of Forster's and Dexter's theories and Inokuti and Hirayama's numerical calculations are discussed in this chapter.

2. Non-radiative energy transfer

The non-radiative transfer of an electronic excitation from a donor to an acceptor is represented by

$$D^* + A \rightarrow D + A^* \qquad (1)$$

where D and A represent the ground states of donor and acceptor respectively, while D^* and A^* represents the excite state (see Figure 1 (a)).

The process consists of the following steps [18]:

- Absorption of the excitation energy by the donor center D
- Relaxation of the lattice about the donor
- Transfer of energy from donor center D to the acceptor center A
- Relaxation of the lattice about the acceptor
- Emission of luminescence by the acceptor center A

Figure 1 (b) illustrates these steps [19].

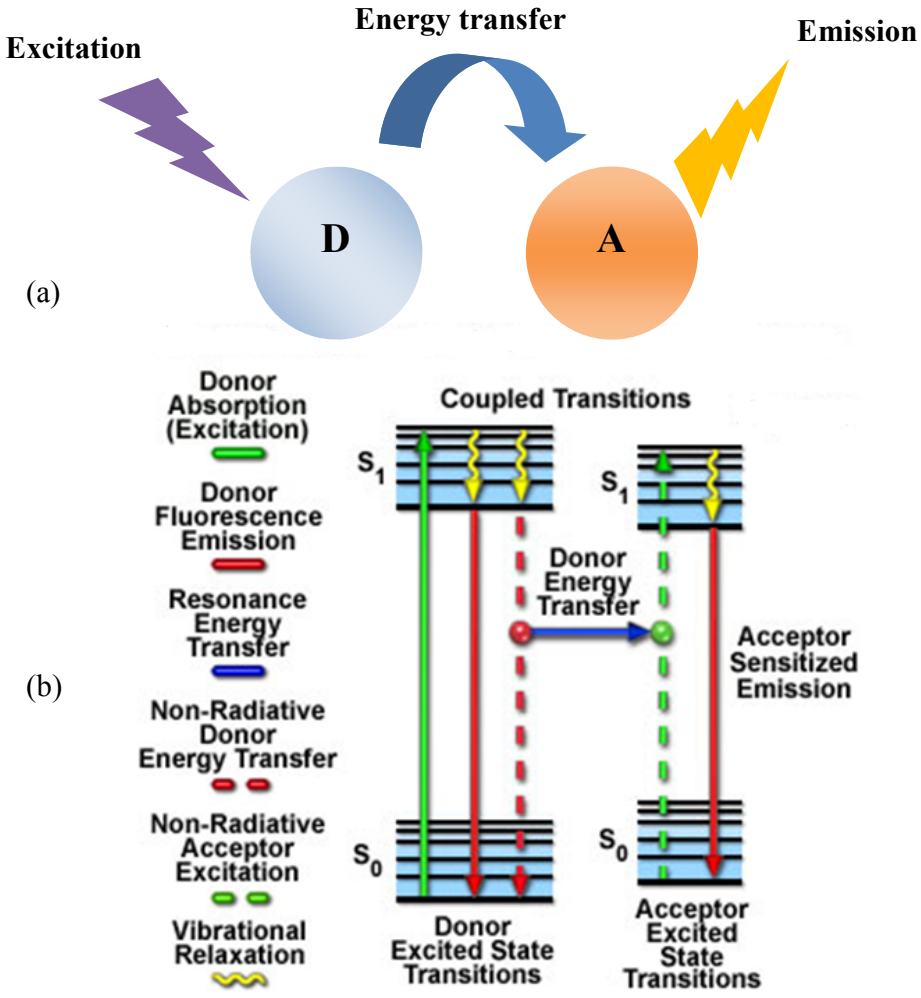

Figure 1: (a) Illustration of energy transfer phenomenon (b) coupled transitions between donor emission and acceptor absorbance in fluorescence resonance energy transfer. Absorption and emission transitions are represented by straight vertical arrows (green and red respectively), while vibrational relaxation is indicated by wavy yellow arrows. The coupled transitions are drawn with dashed lines. The phenomenon of energy transfer is illustrated by a blue arrow [19].

3. Forster's and Dexter's models

Non-radiative energy transfer has been observed and treated theoretically by Forster [2], and was developed by Dexter [3]. In Forster's model, energy is transferred from the donor D to the acceptor A by multipole interactions, while in Dexter's model energy transfer occurs by quantum-mechanical exchange of the excited electron between D and A. Although the nature of the two models are different, both of them require overlap between the emission spectrum of the donor and the excitation spectrum of the acceptor.

Schematic diagram for Forster's and Dexter's models of energy transfer is illustrated in Figure 2 [20] Singlet-singlet energy transfer can happen via Forster's model. However, the multipole interaction will not involve the triplet-triplet energy transfer because that violates the Wigner spin conservation law, which states that the exchange mechanism (Dexter's model) is based on the Wigner spin conservation rule; thus, the spin-allow process could be either singlet-singlet energy transfer or triplet-triplet energy transfer.

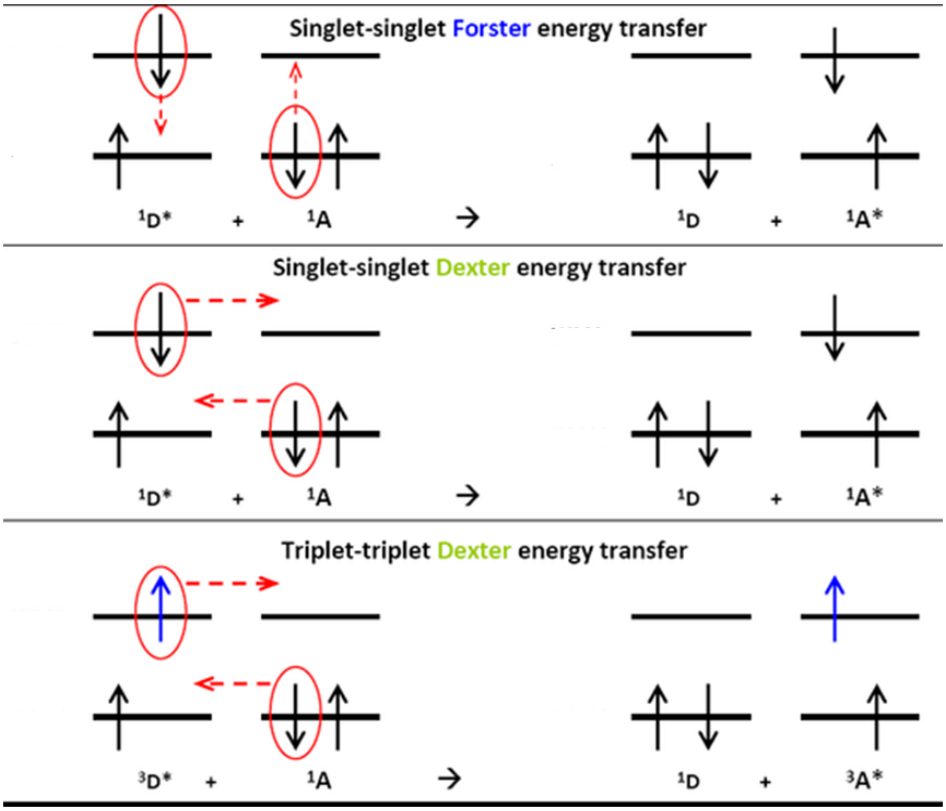

Figure 2: Schematic diagram for Forster and Dexter energy transfer [20]

4. Calculation of the energy transfer rate

The transfer rate between the two states according to Fermi's golden rule is given by

$$W_{DA} = \frac{2\pi}{\hbar} |\langle DA^*|\mathcal{H}_{DA}|D^*A\rangle|^2 \int f_D(E) f_A(E) dE \qquad (2)$$

where $\langle DA^*|$ is the final state, $|D^*A\rangle$ is the initial state, and $\mathcal{H}$ is the interaction Hamiltonian. The integral represent the spectral overlap between the donor (D) emission spectrum and the acceptor (A) absorption spectrum (see Figure 3), $f_D(E)$ is the normalized emission spectrum of the donor, and $f_A(E)$ is the normalized absorption spectrum of the acceptor.

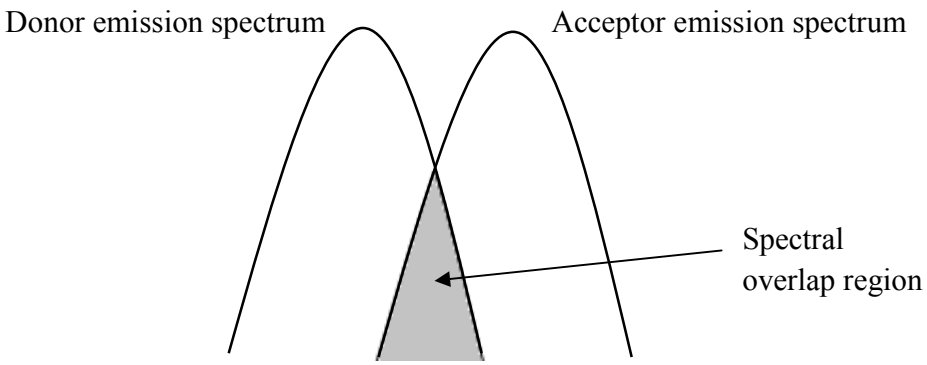

Figure 3: The spectral overlap between the donor (D) emission spectrum and the acceptor (A) absorption spectrum

4.1 Forster theory

Let us consider Forster theory for dipole-dipole interaction first. Since the donor and acceptor are weakly coupled, the Hamiltonian for this problem can be written in a form that can be solved by perturbation theory

$$\mathcal{H}_{DA} = \mathcal{H}_0 + V \qquad (3)$$

where $\mathcal{H}_0$ is the unperturbed part of the Hamiltonian having known solution, and V is the perturbation correction.

For the dipole-dipole interaction

$$\mathcal{H}_0 = |D^*A\rangle\mathcal{H}_D\langle D^*A| + |A^*D\rangle\mathcal{H}_A\langle A^*D| \quad (4)$$

and

$$V = \frac{3(\bar{\mu}_A.\hat{r})(\bar{\mu}_D.\hat{r}) - \bar{\mu}_A.\bar{\mu}_D}{r^3} \quad (5)$$

where r is the distance between donor and acceptor molecules, μ_D and μ_A are the dipole operators. The dipole operators here are more properly referred to as the transition dipole moments that couple the ground and excited electronic states for the donor and acceptor:

$$\bar{\mu}_A = |A\rangle\bar{\mu}_{AA^*}\langle A^*| + |A^*\rangle\bar{\mu}_{A^*A}\langle A| \quad (6)$$

$$\bar{\mu}_D = |D\rangle\bar{\mu}_{DD^*}\langle D^*| + |D^*\rangle\bar{\mu}_{D^*D}\langle D|. \quad (7)$$

For the dipole moment, we can factor out the orientational contribution as a unit vector as illustrated in Figure 4 [21], i.e.,

$$\begin{aligned}\bar{\mu}_D &= \hat{u}_D\mu_D \\ \bar{\mu}_A &= \hat{u}_A\mu_A.\end{aligned} \quad (8)$$

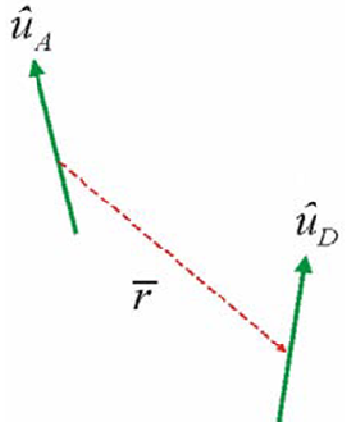

Figure 4: Orientations unit vector of the donor emission dipole and the acceptor absorption dipole [21]

The transition dipole interaction can now be written as:

$$V = \mu_A\mu_D\frac{k}{r^3}[|D^*A\rangle\langle A^*D| + |A^*D\rangle\langle D^*A|] \quad (9)$$

$$k = 3(\hat{u}_A.\hat{r})(\hat{u}_D.\hat{r}) - \hat{u}_A.\hat{u}_D. \quad (10)$$

All of the orientational factors are now in the term *k*.

Now equation (2) can be rewritten as

$$W_{DA} = \frac{1}{\hbar^2}\int_{-\infty}^{+\infty} dt \frac{k^2}{r^6}\langle D^*A|\mu_D(t)\mu_A(t)\mu_D(0)\mu_A(0)|D^*A\rangle \qquad (11)$$

where

$$\mu_D(t) = e^{+i\mathcal{H}_D t/\hbar}\mu_D e^{-i\mathcal{H}_D t/\hbar} \qquad (12)$$

$$\mu_A(t) = e^{+i\mathcal{H}_A t/\hbar}\mu_A e^{-i\mathcal{H}_A t/\hbar}. \qquad (13)$$

The rotational factor is easier to evaluate if the dipoles are static, or they rapidly rotate to become isotropically distributed.

We can express the energy transfer rate as an overlap integral between the donor fluorescence and acceptor absorption spectra as follows

$$W_{DA} = \frac{1}{\hbar^2}\frac{k^2}{r^6}|\mu_{DD^*}|^2|\mu_{AA^*}|^2\int_{-\infty}^{+\infty} f_D(E)f_A(E)dE \qquad (14)$$

so the energy transfer rate scales inversely with r^6, depends on the strengths of the electronic transitions for donor and acceptor molecules, and requires resonance between donor fluorescence and acceptor absorption. The rate of energy transfer is usually written as

$$W_{DA} = \frac{1}{\tau_0}\left(\frac{R_0}{r}\right)^6 \qquad (15)$$

where R_0 is the Forster critical distance, τ_0 is the donor lifetime in the absence of the acceptor. The Forster critical distance R_0 is defined as the acceptor-donor separation radius for which the transfer rate equals the rate of donor decay in the absence of acceptor. In other words, when the donor and acceptor radius (r) equals the Forster distance, then the transfer efficiency is 50 percent (see Figure 5). At this separation radius, half of the donor excitation energy is transferred to the acceptor via resonance energy transfer, while the other half is dissipated through a combination of all the other available processes, including fluorescence emission.

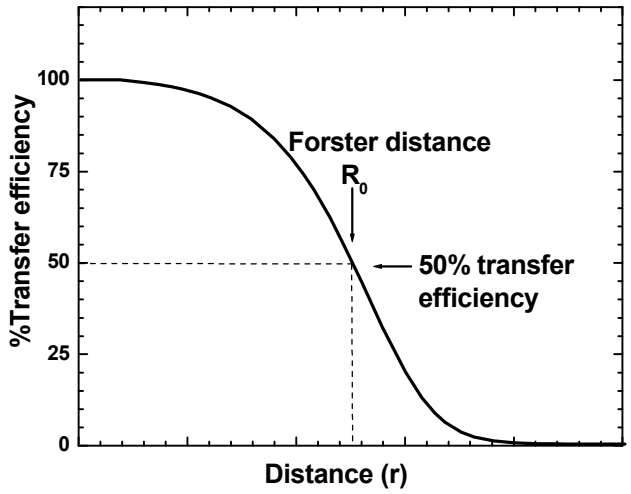

Figure 5: Transfer efficiency as a function of distance. The transfer efficiency is 50% when the distance equals to the Forster radius (R_0).

4.2 Dexter theory

Dexter extended this theory to include higher multipole and exchange interactions. For higher multipole interaction the rate of energy transfer can be written as

$$W_{DA} = \frac{1}{\tau_0}\left(\frac{R_0}{r}\right)^S \tag{16}$$

where s = 6, 8 and 10 corresponding to the dipole-dipole, dipole-quadrupole and quadrupole -quadrupole interactions respectively.

For the exchange interaction, Dexter derived the following expression for the rate of energy transfer [3]

$$W_{DA} = \frac{2\pi}{\hbar^2} Z^2 \int f_D\,(E) f_A(E) dE \tag{17}$$

with

$$Z^2 = K^2 \exp\,(-2r/L) \tag{18}$$

where K is a constant with a dimension of energy, L a constant called the effective Bohr radius. With the same analogy of multipole interaction, one can write the rate of energy transfer for exchange interaction as

$$W_{DA} = \frac{1}{\tau_0} \exp\left(\gamma\left[1-\frac{r}{R_0}\right]\right) \tag{19}$$

where γ is a constant related to Dexter's quantities by

$$\gamma = \frac{2R_0}{L}. \tag{20}$$

5. Numerical calculations

Inokuti and Hirayama [4] made numerical calculations on energy transfer due multipole and exchange interactions. These can be used to determine the mechanism responsible for energy transfer. They considered a system which has a random distribution of energy donors and energy acceptors in an inert medium. Both of the donor and the acceptor are assumed to have only one excited state. If a donor is excited at time t = 0 with the absence of the acceptors, the probability $p(t)$ of finding the donor in the excited state at time *t* is a simple exponential decay

$$p(t) = \exp(-t/t_0) \tag{21}$$

where τ_0 is the isolated donor lifetime.

When acceptors are present, this probability decreases due to energy transfer. Let $W_{DA}(r_k)$ be the rate of energy transfer from a donor *D* to an acceptor *A* at a distance r_k. Then

$$p(t) = \exp(-t/t_0) \prod_{k=1}^{N} \exp[-tW_{DA}(r_k)] \tag{22}$$

where N is the total number of acceptors in the vicinity of the donor.

If n(r) is the probability distribution of the donor acceptor distance r in the volume V, the statistical average $\phi(t)$ of p(t) can be written as

$$\phi(t) = \exp\left(-\frac{t}{t_0}\right) \lim_{N\to\infty, V\to\infty} \{4\pi/V \int_0^{r_V} \exp[-tW_{DA}(r_k)] r^2 dr\}^N \tag{23}$$

$\phi(t)$ is called the donor decay function and it can be used to calculate the relative emission intensity of the donor as

$$\frac{I}{I_0} = \frac{1}{\tau_0}\int_0^\infty \phi(t)dt \tag{24}$$

and the average decay time τ_m of the donor as

$$\frac{\tau_m}{\tau_0} = \frac{1}{\tau_0}\int_0^\infty t\phi(t)dt \Big/ \int_0^\infty \phi(t)dt. \tag{25}$$

6. Calculation for the multipole and exchange interactions

$\phi(t)$ can be calculated for multipole interaction by substituting equation (15) in equation (23) and for exchange interaction by substituting equation (18) in equation (23). From Inokuti and Hirayama calculations, $\phi(t)$ for multipole is

$$\phi(t) = \exp\left[\frac{-t}{\tau_0} - \Gamma\left(1 - \frac{3}{s}\right)\frac{c}{c_0}\left(\frac{t}{\tau_0}\right)^{3/s}\right] \tag{26}$$

where c is the acceptor concentration

$$c = 3N/(4\pi r_V^3) \tag{27}$$

and c_0 is a parameter called the critical transfer concentration, defined by

$$c_0 = \frac{3}{4\pi R_0^3}. \tag{28}$$

By substituting (26) in (24) and (25) and using numerical calculation, the relative emission intensity of the donor $\frac{I}{I_0}$ and the decay time $\frac{\tau_m}{\tau_0}$ as a function of $\frac{c}{c_0}$ can be calculated. Figure 6 presents the theoretical curves of $\frac{I}{I_0}$ and $\frac{\tau_m}{\tau_0}$ vs $\frac{c}{c_0}$ for the dipole-dipole, dipole-quadrupole and quadrupole-quadrupole interactions. Figure 7 shows a plot of $\frac{I}{I_0}$ vs $\frac{\tau_m}{\tau_0}$. This representation is very helpful because it can be used to determine the interaction mechanism responses of energy transfer by fitting the experimental data to the theoretical one. The best fitted curve (s = 6, 8 or10) implying the interaction mechanism caused the energy transfer. After determining (s), Figure 6 can be used to determine c_0.

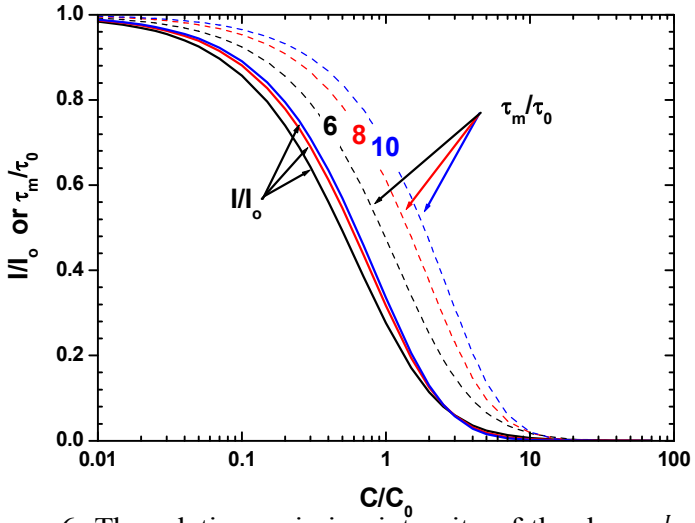

Figure 6: The relative emission intensity of the donor $\frac{I}{I_0}$ and the decay time $\frac{\tau m}{\tau_0}$ as a function of $\frac{c}{c_0}$ for the dipole-dipole (black), dipole-quadrupole (red) and quadrupole-quadrupole (blue) interaction. The abscissa represents $\frac{c}{c_0}$ in logarithmic scale, and the ordinate represents $\frac{I}{I_0}$ (solid lines) and $\frac{\tau m}{\tau_0}$ (dashed lines)

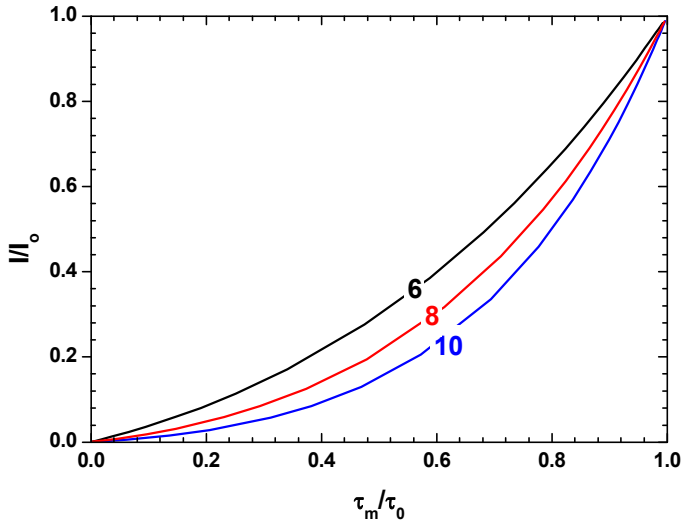

Figure 7: The relative emission intensity of the donor $\frac{I}{I_0}$ vs the decay time $\frac{\tau m}{\tau_0}$ for the dipole-dipole (black), dipole-quadrupole (red) and quadrupole-quadrupole (blue) interaction.

For the exchange interaction, Inokuti and Hirayama calculations for ϕ(t) gives

$$\phi(t) = \exp\left[\frac{-t}{\tau_0} - \gamma^{-3}\frac{c}{c_0}\mathrm{g}(z)\right] \tag{29}$$

where

$$\mathrm{z} = \frac{t}{\tau_0}e^{\gamma} \tag{30}$$

and $\mathrm{g}(z)$is a function which can be written for numerical evaluation as a Taylor series of the form

$$\mathrm{g}(z) = 6z\sum_{m=0}^{\infty}\frac{(-z)^m}{m!(m+1)^4}. \tag{31}$$

For sufficiently large value of z, $\mathrm{g}(z)$ can be expressed by

$$\mathrm{g}(z) = (\ln z)^3 + h_1(\ln z)^2 + h_2(\ln z) + h_3 + \mathrm{O}[e^{-z}(\ln z)^3 z^{*2}] \tag{32}$$

where

$$h_1 = 1.73164699$$
$$h_2 = 5.93433597 \tag{33}$$
$$h_3 = 5.44487446.$$

Inokuti and Hirayama achieved accuracy of 10^{-8} by using (31) for $z \leq 10$ and the leading terms in (32) for $z > 10$.

The relative emission intensity of the donor $\frac{I}{I_0}$ and the decay time $\frac{\tau_m}{\tau_0}$ as a function of $\frac{c}{c_0}$ can be calculated numerically for exchange interaction by substituting (29) in (24) and (25) and used (31) or (32) to evaluate (z). Plots of $\frac{I}{I_0}$ and $\frac{\tau_m}{\tau_0}$ vs $\frac{c}{c_0}$ and $\frac{I}{I_0}$ vs $\frac{\tau_m}{\tau_0}$ can be produced for different values of γ and the experimental data can be fitted to determine γ and c_0.

Figure 8 shows the theoretical curves of $\frac{I}{I_0}$ and $\frac{\tau_m}{\tau_0}$ vs $\frac{c}{c_0}$ for various values of γ for exchange interaction. A plot of $\frac{I}{I_0}$ vs $\frac{\tau_m}{\tau_0}$ for the same γ is presented in Figure 9.

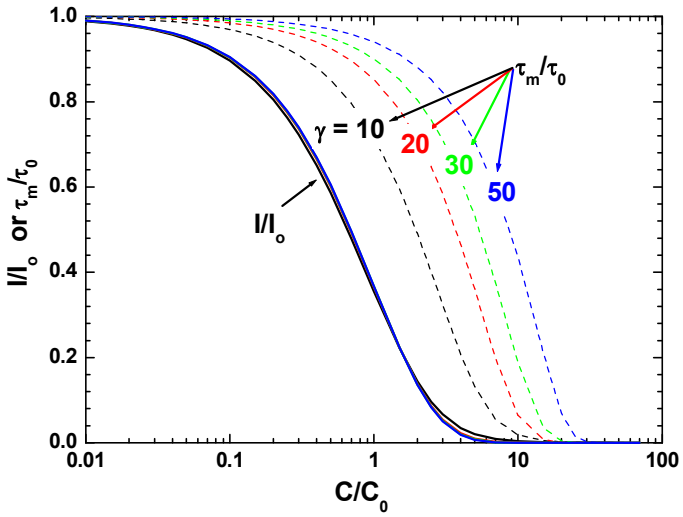

Figure 8: The relative emission intensity of the donor $\frac{I}{I_0}$ and the decay time $\frac{\tau m}{\tau_0}$ as a function of $\frac{c}{c_0}$ for exchange interaction. γ = 10, 20, 30 and 50. The abscissa represents $\frac{c}{c_0}$ in logarithmic scale, and the ordinate represents $\frac{I}{I_0}$ (solid lines) and $\frac{\tau m}{\tau_0}$ (dashed lines)

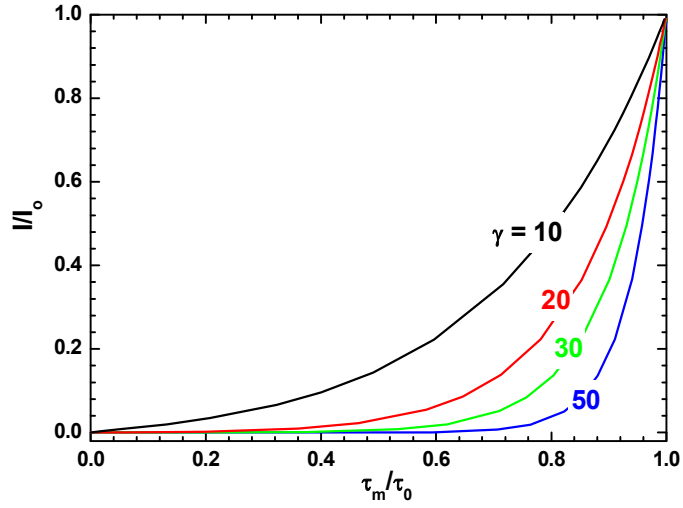

Figure 9: The relative emission intensity of the donor $\frac{I}{I_0}$ vs the decay time $\frac{\tau m}{\tau_0}$ for the exchange interaction. . γ = 10, 20, 30 and 50.

In this study, the numerical calculation and data fitting were performed by using the built-in MATLAB function lisqnonlin [22]. lsqnonlin solves nonlinear least-squares problems, including nonlinear data-fitting problems. This MATLAB function starts at point x_0 and finds a minimum of the sum of squares of the functions described by the user.

For the multipole interaction cases, the parameter to be fitted is c_0. Figure 10 shows the MATLAB code used to fit the multipole interaction data. For the exchange interaction, addition to c_0, γ is also fitted. Figure 11 presents the code used to fit the exchange interaction data.

```
% Define the data sets for the fit (my made up data)
X = [.01 .02 .03 .04 .06 .08 .2 .25 .4 .5 .8];       %Concentrations c
Y = [.93 .82 .69 .61 .48 .35 .17 .14 .09 .09 .05];  %Values of "experimental" I/I0
semilogx(X,Y,'or');              %See data to be fitted
hold on;
% Guess the fit coefficients
x0=[1];
% first one t0=2, but irrelevant as I/I0 does not actually depend on t0
% second one s = 10
% third one c0 = 2

% Set an options file for LSQNONLIN to use the medium-scale algorithm
options = optimset('Largescale','off');

% Calculate the new coefficients using LSQNONLIN
[x,resnorm,residual]=lsqnonlin(@fit_kroon,x0,[],[],options,X,Y);
x   % view fit parameters

%View fitted data
expo = -3:0.1:1.5;  % Concentrations values to get a
c = 10.^expo;       % nice line plot, values not important
fitteddata = relI(c,x(1));
semilogx(c,fitteddata,'r');
%Calculate the standard deviation of residual
STD=std(residual)
```

Figure 10: MATLAB code fits the data to the multipole interaction models.

```
% Define the data sets for the fit (my made up data)
X = [.01 .02 .03 .04 .06 .08 .2 .25 .4 .5 .8];       %Concentrations c
Y = [.93 .82 .69 .61 .48 .35 .17 .14 .09 .09 .05];  %Values of "experimental" I/I0
semilogx(X,Y,'or');              %See data to be fitted
hold on;

% Guess the fit coefficients
x0=[1 5];
% first one t0=2, but irrelevant as I/I0 does not actually depend on t0
% second one s = 10
% third one c0 = 2

% Set an options file for LSQNONLIN to use the medium-scale algorithm
options = optimset('Largescale','off');

% Calculate the new coefficients using LSQNONLIN
[x,resnorm,residual]=lsqnonlin(@fit_kroon,x0,[],[],options,X,Y);
x   % view fit parameters

%View fitted data
expo = -3:0.1:1.5;  % Concentrations values to get a
c = 10.^expo;       % nice line plot, values not important
fitteddata = relI_exch_alt(x(1)c,x(2));
semilogx(c,fitteddata,'r');
%Calculate the standard deviation of residual
STD=std(residual)
```

Figure 11: MATLAB code fits the data to the exchange interaction model.

References

[1] Chow HC and Powell RC 1980 *Phys. Rev. B* **9** 3785

[2] Forster Th. 1948 *Ann. Physik* **2** 55

[3] Dexter DL 1953 *J. Chem. Phys.* **21** 836

[4] Inokuti M and Hirayama F 1965 *J. Chem. Phys.* **43** 1978

[5] Walter JCG 1971 *Phys. Rev.* B **4** 648

[6] Lenth W and Huber G 1981 *Phys. Rev.* B **23** 3877

[7] Bojarski C, Grabowska J, Kulak L and Kusba J 1991 *J. Fluoresc.* **1** 183

[8] Morita M, Buddhudu S, Rau D and Murakami S 2004 *Struct. Bonding* **107** 115

[9] Stavola M and Dexter DL 1979 *Phys. Rev B.* **20** 1867

[10] Martin IR, Rodriguez VD, Rodriguez-Mendoza UR and Lavin V 1999 *J. Chem. Phys.* **111** 1191

[11] Yokota M and Tanimoto1967 O *J. Phys. Soci. Japan* 22 779

[12] Malta OL 1997 *J. Lumin.* **71** 229

[13] Smentek L and Andes Hess BJr 2001 *J. Alloys Compounds* **315** 1

[14] Grether M, Lopez-Moreno E, Murrieta HS, Hernandez JA and Rubio JO 1999 *Optical Mat.* **12** 65

[15] Soos ZG and Powell RC 1972 *Phys. Rev. B* **10** 4035

[16] Lin SH 1973 *Proc. R. Soc. Lond.* **335** 51

[17] Liao DW, Cheng WD, Bigman J, Karni Y, Speiser S and Lin SH 1995 *J. Chinese Chem. Soci.* **42** 177

[18] Melamed NT and Harrison DE 1962 *Westinghouse Research Laboratories* [online]. Available from http://www.dtic.mil/cgi-bin/GetTRDoc?AD=AD0406473 [Accessed 6 June 2012]

[19] Saini S, Singh H and Bagchi B 2006 *J. Chem. Sci*. **118** 23

[20] Dexter energy transfer [online]. Available from http://chemwiki.ucdavis.edu/ Theoretical_Chemistry/Fundamentals/Dexter_Energy_Transfer [Accessed 6 June 2012]

[21] 5.74, Spring 2005: Introductory Quantum Mechanics II [online]. Available from http://www.myoops.org/twocw/mit/NR/rdonlyres/Chemistry/5-74Spring-2005/ 5503C130-4D5D-4DBB-8E8E-51BE9E67514A/0/ps6.pdf [Accessed 6 June 2012]

[22] lsqnonlin [online]. Available from http://www.mathworks.com/help/toolbox /optim/ug/ lsqnonlin.html [Accessed 6 June 2012]

Chapter IV

Research techniques

1. Introduction

Luminescence and related properties of the synthesised phosphors were characterised by six analytic techniques: x-ray diffraction (XRD), Fourier transform infrared spectroscopy (FTIR), ultraviolet–visible spectroscopy (UV-Vis spectroscopy), x-ray photoelectron spectroscopy (XPS), photoluminescence (PL) and cathodoluminescence (CL). XRD was used to determine the crystalline structure and quality of the phase; FTIR to investigate the chemical functional groups; and UV-Vis spectroscopy to detect the absorption positions. XPS was used to explore the atoms in the sample surface and identify the oxidation state of Ce ions. PL and CL were applied to investigate the luminescence characteristics.

2. X-ray diffraction (XRD)

XRD is a technique to determine the structural properties of materials. This technique can inform researchers on the degree of crystallinity, phase identification, lattice parameters, and grain size [1]. The use of the diffraction of waves from the periodic arrangement of atoms in solids to determine the crystal structure was first suggested by Von Laue in 1912, developed by Bragg in 1913 and is now a well-developed science [2]. The typical interatomic distances in solids are a few angstroms [3], so waves with approximately this wavelength are required to explore this structure. The wavelengths of x-rays commonly applied for x-ray diffraction are between 0.7 and 2.3 Å, which is close to the interplanar spacings of most crystalline materials.

2.1 X-ray production

X-rays are a part of the spectrum of electromagnetic radiation in the region between ultraviolet and gamma rays. X-rays have a wavelength between 10.0 and 0.1 Å [4]. They are produced when fast-moving electrons of sufficient energy are decelerated. In an x-ray tube, the high voltage maintained across the electrodes draws electrons toward a

metal target (the anode). X-rays are produced at the point of impact, and radiated in all directions. The kinetic energy of the electrons is transformed into electromagnetic energy (x-rays). Since energy must be conserved, the energy loss results in the release of x-ray photons of energy equal to the energy loss. This process generates a broad band of continuous radiation (called Bremsstrahlung, or braking radiation) as shown in Figure 1.

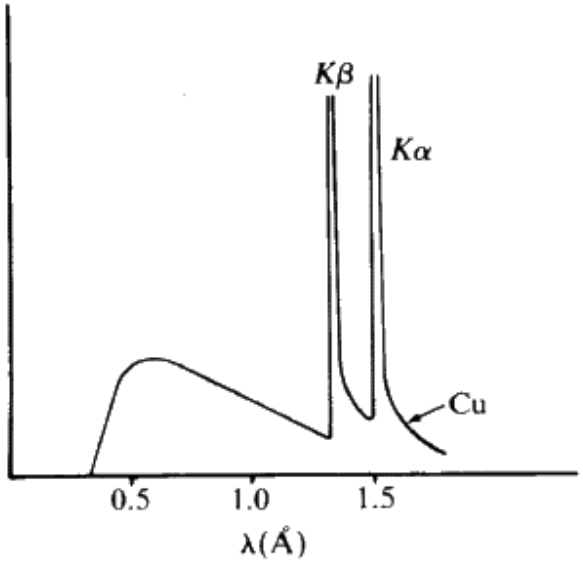

Figure 1: Continuous and characteristic x-rays for copper [5].

If the moving electron interacts with an inner-shell electron of the target atom, characteristic x-rays can be produced. When the moving electron ionizes a target atom by removal of a K-shell electron, transition of an orbital electron from an outer to an inner shell will occur, accompanied by the emission of an x-ray photon. The x-ray photon has energy equal to the difference in the binding energies of the orbital electrons involved. If an L-shell electron moves to replace a K-shell electron, a K_α x-ray is produced (with wavelength 1.54178 Å for Cu). If an M-shell electron moves to replace a K-shell electron, a K_β x-ray is produced (with wavelength 1.39217 Å for Cu). These characteristic x-rays, also shown in Figure 1, are suitable for diffraction experiments. To obtain monochromatic x-rays a suitable metal filter can be used. Nickel strongly absorbs x-rays below 1.5 Å and can be used to filer the K_β x-rays from copper, as shown in Figure 2 [6].

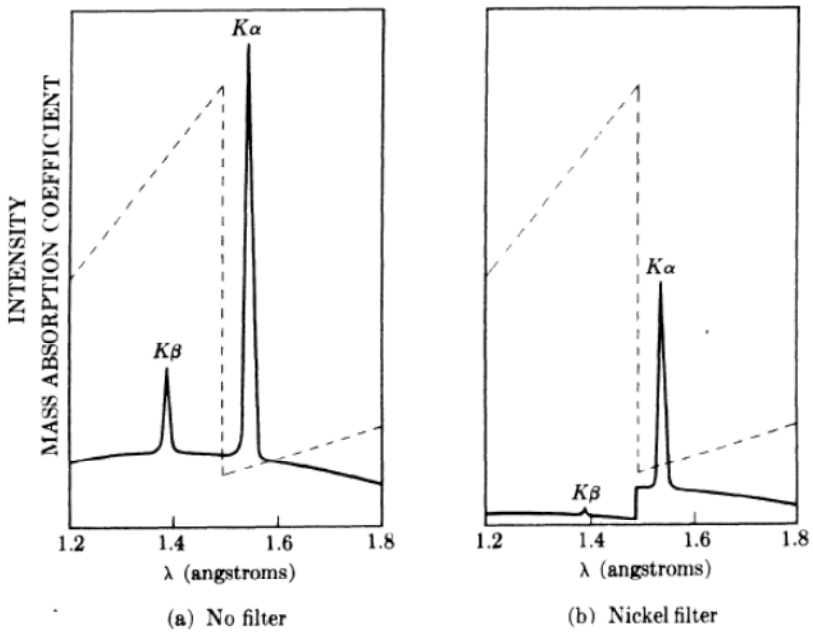

Figure 2: Using a Nickel filter for Cu x-rays [6].

2.2 Bragg's law

X-rays interact primarily with electrons in atoms. When an incident x-ray wave approaches an atom, it is scattered and interference of these scattered waves occur. If the atoms have a periodic arrangement, as in a crystal, the scattering produces a diffraction pattern with sharp maxima (peaks) at certain angles. The peaks in the x-ray diffraction pattern are directly related to the interatomic distances [7].

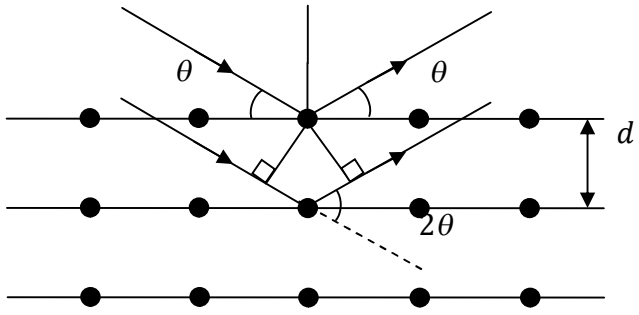

Figure 3: Scattering of x-rays from atoms and Bragg's law.

An incident x-ray beam interacting with the atoms arranged in a periodic manner is shown in two dimensions (2-D) in Figure 3. The atoms can be viewed as forming

different sets of planes in the crystal. For a given set of lattice plane with an interplanar distance of d, the condition for a diffraction (peak) to occur can be written as

$$2d\sin\theta = n\lambda. \quad (1)$$

This is known as Bragg's law, after W.L. Bragg, who first proposed it [8]. In equation 1 θ is the Bragg angle, which is half of the scattering angle; n an integer representing the order of the diffraction peak and λ is the wavelength of the x-rays.

2.3 XRD diffractometer

A diffractometer records the diffraction pattern of a sample. The essential features of a diffractometer are presented schematically in Figure 4 [9].

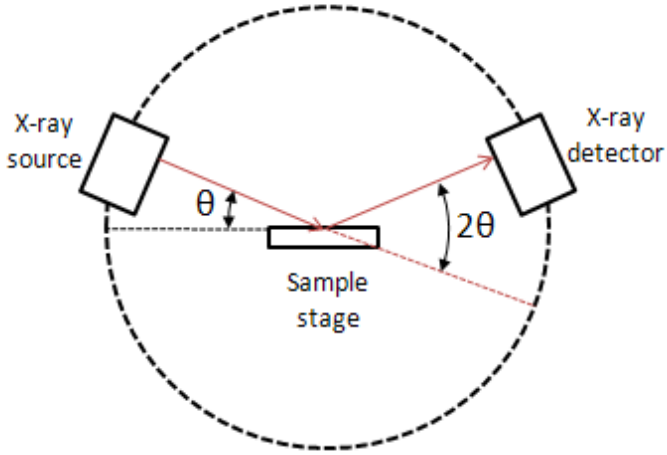

Figure 4: The x-ray diffractometer [9].

It consists of an x-rays source (usually an x-ray tube) producing monochromatic x-rays of known wavelength, a sample stage, a detector, and a way to vary the angle θ. The x-rays are focused on the sample at some angle θ, while the detector reads the intensity of the diffracted x-rays it receives at the scattering angle 2θ.

2.3 XRD applications

With the XRD pattern the identification of an unknown crystalline material becomes possible. Bragg's law is used to convert the angles where peaks occur to interplanar spacings (d-spacings) using Bragg's law (Equation 1). Files of d-spacings for hundreds

of thousands of inorganic compounds for comparison are available in the Powder Diffraction Files (PDF) of the International Centre for Diffraction Data (ICDD).

With the same pattern, the mean crystallite size can be determined. The first scientist that investigated the effect of limited particle size on x-ray diffraction patterns was Paul Scherrer, who in 1918 published what became known as the Scherrer equation [10]

$$\tau = \frac{K\lambda}{\beta cos\theta} \qquad (2)$$

where τ is the mean size cystallites, which may be smaller or equal to the grain size, K is the shape factor, λ is the x-ray wavelength, β is the line broadening at half the maximum intensity (FWHM) in radians, and θ is the Bragg angle.

The XRD data of this study were obtained by a Bruker D8 Advance x-ray diffractometer equipped with a copper anode of x-ray tube (Figure 5).

Figure 5: Bruker D8 Advance x-ray diffractometer.

3. Fourier transform infrared spectroscopy (FTIR)

Fourier Transform Infrared Spectroscopy (FTIR) is an analytical technique which can be used to identify chemical group in organic or inorganic materials. Infrared (IR) light passing through a sample is measured in order to determine the chemical functional groups in the sample. Different functional groups absorb characteristic frequencies of IR radiation. The FTIR spectrometers with especial accessory can measure a wide variety of sample types such as gases, liquids, and solids.

3.1 Infrared region

Infrared rays are a part of the electromagnetic spectrum and cover the range between 0.78 and 1000 μm. The wavelength in infrared spectroscopy is often expressed as the reciprocal of the wavelength in cm, with units cm^{-1}. For convenience the infrared region can be divided into three parts: near, mid and far infrared (Table 1). The part of the mid infrared region between 4000 – 670 cm^{-1} is the most useful one [11].

Table 1: Three sections of IR

Region	Wavelength range (μm)	Wavenumber range (cm^{-1})
Near	0.78 - 2.5	12800 - 4000
Mid	2.5 - 50	4000 - 200
Far	50 -1000	200 - 10

3.2 Physical principles

The physical principles of the FTIR discussed for molecules in [12]: “Molecular bonds vibrate at various frequencies depending on the elements and the type of bonds. For any given bond, there are several specific frequencies at which it can vibrate. According to quantum mechanics, these frequencies correspond to the ground state (lowest frequency) and several excited states (higher frequencies). One way to increase the frequency of a molecular vibration is to excite the bond by having it absorb light energy. For any given transition between two states the light energy must equal the difference in the energy between the two states exactly (usually ground state (E_0) and the first excited state (E_1)).

The energy corresponding to these transitions...” “...corresponds to the infrared portion of the electromagnetic spectrum. Thus absorption of IR is restricted to vibrational states. For a molecule to absorb IR, the vibrations within a molecule must cause a net change in the dipole moment of the molecule. The alternating electrical field of the radiation interacts with fluctuations in the dipole moment of the molecule. If the frequency of the radiation matches the vibrational frequency of the molecule, then radiation will be absorbed, causing a change in the amplitude of molecular vibration.” In solids the same principles apply, but the vibrations of the lattice instead of individual molecules must be considered.

3.3 Sample preparation

Powder samples for FTIR can be mixed with potassium bromide (KBr) which is transparent in the IR to form a fine powder which is then compressed into a thin pellet to be analyzed. The thickness of the pellet and the ratio between the KBr and the powder sample can affect the peak intensity and broadness. Figure 6 shows two FTIR spectra of KBr pellets with different thickness and two FTIR spectra of pure silica with different ratios to the KBr. For a more reliable analysis the ratio between the KBr and the powder sample should be fixed for all measurements.

Due to the hygroscopicity of the KBr, FTIR spectra may show distinct differences in peak intensity of water and hydroxyl groups, according to the amount of water absorbed by KBr in different laboratory environments. Figure 7 shows two FTIR spectra of SiO_2:Ce 4 mol% taken on two occasions. The second reading shows stronger absorbtion due to hydroxyl groups. It is better to dry the KBr at 120ºC for 3h [13] before using it. All measurement should be taken in the same condition.

3.4 Material identification

The material being analysed can be identified by comparing its spectrum with the databases of the standard spectra obtained from known materials. The absorption bands lying between 4000 - 1500 cm^{-1} are generally associated with the functional groups such as OH, C=O, N-H, CH3. The absorption bands in the region from 1500 - 400 cm^{-1} are more specific to their materials [14] and considered as the fingerprint region. These bands used to identify a material.

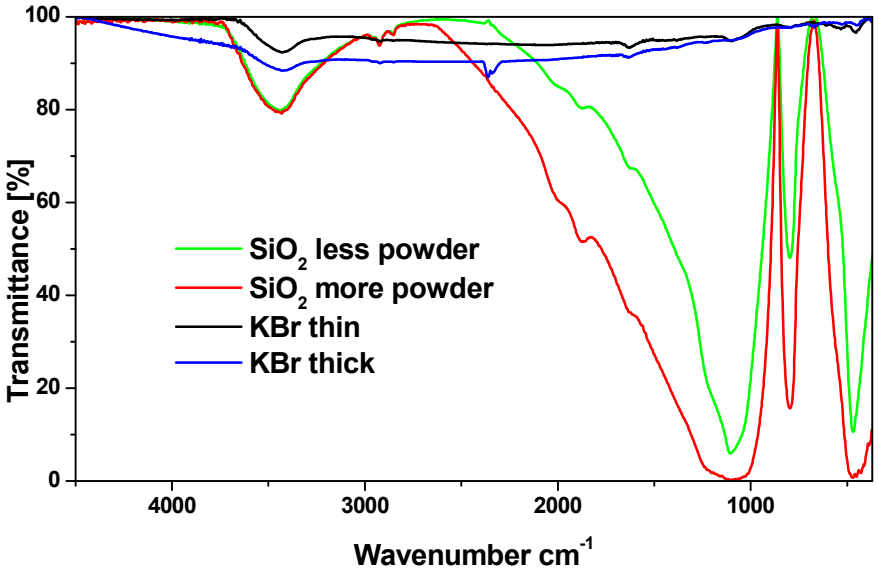

Figure 6: FTIR measurements showing the effect of the thickness of the pellet and the ratio between the KBr and the powder.

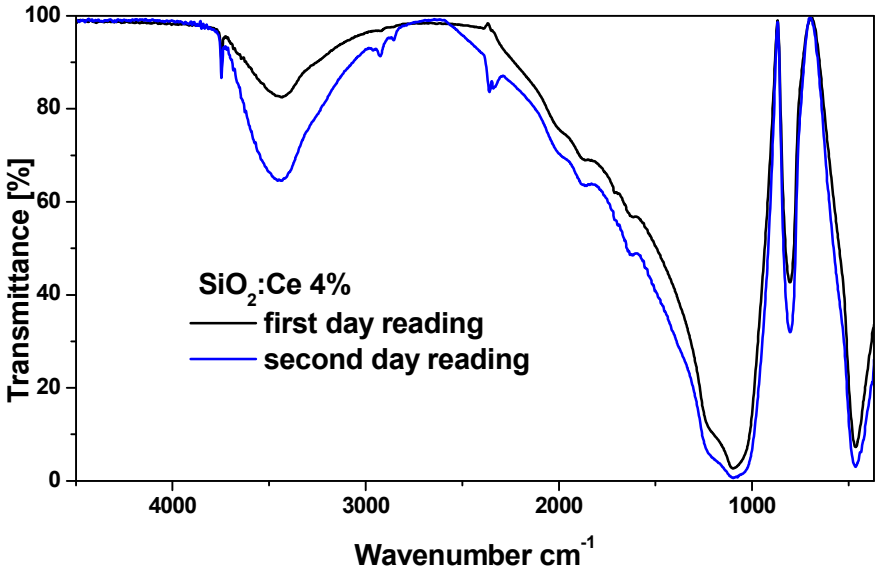

Figure 7: FTIR spectra of the same SiO_2:Ce 4 mol% taken on two occasion.

3.5 Description of the spectrometer

The basic components a spectrometer are an IR source and an interferometer with detector. The IR light passes from the source through the sample and into the interferometer, where the interferogram is recorded by the detector as a mirror is moved. To obtain the infrared spectrum, a computer uses a Fourier transform to decode the interferogram. The FTIR spectra can be plotted in transmittance or absorbance mode. A schematic diagram [15] and photo of a typical Bruker Tensor 27 FTIR spectrometer used in this study are shown in Figure 8.

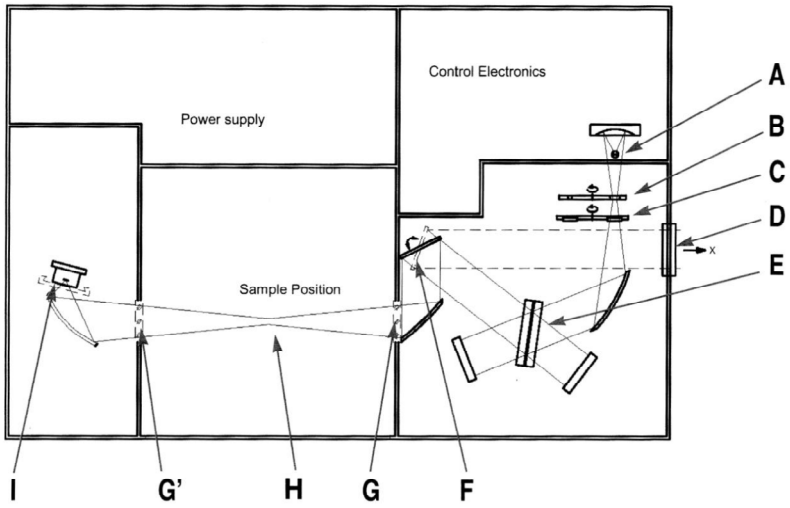

(a)

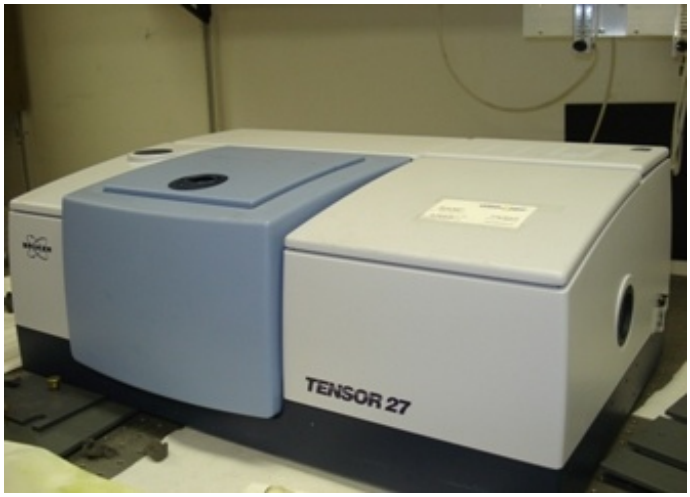

(b)

Figure 8: (a) Tensor 27 optical bench, IR beam path, and major components. A is the mid-IR source, B is the aperature wheel, C is the filter wheel, D is the exit port, E is the beamsplitter, F is the switch mirror, G and G' are the sample compartment windows (KBr), H is the sample holder/cell, I is the detector [15]. (b) Bruker Tensor 27 FTIR spectrometer.

4. UV-Vis spectroscopy

UV-Vis spectroscopy is the measurement of the wavelength and the intensity of absorption of ultraviolet and visible light after it passes through a sample or after reflection from a sample surface. Transmission or absorption measurements can be done for liquid samples or transparent solid samples. Diffuse reflectance measurements can be done by integrating sphere for powder samples.

4.1 Definitions

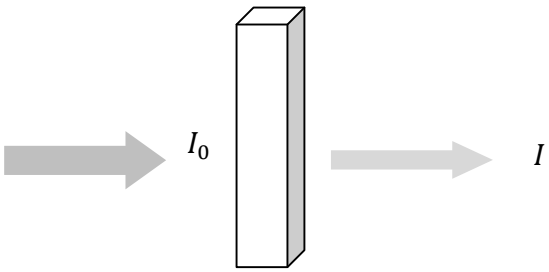

Figure 9: Incident and transmitted light.

When a light of intensity I_0 falls upon a transparent material, as illustrated in Figure 9, some of the light will be absorbed by the material, some will be scattered and reflected and some will be transmitted. Two related quantities can be defined as follows:

Transmittance (T) is the ratio between the radiation transmitted through a material and the radiation falling upon it

$$T = \frac{I}{I_0}, \tag{3}$$

while absorbance (A) is the logarithmic ratio between the radiation falling upon a material and the radiation transmitted through it

$$A = \log\frac{I_0}{I}. \tag{4}$$

4.2 Physical principles

A good description for UV-Vis spectroscopy principles is given in [16]: "The absorption process depends on an atomic structure in which each of the electrons of an atom has an energy level associated with its position in the atom. Permitted energy levels are finite and well defined, but an electron may be made to change to another level if a quantum of energy is delivered equal to the energy difference between the two levels. The original level is called the ground state and the induced level is known as the excited state. Excited states are generally unstable and the electron will rapidly revert to the ground state, losing the acquired energy in the process. Because each electron in a molecule has an unique ground state energy, and because the discrete levels to which it may jump are also unique, it follows that there will be a finite and predictable set of transitions for the electrons of a given molecule. Each of the transitions, or jumps, requires the absorption of a quantum of energy. If that energy is derived from electromagnetic radiation, there will be a direct and permanent relationship between the wavelength of the radiation and the particular transition that it stimulates. That relationship is known as specific absorption. A plot of these points along the wavelength scale at which a given substance shows absorption peaks, or maxima, is called an absorption spectrum."

4.3 Instrumentation

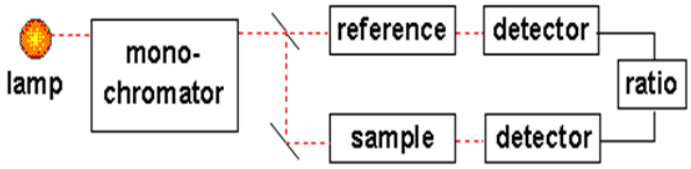

Figure 10: A dual-beam UV-Vis spectrophotometer[17].

The minimum requirements are the source, a monochromator and a detector. The light source is usually a deuterium lamp for UV measurements and a tungsten lamp for visible measurements [17]. The function of a monochromator is to produce a beam of monochromatic (single wavelength) radiation selected from a wide range of wavelengths. First a background scan is recorded without the sample present, and then the light passing through the sample is compared to a reference beam (Figure 10) to obtain the ratio (I/I_0), which does not depend in changes of the incident light intensity.

4.4 Diffuse reflectance measurements

For diffuse reflectance measurements the UV/Vis instrument must be equipped with an integrating sphere coated with a white standard, intended to collect the light reflected by the standard and the sample. Modern double-beam spectrophotometers are equipped with holders in which the powdered sample and the white standard are tightly packed. The standard is usually $BaSO_4$, MgO, or polytetrafluoroethylene (PTFE) [18]. They exhibit near 100% reflectance in the wavelength range from the near UV to the near IR. Our diffuse reflectance spectra were recorded by a Lambda 950 UV–Vis spectrophotometer with an integrating sphere (Figure 11). The standard used was spectralon.

Figure 11: Lambda 950 UV-Vis spectrophotometer.

5. X-ray photoelectron spectroscopy (XPS)

X-ray Photoelectron spectroscopy (XPS), also known as Electron Spectroscopy for Chemical Analysis (ESCA), is used to investigate the chemical composition of surfaces [19]. The technique utilises a photo-ionisation and analyses the kinetic energy distribution of the emitted photoelectrons from a surface. Monochromatic x-ray sources are use as excitation. Mg K_α radiation (1253.6 eV) or Al K_α radiation (1486.6 eV) are often used [19]. Due to the very short path of the photoelectrons excited from the solid, the XPS is considered as a surface-analytical technique. The photoelectrons leaving the sample are detected by a concentric hemispherical analyser (CHA). This gives a spectrum with a series of photoelectron peaks. The binding energy of the peaks is characteristic of

each element. The peak areas can indicate the relative concentration on the material surface. The shape of each peak and the binding energy can be slightly altered by the chemical state of the emitting atom. Hence, XPS can provide chemical bonding information as well.

5.1 Physical principles

The technique is based on Einstein's explanation of the photoelectric effect. The photon is absorbed by an atom or a molecule in solid, followed by an emission of a core electron. The kinetic energies of the emitted electrons (KE') is given by

$$KE' = h\nu - BE - \phi \tag{5}$$

where $h\nu$ is the energy of the photon, BE is the binding energy of the atomic orbital from which the electron originates and ϕ is the sample work function.If the spectrometer and the sample are grounded, then the zero energy level of BE will be aligned as illustrated in Figure 11.

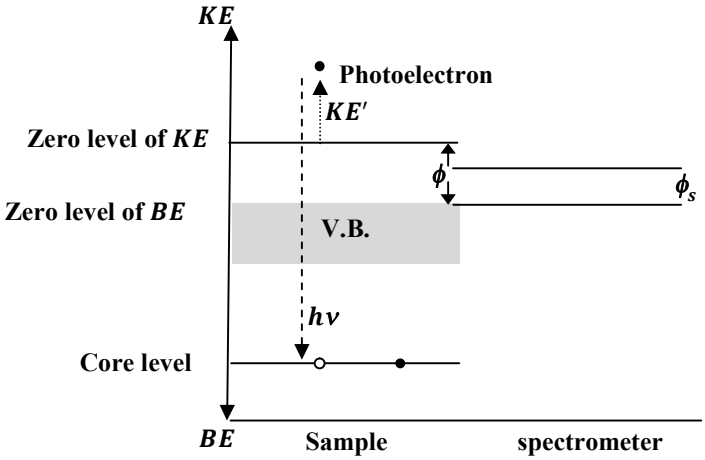

Figure 12: Zero level of BE and KE for grounded sample and the spectrometer.

The KE of the photoelectron relative to zero level of the spectrometer is given by

$$KE' = KE - (\phi - \phi_s) \tag{6}$$

where ϕ_s is the work function of the spectrometer. By substituting 6 in 5, one gets

$$BE = h\nu - KE - \phi_s. \tag{7}$$

For the known photon energy $h\nu$, the binding energy can be determined. With an electron analyzer, the photoelectron spectrum of different binding energies can be recorded by scanning the kinetic energies.

The unique set of binding energies for each element allows one to identify and determine the concentration of the elements on the surface by XPS. In addition to photoelectrons, Auger electrons may also be emitted as result of relaxation of the excited ions remaining after photoemission. Figure 13 shows the XPS and Auger emission process for a model atom [19].

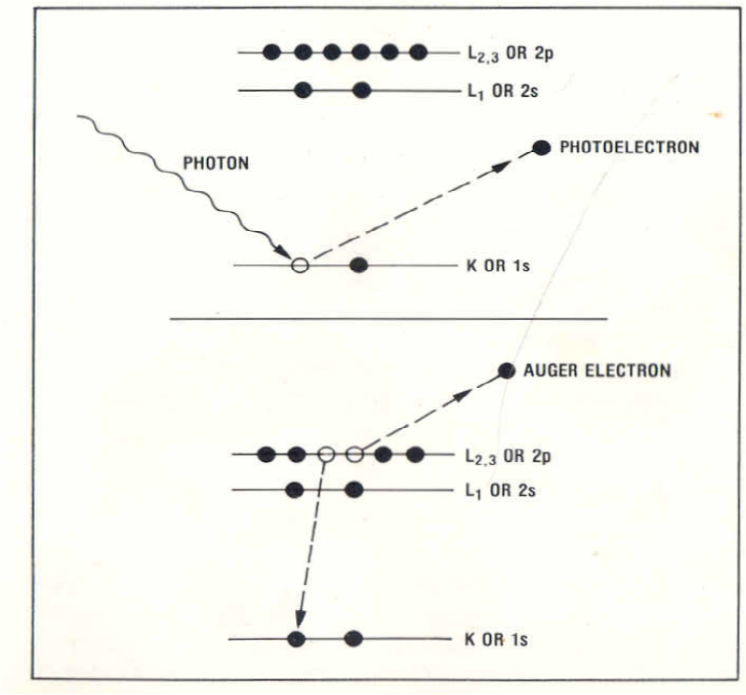

Figure 13: The XPS process (top) and the Auger process (bottom) [19].

5.2 XPS spectrometer

The basic requirements of the XPS spectrometer are an x-ray source, an electron energy analyser and a high vacuum environment. Such a system is illustrated schematically in Figure 14 [20] and a description of every part is given below.

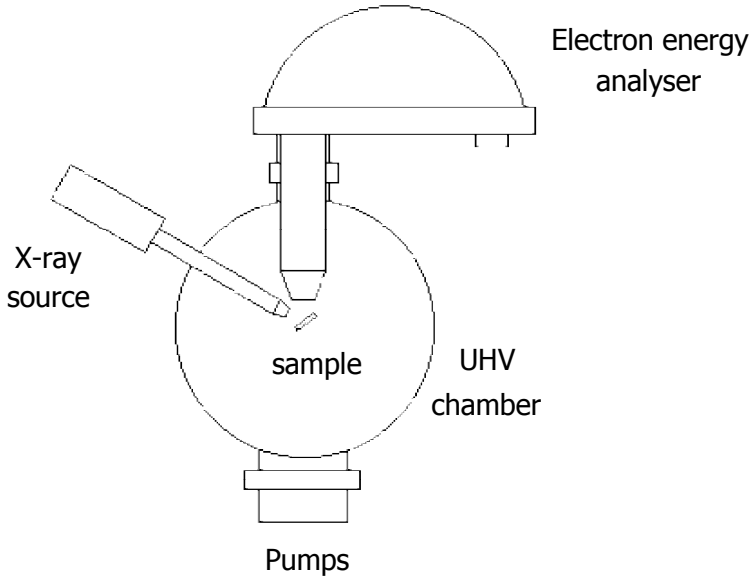

Figure 14: The XPS spectrometer [20].

5.2.1 X-ray source

The source consists of a cathode and an anode. The cathode emits electrons through heating. The emitted electrons are accelerated through a high voltage (about 15 kV) towards the anode. Mg and Al are often used as the anode material.

5.2.2 Electron energy analyser

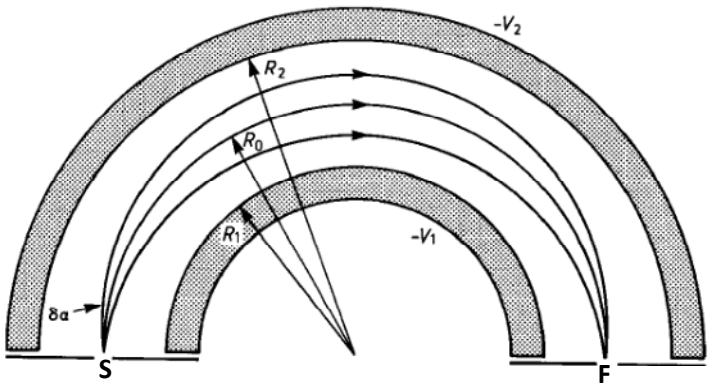

Figure 15: The concentric hemispherical analyser (CHA) [21].

The electron energy analyser, called a concentric hemispherical analyser (CHA), is shown in Figure 15 and described in [21]: It "consists of two precision machined stainless steel hemispheres positioned concentrically. The two hemispheres are the radii, R_1 (inner hemisphere) and R_2 (outer hemisphere). Negative potentials are applied to both

hemispheres with V_2 being greater than V_1. The median equipotential surface between the hemispheres have a value, V_0 given by $V_0 = (V_1R_1 + V_2R_2)/2R_0$ where R_0 is the radius of the median equipotential surface. This means that an electron entering through slit S with a kinetic energy $E = eV_0$ follows the trajectory through the analyzer along the median equipotential surface of radius R_0 and focuses at the exit slit, F. Likewise, electrons entering at S with a kinetic energy not equal to eV_0 follow a different trajectory and will not focus at F. Because R_0, R_1, and R_2 are fixed, changing V_1 and V_2 selectively passes electrons of varying kinetic energies through the analyzer. In XPS and occasionally in AES, scanning the voltages V_1 and V_2 of the hemispheres is generally not practiced because of the need to have the same absolute resolution, ΔE, at all energies in the spectrum. The easy way to achieve this constant absolute resolution is by retarding the electrons to a fixed kinetic energy immediately before they enter the energy analyzer. This fixed kinetic energy is called the pass energy, E_0, so that fixed resolution applies across the entire spectrum. The electrostatic lens system provides this function of retarding the electrons to the correct pass energy."

5.2.3 Vacuum chamber

The sample analysis conducts in a vacuum chamber, under the best vacuum conditions achievable, typically $\sim 10^{-9}$ torr. This facilitates the transmission of the photoelectrons to the analyser but, more importantly, minimises the re-contamination rate of a freshly cleaned sample. This is crucial because XPS is very surface-sensitive, with a typical sampling depth of only a few nanometers. The vacuum is obtains by using a turbo pump which can reach $\sim 10^{-6}$ torr, follows by an ion pump.

5.3 Experimental procedure

Solid samples can be attached mechanically to the specimen holder. Conducting tape may be used for powder samples. The instrument may need calibration. The Au 4f and/or Cu 2p peaks are often used to calibrate the spectrometer. For non conducting samples, photoelectron peaks may shift due to charging on the sample surface during x-ray excitation. This charging shift can be corrected by using a known peak position in the spectrum. In this study, the peak position shift was corrected using the known values of the C1s (284.5 eV) peak and/or the Si2p (103.3 eV) peak.

5.4 Photoelectron spectra and their interpretation

The photoelectron of every element has a characteristic binding energy associated with each core atomic orbital. Thus the presence of particular peaks in the XPS spectrum indicates the presence of specific elements in the sample. In addition, the intensity of the peaks is related to the concentration of the element within the sampled region. Thus, the technique provides quantitative data of the surface composition

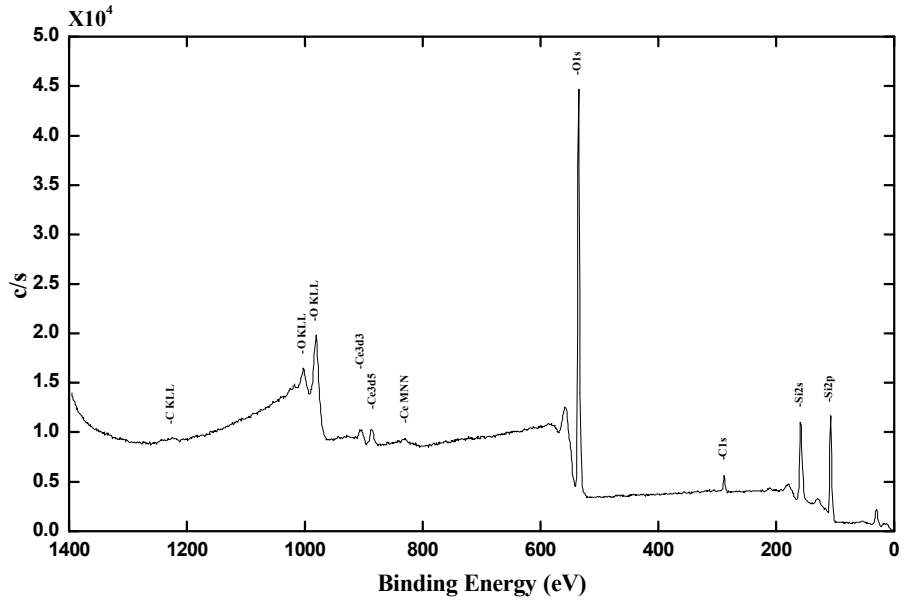

Figure 16: XPS survey scan of SiO_2 doped with Ce (4 mol%).

Survey and high resolution scan are the two ways for collecting photoelectron spectra. Survey scans obtain at high pass energy (high count rate but low resolution) and over the entire useful range of binding energies accessible with the x-ray source employed. Survey scans identify the elemental composition of each element through its core electron. Figure 16 shows an example of the survey scan spectrum of SiO_2:Ce, obtained with pass energy of 187 eV. By using some software (e.g. MultiPak) or an XPS database one can identify the elements on the sample surface.

High resolution scans are collected at low pass energy (lower count rate but higher resolution). The detailed line shape allows individual chemical shifts to be determined.

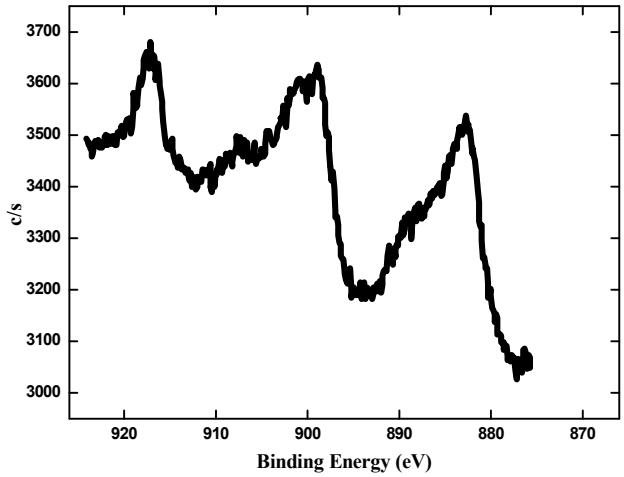

Figure 17: XPS high resolution scan of the Ce peaks of Figure 16

Figure 17 shows an example of a high resolution scan spectrum of SiO_2:Ce sample obtained by pass energy of 11.8 eV. The peaks were scanned within the range of 870-930 eV and are associated with Ce 3d photoelectrons. By using software the spectrum can be fitted with 10 peaks and a relative concentration of Ce^{4+} and Ce^{3+} can be determined. More details of this procedure are given in Chapter IX.

XPS data were collected by two different spectrometers, PHI 5400 ESCA and PHI 5000 Versaprobe, both are using Al x-ray. Figure 18 shows the PHI 5000 XPS spectrometer.

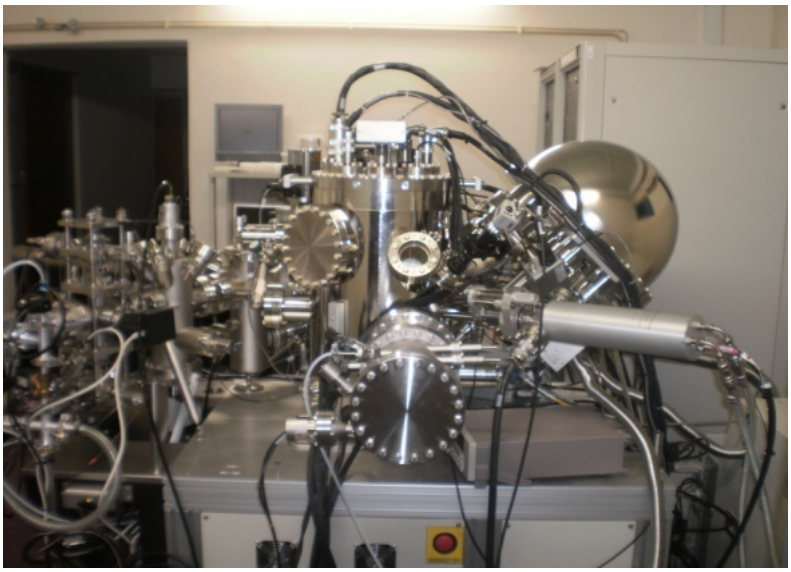

Figure 18: PHI 5000 XPS spectrometer.

6. Photoluminescence spectroscopy (PL)

Photoluminescence spectroscopy is analytical technique that can determine quantities such as emission and excitation spectra and luminescence lifetimes. By this technique, a sample is excited by photons (generally in UV range) and the excess energy released by the sample through the emission of light can be detected and recorded for different modes, i.e. excitation, emission and luminescence decay lifetime.

A spectrofluorometer is an instrument capable of recording the emission spectrum or both the excitation and emission spectra. An emission spectrum is the wavelength distribution of an emission measured at a single constant excitation wavelength. An excitation spectrum is the dependence of emission intensity, measured at a single emission wavelength, upon scanning the excitation wavelength. With a pulsed excitation source and a fast detector the spectrofluorometer can record the luminescence lifetime decay curve. A fluorescence decay time is a measurement, at fixed wavelength, of fluorescence signals as a function of time. A decay curve is a spectrum measured within a narrow time-window during the decay of the fluorescence of interest. Two requirements for lifetime measurements are a pulsed excitation source (pulse duration short in comparison with the excited-state lifetime of the molecule) and a fast detector.

6.1 Physical principles

In photoluminescence spectroscopy, the species is first excited (by absorbing a photon) from its ground electronic state to one of the various vibrational states in the excited electronic state. Collisions with other molecules cause the excited molecule to lose vibrational energy until it reaches the lowest vibrational state of the excited electronic state. The molecule then drops down to one of the vibrational levels of the ground electronic state, emitting a photon in the process. As molecules may drop down into any of several vibrational levels in the ground state, the emitted photons will have different energies. These processes are often visualised with the Jablonski diagram shown in Figure 19.

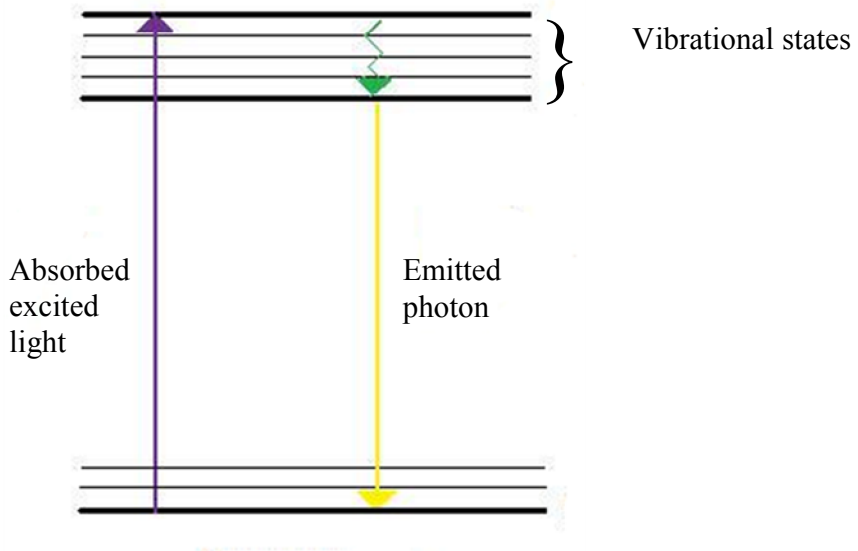

Figure 19: The Jablonski diagram.

6.2 Instrumentation

Four essential elements constituting the spectrofluorometer are illustrated in Figure 20.

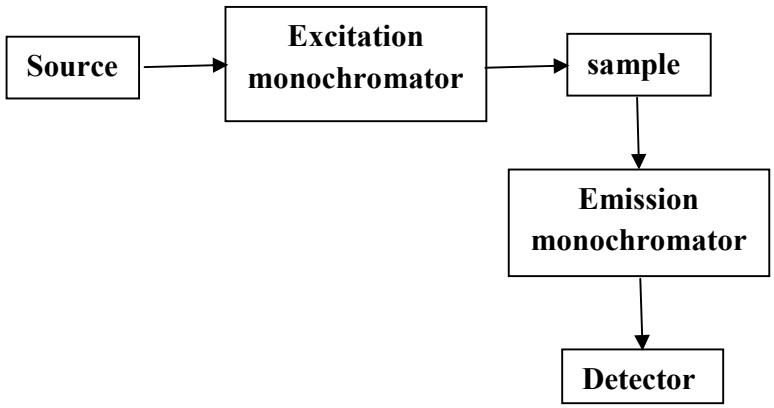

Figure 20: Spectrofluorometer using conventional right-angle collection.

The source produces light photons. Various light sources may be used as excitation sources, including lasers, photodiodes, and lamps. Photons impinge on the excitation monochromator, which selectively transmits light in a narrow range around the specified excitation wavelength. With a laser excitation sources, filters may be used instead of a monochromator, or with a monochromator to give high quality monochromatic light. The

transmitted light passes through adjustable slits that control intensity and resolution by further limiting the range of transmitted light. The filtered light passes into the sample. Emitted light goes through a filter to prevent the excitation light entering the detector and causing second order peaks. The filtered light then enters the emission monochromator, which is often positioned at a 90º angle from the excitation light path to eliminate background signal and minimize noise due to stray light. Again, emitted light is transmitted in a narrow range centred on the specified emission wavelength and exits through adjustable slits, finally entering the photomultiplier tube (PMT). Figure 21 shows the two systems used to collect our data: (a) the Cary Eclipse fluorescence spectrophotometer, and (b) the 325 nm He-Cd laser PL system.


(a)


(b)

Figure 21: (a) 325 nm He-Cd laser PL systems. (b) Cary Eclipse fluorescence spectrophotometer.

A narrow filter was used instead of an excitation monochromator with the laser PL system, since the laser may produce some lines in addition to 325 nm. The Cary Eclipse is equipped with a xenon lamp to produce a wide spectrum range between 200 and 1100 nm. The monochromator and built-in filters with generally yielded good monochromatic light. However, when exciting between 200 and 300 nm, the Cary Eclipse detecting some peaks that were not the result of luminescence from the samples. These peaks occurred for all samples and we attribute them to characteristic peaks from the Xe lamp which are not effectively removed by the monochromator, and are therefore visible in the spectrum. They were especially apparent if the sample itself was poorly luminescent and hence a high voltage was applied to the photomultiplier. External filters (Figure 22) were placed between the source and sample to eliminate these peaks.

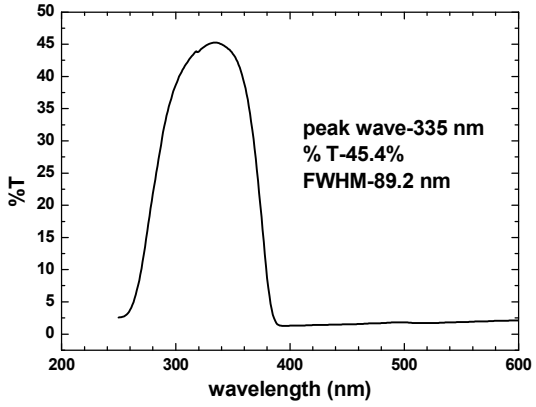

(a)

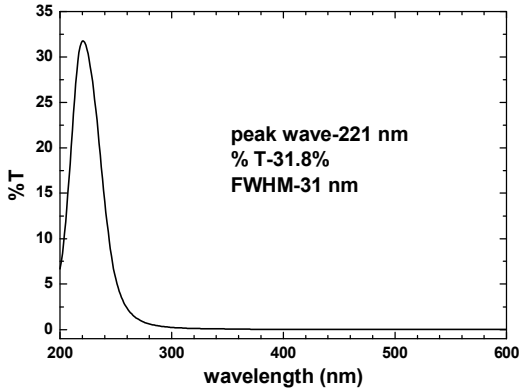

(b)

Figure 22: The transmission spectra of the two filters used for excitation.

Figure 23 (a) present the excitation and emission spectra of LaF_3:Ce excited with 232 nm measured without the filter and (b) with the filter. The peaks due to the Xe lamp (between 400 and 500 nm) were eliminated when the filter was used.

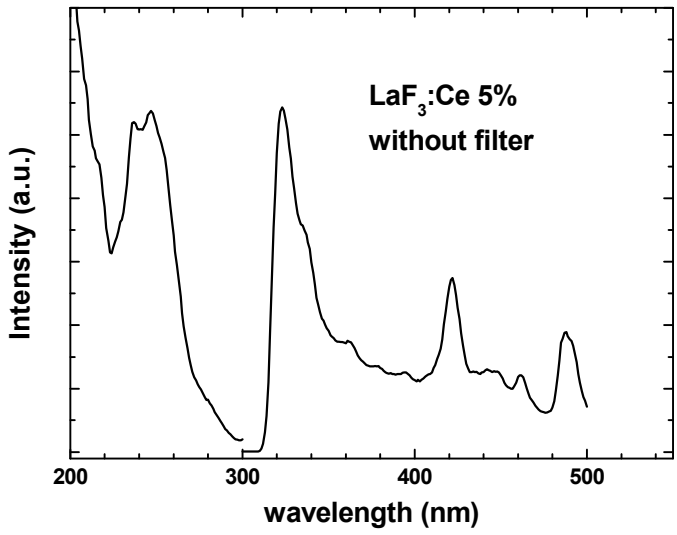

(a)

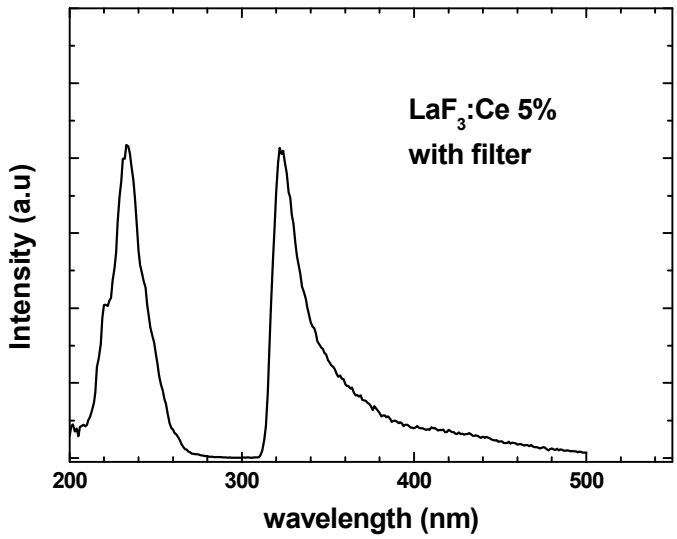

(b)

Figure 23: Excitation and emission spectra of LaF_3:Ce (a) without filter (b) with filter.

With the excitation wavelength between 200 and 300 nm, Cary Eclipse also has no suitable built-in filters that can be used on the detector side to stop second order peaks. In this range we used a sheet of plastic transparency (for use with an overhead projector), which blocked UV light having a wavelength less than 315 nm but allowed longer wavelengths through. Figure 24 shows the transmission spectrum of the sheet which prevented the second order peaks if the excitation wavelength is less than 315 nm. Fortunately, with the excitation wavelength higher than 315 nm, the build-in filters work well. Note that in Figure 23(b) this transparency filter is blocking part of the Ce luminescence near 300 nm, giving the emission peak its asymmetrical shape.

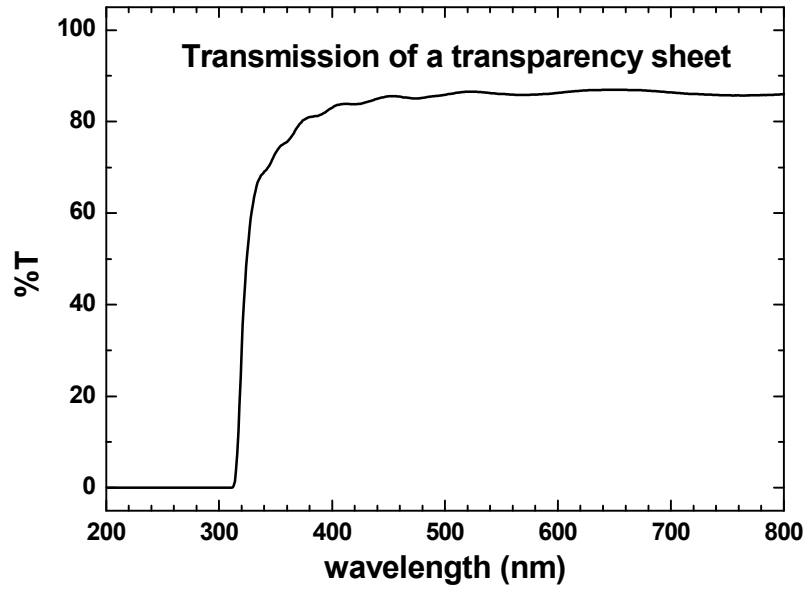

Figure 24: The transmission spectrum of the transparency sheet.

The Cary Eclipse is designed to work in fluorescence or phosphorescence mode individually, i.e. it cannot collect a fluorescence spectrum when it was used in phosphorescence mode and vice versa.

7. Cathodoluminescence spectroscopy (CL)

Cathodoluminescence (CL) is the emission of photons from a specimen excited by an electron beam. An example of the CL process is the screen of a television cathode ray tube (CRT) monitor. Due to the interaction of the beam with the specimen, different electromagnetic waves and electrons are generated: UV, IR, visible light, x-rays, secondary electrons, Auger electrons and back-scattered electrons. These are illustrated in Figure 25 [22].

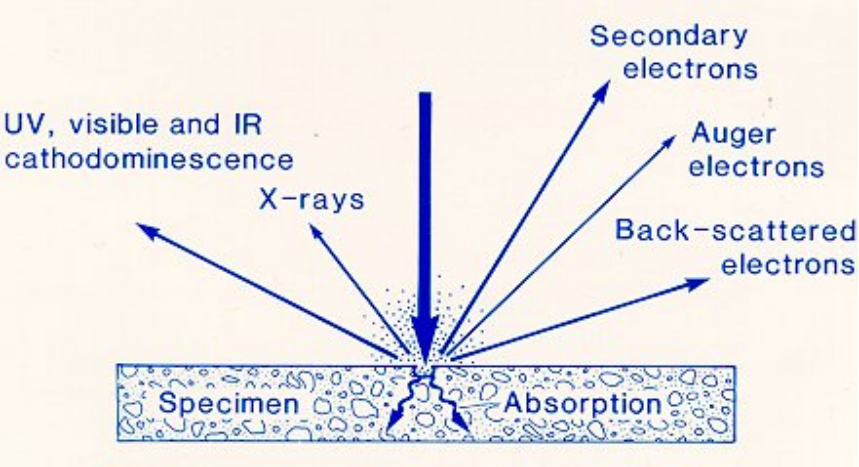

Figure 25: The energies produced from elecron beam interaction with solid matter [22].

7.1 Physical principles

The band theory of solids provides a way to explain the CL emission. An insulating solid material (such as SiO_2) has a valence band and a conduction band with an intervening band gap (see Figure 26). If a material is bombarded by electrons with sufficient energy, electrons from the lower-energy valence band are promoted to the higher-energy conduction band forming electron-holes pairs (EHs pairs). These EHs pairs may be temporarily trapped by intrinsic (structural defects) or extrinsic (impurities) luminescent centres, or both. The luminescence emission occurs as result of the recombination of EHs pairs in such centres.

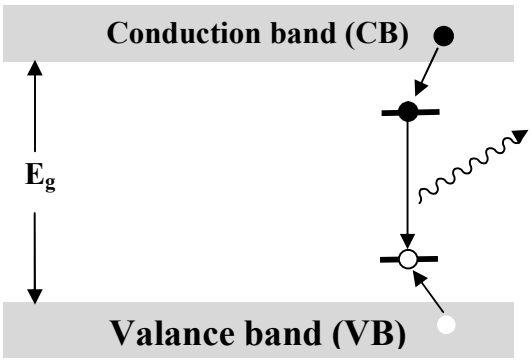

Figure 26: The process causing CL emission.

7.2 Instrumentation

The basic components of the CL spectrometer are similar to the XPS spectrometer, changing only the x-ray source to an electron gun and the electron energy analyser to a spectrometer. The electron gun was used to accelerate electrons through high voltage, typically 2-5 kV. A spectrometer and computer were used to collect and plot the spectra. Cathodoluminescence data for this study were collected by two systems: a PHI Model 549 Auger system with S2000 spectrometer and a Preparation chamber from PREVAC equipped with an ES40C electron gun unit and USB2000+ spectrometer. The two systems are shown in Figure 27.

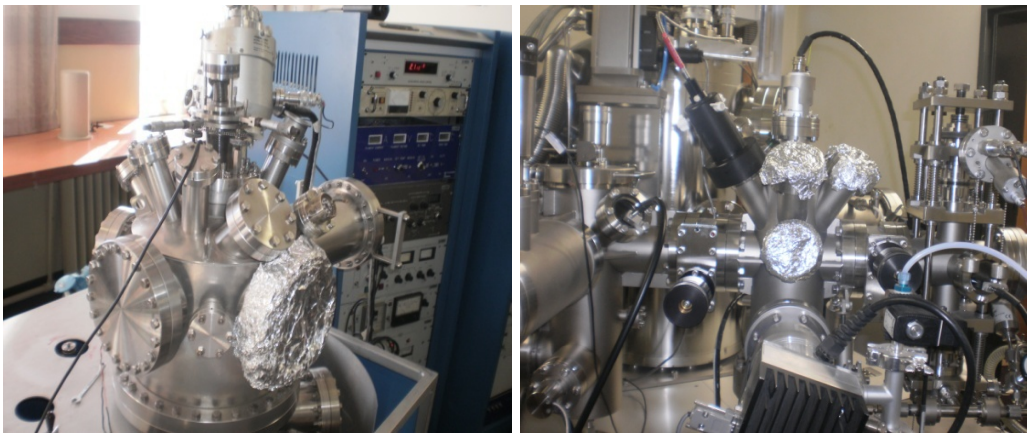

(a) (b)

Figure 27: (a) PHI 549 Auger system, and (b) PREVAC system for collecting CL spectra.

7.3 Samples preparation and measurements

For the PHI 549 Auger system, the powder samples are pressed in small holes (around 1 mm diameter) in a copper holder attached to a head. Five holders and the Faraday cup were placed in the head. The function of the Faraday cup is to measure the current beam size. Then the head was introduced into the vacuum chamber. We waited for the desired vacuum, and then accelerated the electrons towards the sample. The CL spectrum can be collected with a spectrometer and recorded by a computer.

To determine the electron beam size, the beam current was measured while moving the edge of the Faraday cub perpendicular to the electron beam. The beam current as function of the distance moved by the edge of the Faraday cup was differentiated and plotted. The diameter of the electron beam is taken as the width at half-maximum. The plot of the beam current against moving distance is illustrated in Figure 28(a). Figure 28(b) shows the differentiated current as a function of moving distance of the edge of the Faraday cup. The electron beam size was found to be around 184 μm.

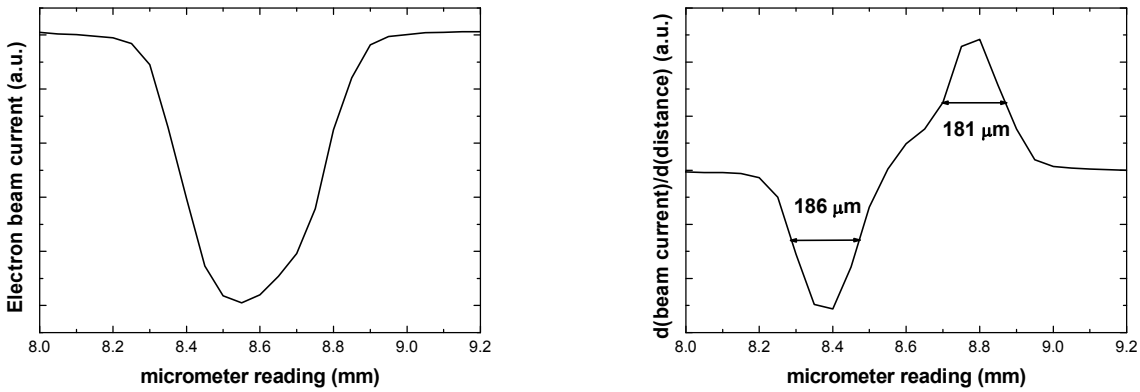

Figure 28: (a) The beam current against moving distance of the edge of the Faraday cup. (b) The differentiated current as a function of moving distance of the edge of the Faraday cup.

For the PREVAC system, the powder samples attached to the horizontal sample holder using carbon tape. The holder introduced into an ultra high vacuum (UHV) chamber. The Preparation chamber from PREVAC was attached to the PHI 5000 Versaprobe XPS and equipped with an ES40C electron gun unit. The electron beam was directed upon

different samples by changing the voltage on the XY deflection plates using the electron gun controller. The CL emission collected by USB2000+ spectrometer. The spectrometer calibration was checked by using the known wavelengths of a Cd spectral lamp. The spectrum of the Cd lamp (Figure 29) confirmed that the spectrometer is well-calibrated, and also shows that the resolution of the spectrometer is about 10 nm.

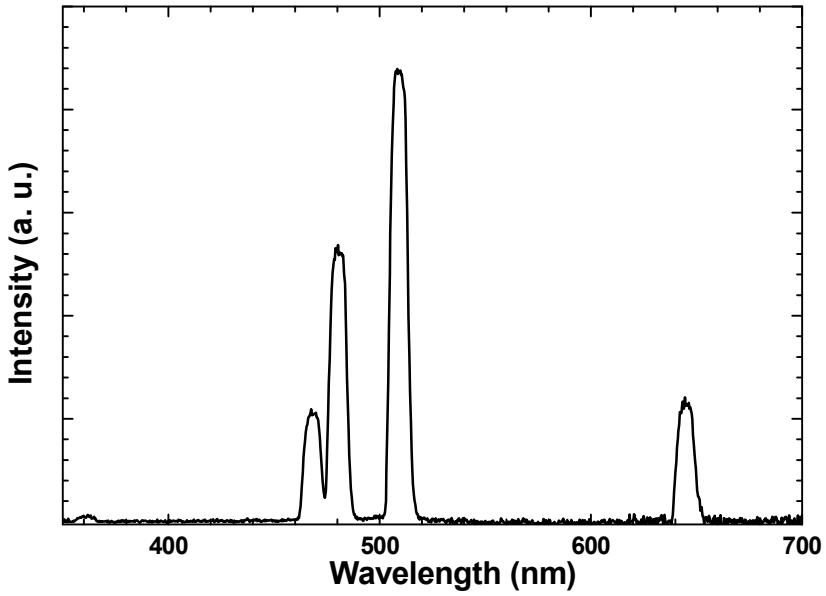

Figure 29: Cd lamp spectrum recorded by USB2000+ spectrometer.

The advantage of the PREVAC system over the PHI 549 Auger system is that the electron beam scans the fixed horizontal samples giving higher opportunity for comparing the CL emission intensities. But the advantage of the PHI 549 Auger system over the PREVAC system is the capability of the PHI 549 Auger system to measure the Auger spectrum and the beam current size which are necessary for degradation measurements.

References

[1] Cost-Effective Analysis of Industrial Minerals, [online]. Available from http://www.bruker-xs.de/fileadmin/user_upload/KJR_Files/Bruker_AXS_Industrial Minerals_Webinar_Presentation_2007-07-19.pdf [Accessed 21 May 2012].

[2] Burns G 1985 *Solid state physics* (Florida: Academic press, Inc)

[3] Ashcroft NW and Mermin ND 1976 *Solid State Physics* (Philadelphia: Saunders College).

[4] Connolly R Introduction to X-ray Powder Diffraction,[online]. Available from http://epswww.unm.edu/xrd/xrdclass/01-XRD-Intro.pdf [Accessed 21 May 2012]

[5] X Ray Generation, [online]. Available from: http://xrayweb.chem.ou.edu/notes/ xray.html [Accessed 21 May 2012]

[6] Cullity BD 1956 *Elements of x-ray diffraction* (Reading: Addison Wesley) p. 16

[7] Introduction to X-ray Diffraction [online]. Available from http://www.mrl.ucsb. edu/mrl/centralfacilities/xray/xray-basics/index.html [Accessed 21 May 2012]

[8] Kittel C 1971 *Introduction to Solid State Physics* (New York: Wiley)

[9] Powder X-ray Diffraction, [online]. Available from http://chemwiki.ucdavis.edu/A nalytical_Chemistry/Instrumental_Analysis/Diffraction/Powder_X-ray_ Diffraction [Accessed 31 May 2012].

[10] Scherrer P and Gottingen NGW 1918 *Math-Pys. Kl.* **2** 96

[11] Infrared absorption spectroscopy – theoretical principles, [online]. Available from http://teaching.shu.ac.uk/hwb/chemistry/tutorials/molspec/irspec1.htm [Accessed 21 May 2012]

[12] Fourier Transform Infrared Spectroscopy , [online]. Available from http://www.exova.com/pharma-technical-articles/250-fourier-transform-infrared-spectroscopy[Accessed 21 May 2012]

[13] Borka L 1975 *Anal. Chem.* **47** 1212

[14] Introduction to Interpretation of Infrared Spectra, [online]. Available from http:// www2.ups.edu/faculty/hanson/Spectroscopy/IR/IRInterpretation.htm [Accessed 21 May 2012]

[15] Bruker Tensor 27 FT-IR & OPUS Data Collection Program, [online]. Available from http://chem-faculty.lsu.edu/stanley/webpub/Bruker-Tensor-FTIR-instructions .pdf [Accessed 21 May 2012]

[16] Basic UV/Visible Spectrophotometry, [online]. Available from http:// www. biochrom.co.uk/download/72/ [Accessed 21 May 2012]

[17] Ultraviolet and Visible Absorption Spectroscopy, [online]. Available from http://www.files.chem.vt.edu/chem-ed/spec/uv-vis/uv-vis.html [Accessed 21 May 2012]

[18] Hubbard AT 2002 *Encyclopedia of Surface and Colloid Science* Volume 4 (New York: Marcel Dekker)

[19] Moulder F, Stickle WF, Sobol PE and Bomben KD 1995 *Handbook of X-ray Photoelectron Spectroscopy* (Japan: ULVAC-PHI, Inc. 370 Enzo, Chigasaki 253-8522)

[20] Photoelectron Spectroscopy , [online]. Available from http://www.chem.qmul.ac .uk/surfaces/scc/scat5_3.htm [Accessed 21 May 2012]

[21] Operating principles of the Concentric Hemispherical Analyzer, [online]. Available from http://bama.ua.edu/~surfspec/cha_details.htm [Accessed 21 May 2012]

[22] Introduction to Cathodoluminescence, [online]. Available from http://plaza.snu .ac.kr/~lee2602/atlas/cath_intro.html [Accessed 21 May 2012]

Chapter V

Luminescence from lanthanide doped sol-gel silica

1. Introduction

Microporous silica (SiO_2) prepared by the sol-gel technique is generally considered to be an optically inert medium, and its chemical and thermal stability increase its attractiveness as a host for luminescent ions [1,2]. Further advantages of the sol-gel process are that it can produce very pure glass at temperatures well below the melting point, and allows incorporation of much higher concentration of dopants than the melt process [3,4]. Lanthanide group ions are usually used as luminescent centres [5]. These ions have partially filled f-level electron shells, giving rise to various electron transitions in the UV, visible and IR regions of spectrum.

Luminescence emission produced by photon (photoluminescence) or electron (cathodoluminescence) excitation has different properties according to the different mechanism causing the excited state. Many studies on photoluminescence or cathodoluminescence from lanthanide doped silica have been reported [6-11], but according to our knowledge no comparison between photoluminescence and cathodoluminescence of the same samples has been reported. The luminescent properties of silica, prepared under identical conditions, but doped with a variety of different lanthanide ions, has been studied using cathodoluminescence (CL) as well as photoluminescence (PL) spectroscopy and the results using these two excitation methods were compared.

2. Experimental

For the sol-gel process tetraethylorthosilicate (TEOS) was allowed to react with water to form silica (SiO_2). Ethanol was used as a solvent, nitric acid was added to catalyze the reaction and the nitrates of lanthanide were added to produce doped samples. After stirring for five hours, mixtures were stored in closed containers and transferred to a water bath at 50°C until formation of a gel. Finally the gel was dried, ground to a fine

powder and annealed in air at 600 or 1000°C for 2 hours. The reduced samples were annealed in flowing 4% hydrogen in argon gas for the same temperatures and time.

X-ray diffraction (XRD) measurements were performed with a Bruker D8 diffractometer; Scanning electron microscopy (SEM) images and Auger spectra were obtained with a PHI 700 Scanning Auger Nanoprobe; Fourier Transform Infrared (FTIR) absorption measurements were made with a Bruker Tensor 27 instrument. Diffuse reflectance spectra were recorded using a Lambda 950 UV-Vis spectrophotometer with an integrating sphere and using spectralon as a reflectance standard. PL was measured with a Cary Eclipse Fluorescence Spectrophotometer and also with a 325 nm He-Cd laser PL system. CL measurements were made in a Preparation chamber from PREVAC equipped with an ES40C electron gun unit and USB2000+ spectrometer under the following conditions: 2 kV accelerating voltage, 400 μA emission current and vacuum ~2×10^{-8} torr.

3. Results and discussion

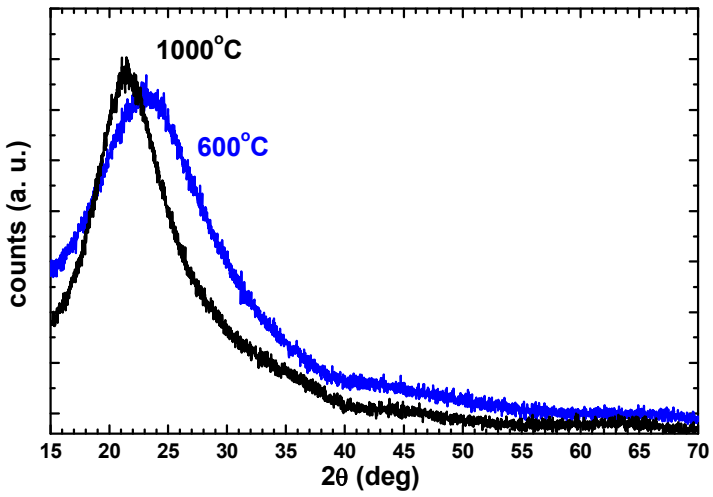

Figure 1: XRD of pure silica annealed in air at 600 and 1000°C.

The XRD spectra of sol-gel silica samples annealed at different temperatures are given in Figure 1. The sample annealed at 600°C exhibited a broad peak at $2\theta \approx 23°$, characteristic

of amorphous silica [12,13]. This narrowed slightly after annealing at 1000°C, which indicates a less disordered yet still amorphous sample. Nagpure *et al*. [14] reported a low-quartz crystalline phase in silica prepared by the combustion method annealed at 1000°C. These contrasting results indicate the advantage of the sol-gel process for producing a single amorphous phase. There were no significant changes in the XRD spectra for the samples due to doping, nor for those heated in a reducing atmosphere instead of air.

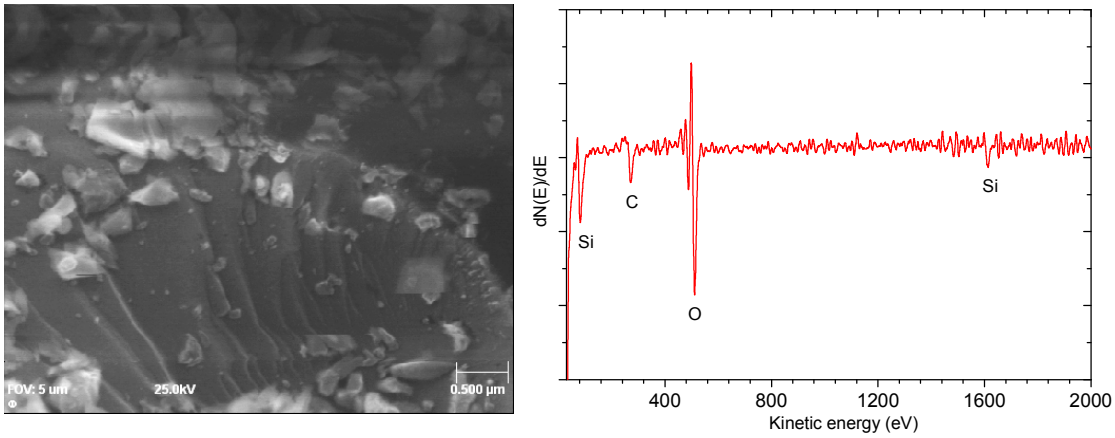

(a) (b)

Figure 2: (a) SEM image and (b) Auger spectrum of Ce doped silica

A SEM image for an undoped sample annealed at 1000°C is shown in Figure 2(a). It shows fractured surfaces and particles with irregular shape, consistent with what is expected for a brittle material that has been ground to powder. The corresponding Auger spectrum is shown in Figure 2(b). The peak at 92 eV as well as the small peak at 1615 eV correspond to Si, while the peak at 503 eV corresponds to O, making up the SiO_2. The peak at 273 is due to C contamination from adventitious hydrocarbons which are usually present. No extra peaks were found with the sample doped with 4 mol% Ce, for which the Auger spectrum looks the same as for the undoped sample. This may be due to the low level of dopant, and also because the Auger yield decreases in favour of x-ray emission for heavier elements such as the lanthanides.

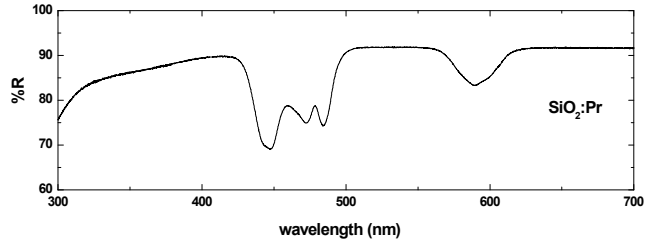

(a)

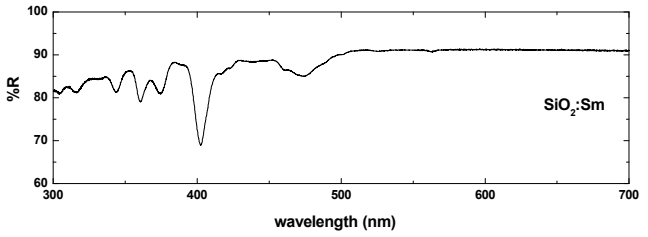

(b)

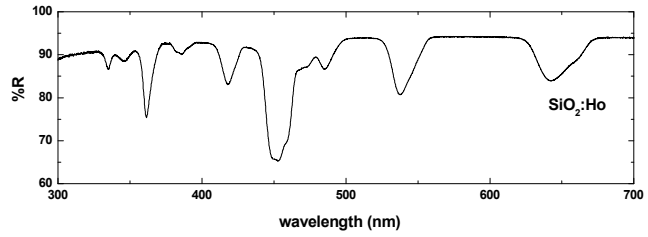

(c)

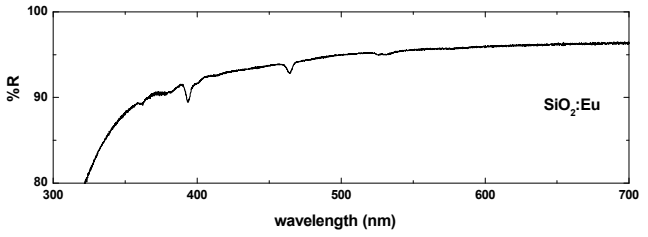

(d)

Figure 3: Diffuse reflectance spectra for SiO_2 doped with (a) Pr (b) Sm (c) Ho (d) Eu

Figure 3 shows the UV-Vis diffuse reflectance measurements for silica samples doped with a variety of lanthanide ions (concentration 1 mol%), measured with a 150 mm integrating sphere and using spectralon as a standard. The f-f absorption lines in the spectra, characteristic of these lanthanides [15], show that they have been successfully incorporated in the silica host.

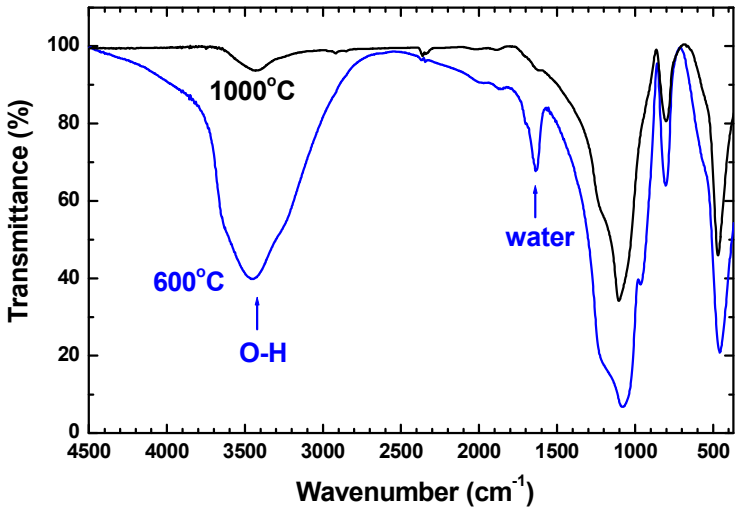

Figure 4: FTIR of Ce (0.5 mol%) doped silica samples.

FTIR spectra of silica samples annealed at 600°C and 1000°C are shown in Figure 4. As in the case of the Auger spectra, there was no difference between the doped and undoped samples. The absorption bands below 1200 cm^{-1} are characteristic of SiO_2 (see Chapter X for further details), while the absorption near 3447 cm^{-1} is attributed to the stretching vibration of hydroxyl ions (O-H) and the absorption near 1636 cm^{-1} is attributed to water molecules. The FTIR results clearly show that the lower temperature annealing (600°C for 2 h) could not effectively remove all water and hydroxyl ions present in the sol-gel process. These act as quenching sites and reduce the intensity of emission for lanthanide doped silica (see Chapter X, Figure 2 for the case of a sample doped with Tb), therefore all subsequent annealing was performed at the higher temperature of 1000°C.

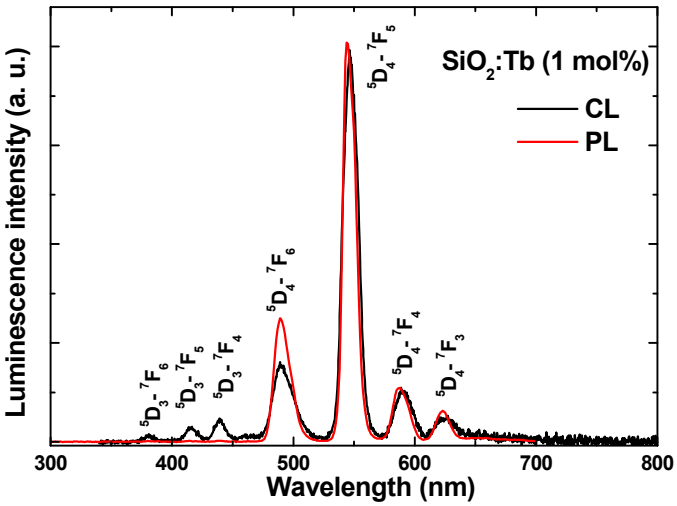

Figure 5: CL and PL of SiO_2:Tb (1 mol%)

Figure 5 shows the luminescence obtained from SiO_2:Tb(1 mol%). Strong CL and PL were obtained at 545 nm due to the $^5D_4 - ^7F_5$ transition. In addition to other weaker $^5D_4 - ^7F_J$ transitions (J= 6,5,4 and 3), CL also gave luminescence originating from the $^5D_3$ level which was not observed in the corresponding strong PL spectrum produced with 227 nm excitation. This interesting difference is discussed in more detail in Chapter VI.

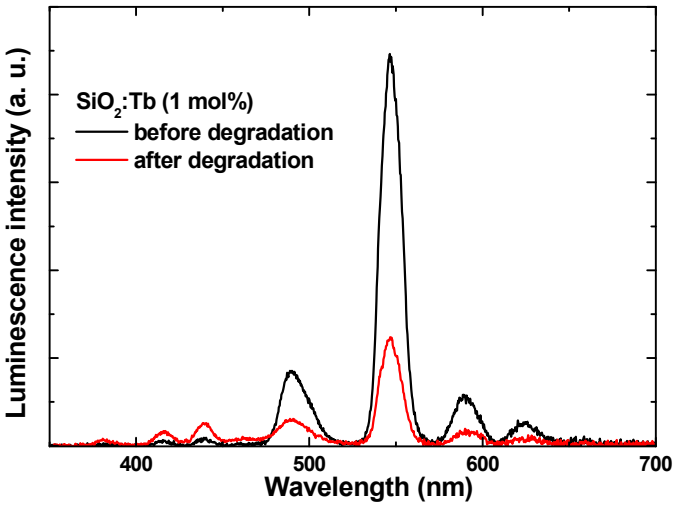

Figure 6: CL spectrum of SiO_2:Tb (1 mol%) before and after degradation.

Phosphors used for CL are known to often degrade with time, often due to electron stimulated surface chemical reactions [16]. The terbium doped silica sample was left overnight (20 h) exposed to the electron beam (2 kV accelerating voltage, 400 μA emission current and vacuum ~2×10^{-8} torr) and Figure 6 shows the CL spectra before and after degradation. The CL system used is still under development and it was not possible to measure the beam current or diameter. However, the degradation of the sample is very clear, even for the good vacuum conditions. Of great interest is that although the green emission at 545 nm from the $^5D_4$ level is decreased substantially, the blue emissions below 480 nm have actually increased. The intensity of the blue emissions from Tb is known to be dependent on the Tb doping level, because for high Tb concentrations energy transfer by cross relaxation between Tb^{3+} ions can occur which depopulates the $^5D_3$ level from which the blue emission originates [17]. (This is discussed in more detail in Chapter VI.) It is therefore suggested that when the degradation process results in a decrease in the concentration of luminescent Tb^{3+} ions, the rate of cross-relaxation is reduced, resulting in an increase in the blue luminescence emission.

For the Tb doped silica, the influence of the CL excitation voltage on the CL emission intensity was measured. The measurements were taken over a short time during which degradation is negligible. Figure 7 shows the luminescence intensity of SiO_2:Tb (normalised to the lowest value measured) as a function of the accelerating voltage of the electron beam. In general, for a given current density the CL emission increases as a power function of the accelerating voltage V, relative to a dead voltage V_0, i.e. [18]

$$L = c(V - V_0)^n$$

where c is a constant that depends on the current density and n generally lies between one and three. In this case the experimental data fits well to a line, meaning $n = 1$, and the dead voltage V_0 can be seen to be about 0.8 kV.

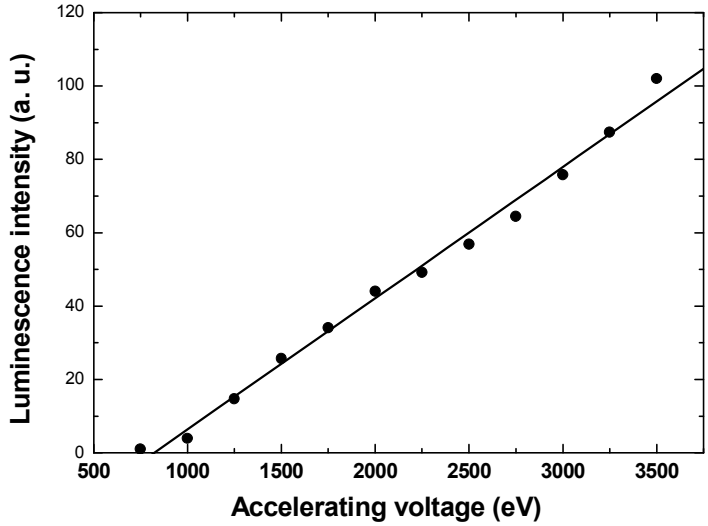

Figure 7: CL emission of SiO_2:Tb (1 mol%) vs accelerating voltage (closed circle) fitted to the straight line.

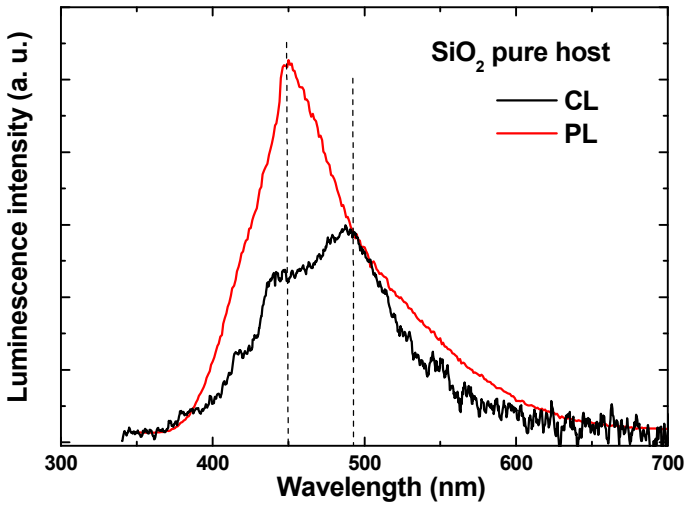

Figure 8: CL and PL of pure silica

Undoped silica exhibited weak CL emission in a band from 400–600 nm (Figure 8). Luminescence from pure amorphous silica at 2.7 eV (460 nm) is well known and associated with an oxygen deficiency defect [19]. Undoped sol-gel silica has been found to have two photoluminescence peaks in this region, a more intense peak near 450 nm and weaker peak or shoulder at 525 nm [9,20]. We observed opposite trend, namely the

peak near 450 nm is weaker that the peak near 500 nm. A considerable PL emission under laser excitation (325 nm) was detected with a band from 400–600 nm (Figure 8) having a maximum at 450 nm.

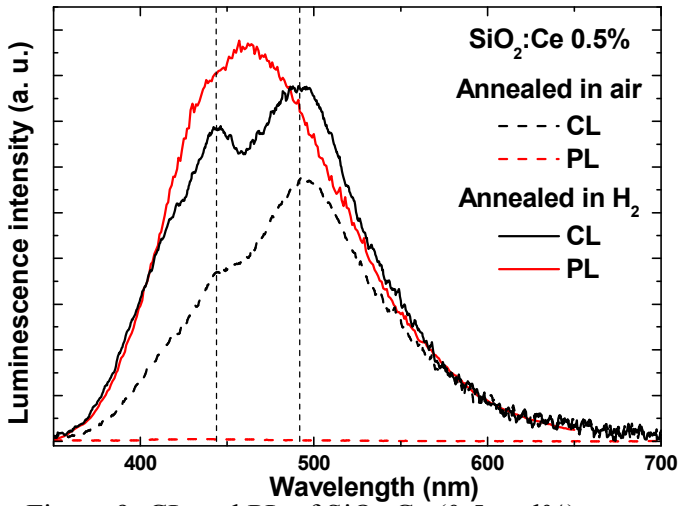

Figure 9: CL and PL of SiO_2:Ce (0.5 mol%)

Cerium doped samples (Figure 9) gave a broad band CL emission from 400 – 600 nm having two peaks at 447 nm and 495 nm. These are separated by 2170 cm^{-1}, which corresponds well to the expected splitting of f-d luminescence of Ce from the d-level to the two f-levels ($^2F_{5/2}$ and $^2F_{7/2}$), namely about 2070 cm^{-1} [21]. However, the cerium doped silica sample annealed in air gave no emission when excited by UV illumination with the Cary Eclipse fluorescence spectrometer. This interesting observation can be explained by the fact that cerium may convert from the luminescent Ce^{3+} to the non-luminescent Ce^{4+} ion during the high temperature annealing in air as used in this study. Therefore samples show no photoluminescence, although under electron irradiation the Ce^{4+} ions may capture an electron to form an excited luminescent Ce^{3+} ion [22] and therefore samples exhibit cathodoluminescence (see Chapter VIII for further details). After annealing our cerium doped samples in a reducing atmosphere as in ref. [23] they did indeed exhibit fluorescence under 325 nm excitation, as shown in Figure 5, with broad peak having a single maximum at 461 nm.

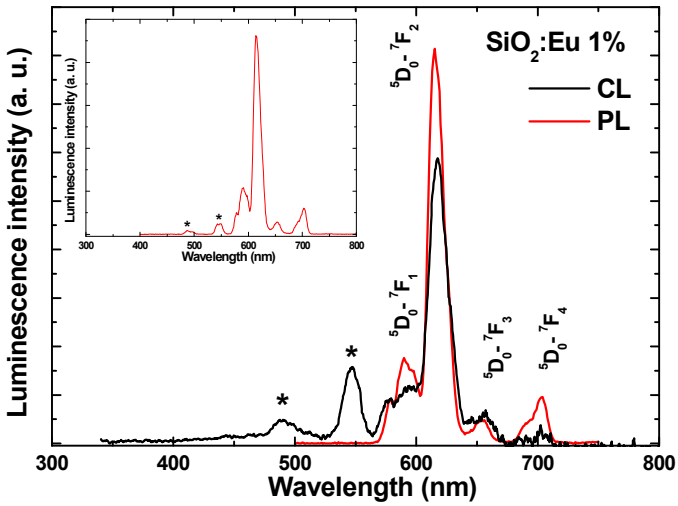

Figure 10: CL and PL (λ_{ex} = 395 nm) of SiO_2:Eu (1 mol%). The inset is the PL emission at λ_{ex} = 227 nm

Samples doped with europium (Figure 10) exhibited a good photoluminescence spectrum under 395 nm excitation, characteristic of the Eu^{3+} ion. It is dominated by the electric dipole $^5D_0$–$^7F_2$ transition near 615 nm, which indicates that there is lack of inversion symmetry at the site of the ion [24]. The corresponding CL spectrum was similar to the PL, except for two additional weak emission peaks located at 490 nm and 545 nm. These wavelengths both occur in the Tb emission spectrum (Figure 5) suggesting that they are due to a small impurities of Tb ions. This is confirmed by the fact that when the PL is measured by exciting the sample at 227 nm (a common excitation for both Eu and Tb), then the peaks are also observed in the PL spectrum (see the inset in Figure 10).

Samples doped with samarium (Sm^{3+}) emitted red light near 650 nm due to the $^4G_{5/2}$-$^6H_{9/2}$ transition of the Sm^{3+} ion (Figure 11). The PL and CL spectra are almost identical. The same is true for samples doped with Dy^{3+} which has orange luminescence near 577 nm ascribed to the $^4F_{9/2}$-$^6H_{13/2}$ transition of the Dy^{3+} ion (Figure 12).

Praseodymium (Pr^{3+}) doped SiO_2 displayed no luminescence when annealed in air. Very poor CL and PL emission was observed near 615 nm for samples reduced in hydrogen (Figure 13), while the thullium (Tm^{3+}) doped SiO_2 sample showed only CL emission near 463 nm (Figure 14). Neither CL nor PL emission were observed from the samples doped with Nd, Gd, Ho, Er and Yb lanthanide ions during the study, so no results can be given.

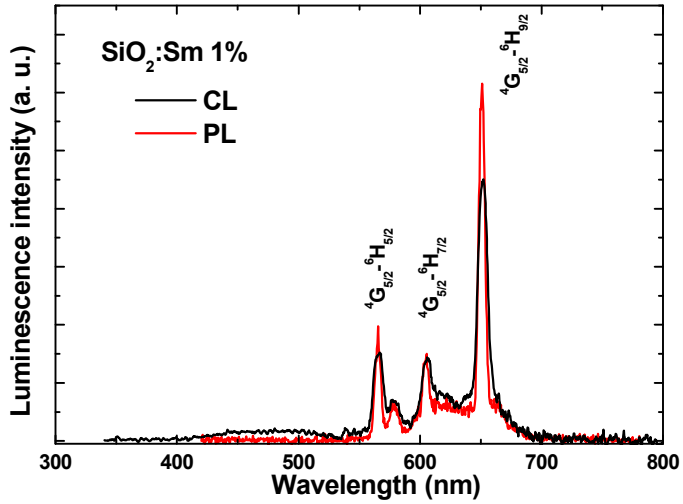

Figure 11: CL and PL (λ_{ex} = 400 nm) of SiO_2:Sm (1 mol%)

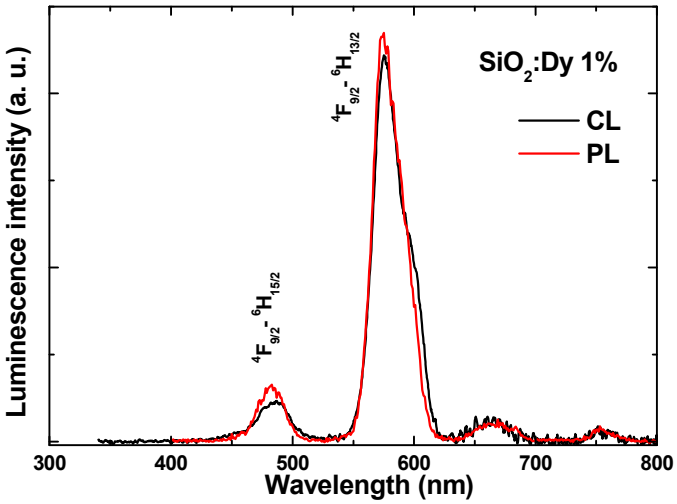

Figure 12: CL and PL (λ_{ex} = 350 nm) of SiO_2:Dy (1 mol%)

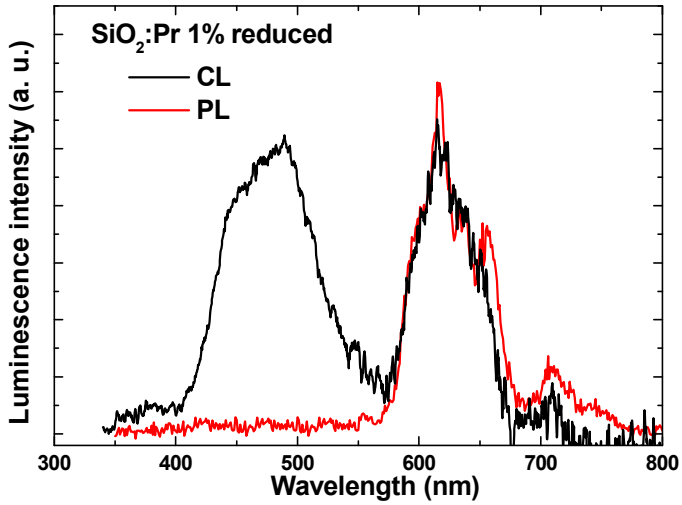

Figure 13: CL and PL (λ_{ex} = 252 nm) of SiO_2:Pr (1 mol%) reduced in hydrogen. The CL peak at 460 nm originates from the host (compare Figure 8).

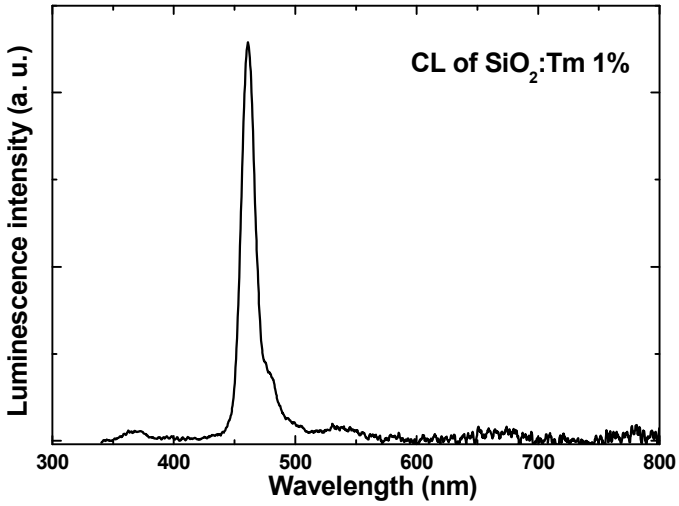

Figure 14: CL of SiO_2:Tm (1 mol%)

4. Conclusions

The photoluminescence and cathodoluminescence spectra of a wide variety of lanthanide dopants in sol-gel amorphous silica have been recorded for identical preparation and measurement conditions. While the sample doped with Tm^{3+} only exhibited CL, samples doped with Tb, Ce, Eu, Sm, Dy and Pr were found to emit under both forms of excitation, although for Tb, Ce and Pr there are significant differences in the spectra depending on the mode of excitation. Certainly in the case of Tb and Ce doping, the cathodoluminescence excitation produced luminescence which was not created by UV irradiation, and this was attributed to the additional luminescence of ions in the 4+ valence state that captured electrons and then emitted in a similar fashion as ions in the 3+ state. For cerium doped samples photoluminescence emission could also be induced by annealing the samples in a reducing atmosphere. These results indicate some of the challenges when comparing photoluminescence and cathodoluminescence results, as well as giving a survey of the suitability of sol-gel silica as a host for luminescent lanthanide ions.

References

[1] Yehoshua Y 2006 *The physics and engineering of solid state lasers* (Washington: International society for optical engineering)

[2] Guodong Q, Minquan W, Mang W, Xianping F and Zhanglian H 1997 *J. Lumin.* **75** 63

[3] Jan T, Johannes Z and Rolf C 2006 *J. Mater. Sci.* **41** 8173

[4] Silversmith AJ, Boye DM, Brewer KS, Gillespie CE, Lu Y and Campbell DL 2006 J. *Lumin.* **121** 14

[5] Claire P, Anders H and Mikael L 2005 *J. Lumin.* **111** 265

[6] Muralidharan MN, Rasmitha CA and Ratheesh R 2009 *J Porous Mater* **16** 635

[7] Yan B, Zhang H-j, Wang S-b and Ni J-z 1998 *J. Photochem. Photobio. A: Chemistry I* **12** 231

[8] Ntwaeaborwa OM, Swart HC, Kroon RE, Holloway PH and Botha RJ 2006 *Surf. Interface Anal.* **38** 458

[9] Biggs MM, Ntwaeaborwa OM, Terblans JJ and Swart H, 2009 *Physica B* **404** 4470

[10] Mhlongo GH, Ntwaeaborwa OM, Dhlamini MS, Swart HC and Hillie KT 2010 *J. Mater. Sci.* **45** 5228

[11] Dhlamini MS, Mhlongo GH and Hillie KT 2010 *Opt. Mater.* **33** 79

[12] Lijuan W, Anhuai L, Changqiu W, Xishen Z, Dongjun Z and Rui L 2006 *J. Colloid Interface Sci.* **295** 436

[13] Kalapathy U, Proctor A and Shultz J 2000 *Bioresour Technol.* **73** 257

[14] Nagpure IM, Pitale SS, Tshabalala KG, Kumar V, Ntwaeaborwa OM, Terblans JJ and Swart HC 2011 *Mater. Res. Bull.* **46** 2359

[15] Carnall WT 1979 Ch. 24 in "Handbook on the Physics and Chemistry of Rare Earths" (Eds K.A. Gschneidner, Jr. and L. Eyring) North-Holland Publishing Company

[16] Swart HC, Terblans JJ, Coetsee E, Ntwaeaborwa OM, Dhlamini MS, Nieuwoudt S and Holloway PH 2007 J. Vac. Sci. Technol. A 25 917

[17] Blasse G 1983 *Rev. Inorg. Chem.* **15** 319

[18] Garlick GFJ 1949 *Luminescent materials* (London: Oxford University Press) p.176

[19] Sakurai Y and Nagasawa K 2001 *J. Non-cryst. solids* **290** 189

[20] Ntwaeaborwa OM, Swart HC, Kroon RE, Botha JR, Ngaruiya JM and Holloway PH 2008 *in: H.K. Wright, G.V. Edwards (Eds.)* Photoluminescence research progress (New York: Nova Science Publishers)

[21] Andriessen J, Antonyak OT, Dorenbos P, Rodnyi PA, Stryganyuk GB, van Eijk CWE and Voloshinovskii AS 2000 *Optics Comm*. **178** 355

[22] Reisfeld R, Patra A, Panczer G and Gaft M 1999 *Opt. Mater.* **13** 81

[23] Fasoli M, Vedda A, Lauria A, Moretti F, Rizzelli E, Chiodini N, Meinardi F and Nikl M 2009 *J. Non-Cryst. Solids* **355** 1140

[24] Yen WM, S Shionoya S and H Yamamoto H 1999 *Phosphor Handbook* 2nd ed. (Boca Raton: CRC Press)

Chapter VI

$^5D_3 \rightarrow {}^7F_J$ emission of Tb doped sol-gel silica

1. Introduction

Sol-gel silica (SiO_2) has been widely used as a host material for rare earth ions because it has good physical properties and chemical stability [1]. The sol-gel method is an attractive technique for SiO_2 preparation since it can produce very pure glass at temperatures well below the melting point and allows incorporation of much higher concentration of dopants than the melt process. Trivalent terbium is a rare earth ion widely used as a dopant in a variety of host matrices [2]. The ion exhibits narrow line emissions located between 400 and 650 nm. The blue light below 480 nm can be attributed to the $^5D_3 \rightarrow {}^7F_J$ transitions, while the green emission above 480 nm results from the $^5D_4 \rightarrow {}^7F_J$ transitions [3]. Figure 1(a) shows a partial energy level diagram of trivalent terbium with labeled transitions that correspond to the observed emission lines. The intensity of blue fluorescence from the $^5D_3$ level is highly dependent on the terbium concentration [3-5]. Since the energy difference between $^5D_3$ and $^5D_4$ levels is approximately equal to the energy difference between $^7F_0$ and $^7F_6$ levels, the excited electrons in the $^5D_3$ level populate the $^5D_4$ level through cross-relaxation, which involves a transfer of energy from an ion in the $^5D_3$ state to a nearby ion in the ground state (see Figure 1(b)) and can be represented as [6]

$$Tb^{3+}(^5D_3) + Tb^{3+}(^7F_6) \rightarrow Tb^{3+}(^5D_4) + Tb^{3+}(^7F_0).$$

Thus, in samples of low Tb^{3+} concentration where cross-relaxation is improbable both blue $^5D_3 \rightarrow {}^7F_J$ and green $^5D_4 \rightarrow {}^7F_J$ emissions are observed, while the blue $^5D_3 \rightarrow {}^7F_J$ emission is generally not observed in samples containing higher Tb^{3+} concentrations. This concentration quenching effect is well known and blue emission can be expected only if the cross-relaxation is inhibited e.g. by decreasing the Tb concentration or increasing the average distance between terbium ions by co-doping with Al, as reported by Silversmith *et al.* [4]. In this chapter we present different emission spectra obtained for highly doped (1 mol%) silica samples during photoluminescence and

cathodoluminescence characterization. What is surprising is that the blue emission, which does not occur during photoluminescence measurements, is observed during cathodoluminescence measurements. Possible reasons for this were evaluated.

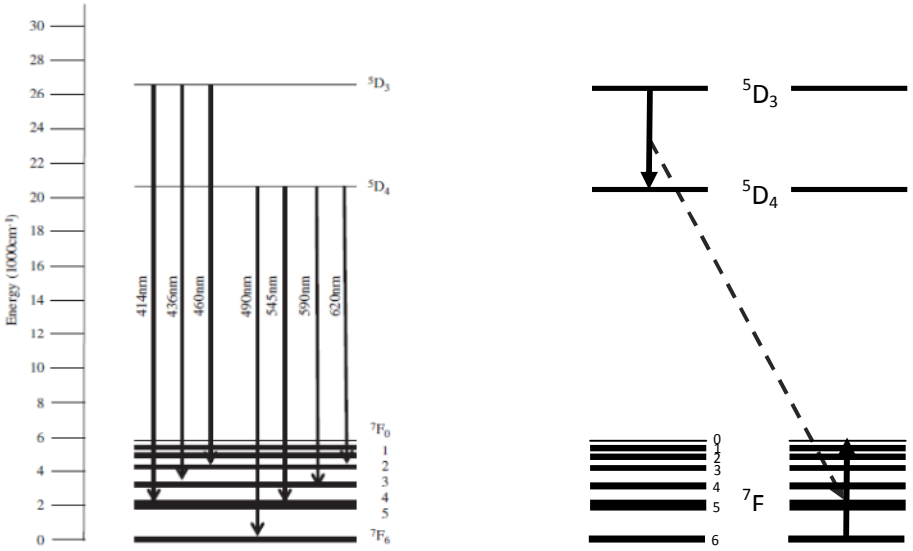

Figure 1: (a) Energy level diagram of Tb^{3+} [4]. (b) Cross-relaxation between adjacent Tb^{3+} ions.

2. Experimental

Samples of 0.1 and 1 mol% Tb-doped SiO_2 glass were prepared by the sol–gel method using tetraethylorthosilicate (TEOS), water, ethanol (C_2H_5OH) and $Tb(NO_3)_3$ as starting materials and nitric acid (HNO_3) as a catalyst. The molar ratio of TEOS:H_2O:C_2H_5OH was 1:5:10, and the HNO_3 concentration was 0.015 M in water. TEOS was mixed with ethanol and stirred for 30 min after which the acidified water was added and stirring continued for another 30 min. After that $Tb(NO_3)_3$ was dissolved in a little ethanol and added to the mixture, which was stirred for a further 4 h. Then the mixture was stored in a closed container and transferred to a water bath at 50°C until a gel was formed. The gel was dried and annealed in air at 1000°C for 2 h. X-ray diffraction (XRD) measurements were performed with a Bruker D8 diffractometer while photoluminescence was measured at room temperature with a variety of excitation sources including a xenon lamp, Cary Eclipse Fluorescence Spectrophotometer, a 248.6 nm Ne-Cu laser mini-PL system, a 325 nm He-Cd laser PL system as well as synchrotron radiation using the SUPERLUMI

beam-line at HASYLAB. Cathodoluminescence was measured in a PHI Model 549 Auger system with S2000 spectrometer at a pressure of ~2 x 10^{-8} torr, an accelerating voltage of 2 kV and a beam current of ~12 μA.

3. Results and discussion

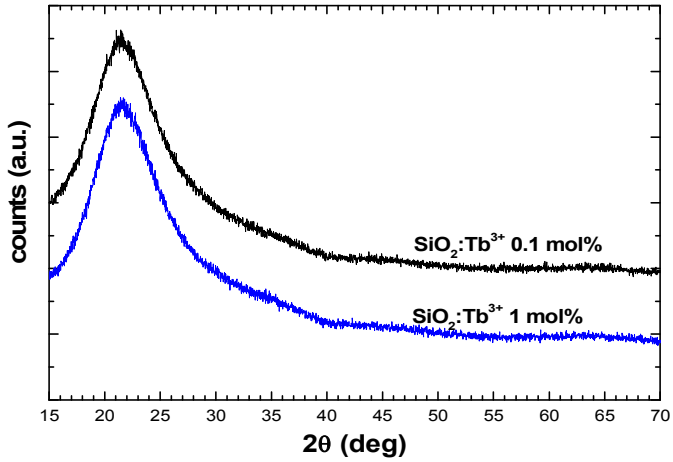

Figure 2: XRD of Tb^{3+} 1% and 0.1% doped silica annealed in air at 1000°C.

The XRD spectra (Figure 2) exhibited the well known characteristics broad peaks of amorphous silica (SiO_2) at $2\theta \approx 23°$[7,8] and no differences between samples with low and high Tb concentrations were found. The PL spectra of SiO_2:Tb^{3+} (1 mol%) recorded using the xenon lamp, lasers and synchrotron radiation showed the characteristic green emission bands attributed to the $^5D_4 \rightarrow {}^7F_J$ transitions (J = 6, 5, 4, 3) with the dominant green band at 545 nm (Figure 3), but no blue emission band from $^5D_3 \rightarrow {}^7F_J$ transitions were observed, except for very small peaks in the spectrum excited with the 248 nm laser. However, in the same sample the CL spectrum showed the blue emission from $^5D_3 \rightarrow {}^7F_J$ transitions (J = 5, 4) in addition to the $^5D_4 \rightarrow {}^7F_J$ green emission bands. Figure 4 shows that for the lower concentration Tb^{3+} (0.1 mol%) the blue $^5D_3 \rightarrow {}^7F_J$ emissions was observed from the PL spectra. The absence of the $^5D_3 \rightarrow {}^7F_J$ blue emission in the PL results at high Tb^{3+} concentration (1 mol%) (Figure 3) can be attributed to the cross-relaxation process (concentration quenching). It is however interesting to find out why the blue $^5D_3 \rightarrow {}^7F_J$ emission is present in the CL spectra of the sample with a high concentration (1 mol%) of Tb^{3+}.

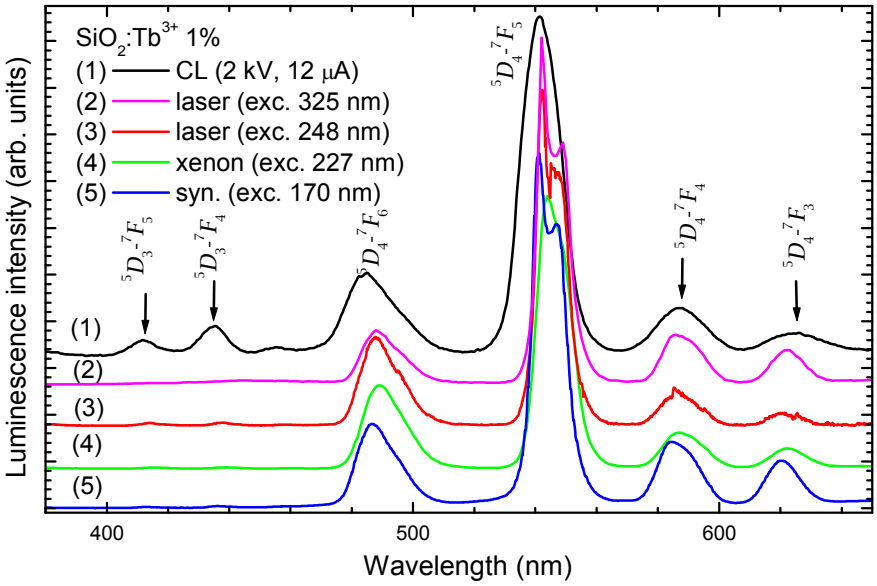

Figure 3: CL and PL spectra of SiO_2 :Tb^{3+} 1%.

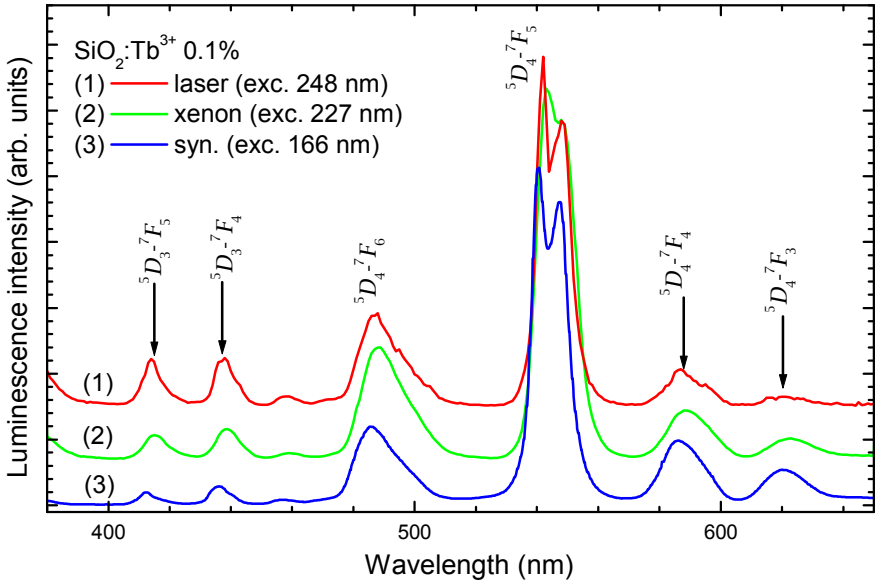

Figure 4: PL spectra of SiO_2:Tb^{3+} 0.1% .

Similar observations of blue emission in CL spectra have been reported in 1% Tb^{3+} doped Lu_2O_3 [9] and 1.5% Tb^{3+} doped Al_2O_3– ZrO_2 [10]. Zych *et al.* [9] could not explain their observation, while Zawadzki *et al.* [10] considered that the terbium ions may be found both in Tb^{4+} and Tb^{3+} oxidation states, suggesting that some Tb^{4+} ions substituting Zr^{4+} ions may be converted into excited $(Tb^{3+})^*$ ions as a result of the electron beam excitation. They propose that the normally non-luminescent Tb^{4+} ions, which became the transient $(Tb^{3+})^*$ ions under electron beam excitation, are responsible for the blue emission according to

$$Tb^{4+} + e^- \rightarrow (Tb^{3+})^* \rightarrow Tb^{4+} + h\nu_{lum}(^5D_3 \rightarrow {}^7F_J) + e^- .$$

A different environment of Tb^{4+} ions compared to Tb^{3+} ions, with a lower concentration, may account for the lack of concentration quenching. This mechanism is associated with the electron beam excitation and therefore explains why the blue emission is found in the CL spectrum but not in the PL spectra (Figure 3). In our case a similar mechanism may account for the blue terbium luminescence observed in 1% doped samples using CL, where Tb^{4+} ions substitute Si^{4+} ions in the silica.

As an alternative explanation we considered that the quantum efficiency of CL is given as approximately 10^3 times the quantum efficiency of PL [11]. This suggested the possibility that for CL the rate of excitation is higher and both the $^5D_3$ and $^5D_4$ Tb^{3+} levels could be appreciably populated. Then the high population of electrons in the lower $^5D_4$ levels may actually prevent the cross-relaxation process in some ions (due to the exclusion principle) and therefore relaxation directly from the $^5D_3$ level would occur, i.e. blue $^5D_3 \rightarrow {}^7F_J$ emission would be observed. For 2 keV electrons, if the bandgap of the SiO_2 host is taken as 9 eV [12] each electron is capable of creating ~220 electron hole pairs. This is lower than the estimate of 10^3 for the CL to PL relative quantum efficiency given earlier, because in this case the electron energy is fairly low and the bandgap is quite large. A current of 12 μA corresponds to 7.5×10^{13} electrons per second, giving an excitation rate of 1.7×10^{16} electron-hole pairs per second. The power of all the light sources used to obtain the PL results in Figure 3 has not been well characterized, except the 325 nm He-Cd laser for which the power onto the sample was measured to be 5 mW. For this wavelength the photon energy is 3.8 eV or 6.1×10^{-19} J and so the photon flux is

8.2×10^{15} photons per second. If each photon has the same probability of producing a luminescent photon as an electron-hole pair (which is unlikely to be the case, and introduces some uncertainty in the rough calculation), then the ratio of excited states produced by CL compared to PL is only about 2:1. This suggests that the $^5D_3 \rightarrow {}^7F_J$ blue emission presented in the CL spectra of the sample with 1% Tb^{3+} concentration cannot be attributed to the high quantum efficiency of CL compared to PL, as the excitation rates are similar in the two processes. The calculation rather supports the view that it is the difference in the nature of the excitation source between CL and PL that is mainly responsible for the difference in emission from the same sample, and that the mechanism proposed by Zawadzki *et al.* [10] can be used to explain this phenomenon.

4. Conclusion

Tb^{3+} ions were successfully incorporated into silica produced by the sol-gel process. Concentration quenching became significant, removing the blue emission below 480 nm in the PL results, when the Tb^{3+} concentration was increased from 0.1 to 1 mol%. Yet the blue emission was observed in the CL results even at the higher concentration of Tb^{3+}. We conclude that is not as a result of the difference in excitation rates between CL and PL (or the high quantum efficiency of CL compared to PL), but rather due to the difference in the nature of excitation. During CL excitation it is possible for electrons to reduce non-luminescent Tb^{4+} ions into an excited $(Tb^{3+})^*$ state, and it appears that this source of luminescence is not concentration quenched, possibly because it has a lower concentration on a different site of the Tb^{4+} ions compared to the Tb^{3+} ions. It is clear that whether the blue $^5D_3 \rightarrow {}^7F_J$ emission of terbium doped silica occurs or not depends not only on the terbium concentration, but also on the nature of the excitation source.

References

[1] Guodong Q, Minquan W, Mang W, Xianping F and Zhanglian H 1997 *J. of Lumin.* **75** 63

[2] Dhlamini MS, Ntwaeaborwa OM, Swart HC, Ngaruiya JM and Hillie KT 2009 *Physica B* **404** 4406

[3] Shionoya S and Yen WM (Eds.) 1999 *Phosphor Handbook* (Boca Raton: CRC Press)

[4] Silversmith AJ, Boye DM, Brewer KS, Gillespie CE, Lu Y and Campbell DL 2006 *J. Lumin.* **121** 14

[5] Hayakawa T, Kamata N and Yamada K 1996 *J Lumin.* **68** 179

[6] Blasse G 1983 *Rev. Inorg. Chem.* **15** 319

[7] Lijuan W, Anhuai L, Changqiu W, Xishen Z, Dongjun Z and Rui L 2006 *J Colloid Interface Sci.* **295** 436

[8] Kalapathy U, Proctor A and Shultz J 2000 *Bioresour Technol.* **73** 257

[9] Zych E, Hreniak D, Strek W 2002 *Radiat. Eff. Defects S.* **157** 983

[10] Zawadzki M, Hreniak D, Wrzyszcz J, Miśta W, Grabowska H, Malta OL and Stręk W 2003 *Chem. Phys.* **291** 275

[11] Ozawa L 2007 *Cathodoluminescence and Photoluminescence Theories and Practical Applications* (Boca Raton: CRC Press)

[12] Sze SM 1981 *Physics of Semiconductor Devices* (New York: Wiley)

Chapter VII

The impurity levels of lanthanide ions in silica

1. Introduction

Silica is a basic material of technological importance for optics, microelectronics, photonics and fibre optics. Its high absorption edge energy makes it particularly useful for UV applications and it has been used as a host material for a variety of luminescent lanthanide ions due to its chemical stability and non-hygroscopic nature. Specific applications include optical amplifiers doped with erbium for the telecommunications industry [1] and x-ray scintillation material doped with cerium for radiation sensing [2].

For lanthanide ions the 4f electron energy levels are shielded from the host environment by the filled outer 5s and 5p orbitals, so that the transitions between the 4f states (and therefore the luminescence wavelengths) are relatively insensitive to the host. For this reason little attention has been paid until recently to the location of the impurity levels of the lanthanide ions within the energy gaps of their hosts. However, luminescence from some lanthanide ions, e.g. cerium, occurs due to f-d transitions from the unshielded 5d state of which the energy relative to the f-states is therefore host dependent. The absolute positions of the 4f and 5d states relative to the energy gap of the host also affect quenching and charge trapping phenomena and so they are required for proper modelling of phosphor performance [3]. In addition, the interaction of lanthanide ions with defect levels of a host can only be studied if the energy levels of the lanthanide ions are known.

Although the use of lanthanides in luminescence phosphors became widespread about half a century ago [4], it is only recently that a phenomenological model capable of predicting the lanthanide energy levels has become available. This is primarily due to the work of Dorenbos and was applied initially to CaF_2 and YPO_4 [5] and more recently to other materials e.g. GaN [6] and $Al_xGa_{1-x}N$ [7] where it was possible to explain the lack of blue luminescence from terbium ions unless $x > 0.38$ due to overlap of the 4f $^5D_3$ level

with the conduction band. Only five host-specific parameters are required: the bandgap of the host and four others, two each for divalent and trivalent ions to locate the ground states of the f and the d levels respectively. In principle the data can be obtained from any of the lanthanide ions, since the data compiled by Dorenbos [8-14] relates to the values between the different lanthanide ions. In practice Eu^{2+} is usually used for the divalent ions and Ce^{3+} for the trivalent ions, as this data is most readily obtained experimentally. Determining the parameters to locate the levels for a particular host is not always straightforward. In this chapter a scheme for the energy levels of both the divalent and trivalent lanthanide ions in amorphous silica is proposed.

2. Model for the lanthanide impurity levels

As a first step to the model, Dorenbos [8] used experimental data to show that the differences between the f-d transition energies of trivalent lanthanide ions were independent of the host. This allowed new estimates of the free ion f-d transition energies and, using at least one experimental f-d transition energy for any trivalent lanthanide ion in a host, to give the crystal field depression $D(A,3+)$ for that host A [9]. The process was analogous for the divalent ions [10], yielding the crystal field depressions $D(A,2+)$ for divalent ions in different hosts [11].

Given the f-d transition energies E_{fd}, if one can determine either the energy from the valence band to the f-level E_{Vf} or from the d-level to the conduction band E_{dC} one can place the levels absolutely. Note that

$$E_{Vf} + E_{fd} + E_{dC} = E_{VC}$$

where E_{VC} is the bandgap. To first approximation, an electron promoted to the 5d level of any lanthanide ion interacts with the crystal in the same manner, since the differences between the lanthanides occurs only for the inner shielded 4f electrons. Therefore the 5d energy levels of all the lanthanides are approximately equal [5]. In addition Dorenbos found that the charge transfer (CT) energy (E^{CT}) of a trivalent lanthanide ion provides a fair measure of E_{Vf} for the corresponding divalent ion [12]. By comparing small

calculated changes in E_{dC} across the divalent lanthanides [13] with changes in E_{Vf} based on CT data, and using the known relative f-d transition energies together with

$$\Delta E_{Vf} + \Delta E_{fd} + \Delta E_{dC} = 0,$$

Dorenbos [12] was able to find the variation ΔE_{Vf} across the divalent lanthanides. Then if either the f- or the d-energy level of any divalent lanthanide ion can be found relative to either the valence or the conduction band, all the f- and d-levels for all the divalent ions can be computed. The value of E^{CT} for Eu^{3+}, giving E_{Vf} (Eu^{2+}), is often most easily obtained experimentally [14] and so ΔE_{Vf} is generally expressed relative to this ion. Dorenbos [12] also predicted the variation ΔE_{Vf} across the trivalent lanthanides. Although E^{CT} for tetravalent lanthanide ions is expected to be a fair measure of E_{Vf} for the corresponding trivalent lanthanide ions, this data is not so readily available and so instead E_{dC} (Ce^{3+}) is usually estimated and for the trivalent ions ΔE_{Vf} is generally expressed relative to cerium.

Therefore in addition to the bandgap of a particular host, one needs the crystal field depression of the f-d transitions and any one known absolute energy level to predict all the f- and d-levels of all the lanthanide ions. The last two parameters are needed for both divalent and trivalent ions, giving five host specific parameters in total. The free ion f-d transition energies and their relative values, together with the values of ΔE_{Vf} and ΔE_{fd} are given in Table 1. Note that recently Dorenbos [15] has published new estimates of ΔE_{Vf} for the divalent and trivalent ion which are used here. Older values have been applied successfully to oxide and fluoride hosts [14], but for a sulphide host the model did not work well and for that work the values were adapted to give a constant value for E_{dC} [16].

Table 1: Host independent data for energy level diagrams of lanthanide ions. The columns labelled Free give the f-d transition energy of the free ions. The next columns gives the relative values of the f-d energy, the energy from the valence band to the f-level ground state and the energy from the d-level ground state to the conduction band [8-15]. All values are in electron-volts.

Ion	**Divalent ions, Ln^{2+} (changes relative to Eu^{2+})**				**Trivalent ions, Ln^{3+} (changes relative to Ce^{3+})**			
	Free	ΔE_{fd}	ΔE_{Vf}	ΔE_{dC}	Free	ΔE_{fd}	ΔE_{Vf}	ΔE_{dC}
La	-0.94	-5.16	5.69	-0.53	-	-	-	-
Ce	0.35	-3.87	4.07	-0.20	6.12	**0.00**	**0.00**	**0.00**
Pr	1.56	-2.66	2.83	-0.17	7.64	1.52	-1.94	0.42
Nd	1.93	-2.29	2.50	-0.21	8.94	2.82	-3.29	0.47
Pm	1.96	-2.26	2.32	-0.06	9.31	3.19	-3.63	0.44
Sm	3.00	-1.22	1.24	-0.02	9.40	3.28	-3.74	0.46
Eu	4.22	**0.00**	**0.00**	**0.00**	10.58	4.46	-4.92	0.46
Gd	-0.10	-4.32	4.67	-0.35	11.81	5.69	-6.17	0.48
Tb	1.19	-3.03	3.23	-0.20	6.97	0.85	-0.88	0.03
Dy	2.12	-2.10	2.30	-0.20	8.58	2.46	-2.53	0.07
Ho	2.25	-1.97	2.44	-0.47	9.72	3.60	-3.55	-0.05
Er	2.12	-2.10	2.62	-0.52	9.46	3.34	-3.41	0.07
Tm	2.95	-1.27	1.77	-0.50	9.46	3.34	-3.18	-0.16
Yb	4.22	0.00	0.49	-0.49	10.83	4.71	-4.15	-0.56
Lu	-	-	-	-	12.22	6.10	-5.64	-0.46

3. Lanthanide impurity levels in amorphous silica

Amorphous silica samples doped with lanthanide ions were prepared with the sol-gel process using TEOS as a precursor and annealed at 1000°C. Emission and excitation measurement were performed on a Cary Eclipse fluorescence spectrophotometer having a xenon lamp as well as with synchrotron radiation using the SUPERLUMI station of HASYLAB at DESY. All measurements were made at room temperature, and excitation spectra from SUPERLUMI were corrected for the incident flux by comparison to the excitation spectrum of sodium salicylate.

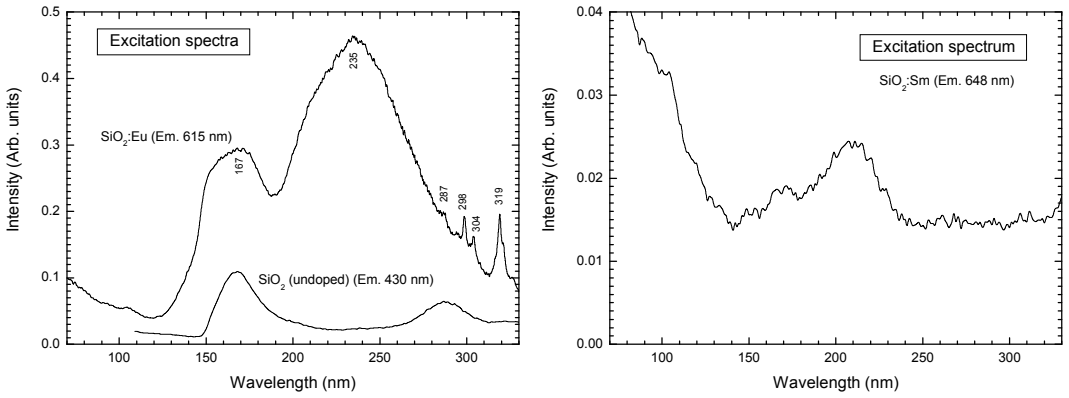

(a) (b)

Figure 1: Excitation spectra for sol-gel silica measured at SUPERLUMI. (a) undoped and 1% Eu^{3+} doped silica (b) 1% Sm^{3+} doped silica. Samples were annealed at 1000°C in air

Figure 1(a) shows the excitation spectrum of a sample doped with 1% Eu while monitoring the emission due to Eu^{3+} ions at 615 nm. The small sharp features around 300 nm are due to f-f transitions of Eu^{3+} [17], while the broad band at 235 nm (5.28 eV) is the CT band. A similar excitation spectrum was obtained by Yi *et al.* [18], but they only measured down to 250 nm. The band near 170 nm was also observed in undoped silica as well as when doping with different lanthanides and is attributed to defects in the silica [19]. The value of E^{CT} (Eu^{3+}) is used for the energy E_{Vf} (Eu^{2+}) and from the differences in Table 1, the absolute f-levels of the divalent lanthanide ions are established as in Figure 2(a). The value found here agrees well with that for silicates listed by Dorenbos [14]. From Figure 2(a) one may predict that E^{CT} (Sm^{3+}) will lie 1.24 eV above that of Eu^{3+} at 6.51 eV (190 nm). Gutsov *et al.* [20] attributed a broad absorption peak in Sm doped sol-gel silica at 35714 cm^{-1} (4.42 eV, 280 nm) to E^{CT} (Sm^{3+}). However, this energy lies lower than that for Eu^{3+} and is not consistent with our results. Figure 1(b) shows the excitation spectrum of SiO_2:1% Sm^{3+} and the CT band is found at 210 nm, fairly close to the 190 nm predicted from the model. An excitation band near 280 nm, similar to that found by Gutsov *et al.* [20], is also found for undoped silica (Figure 1(a)) and may be associated with defects [19].

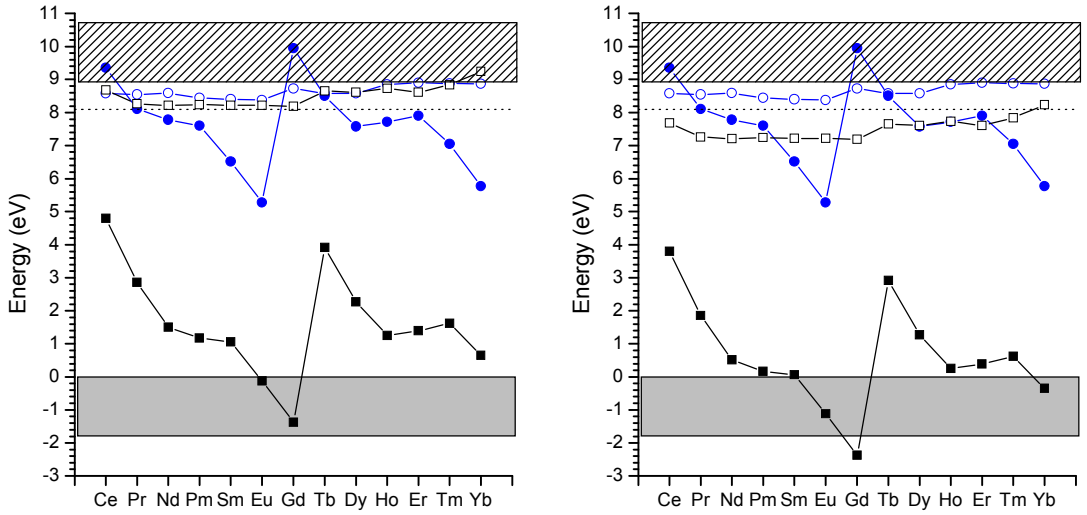

Figure 2: Location of the energy levels of divalent and trivalent lanthanide ions in silica. (a) Scheme based on associating E^{CT} (Ce^{4+}) with the value E_{Vf} (Ce^{3+}). (b) More realistic scheme obtained by reducing E_{Vf} (Ce^{3+}) in (a) by 1 eV.

To obtain the divalent lanthanide d-levels, the crystal field depression $D(A,2+)$ is required, but this value is not given for silica in the extensive tabulations of Dorenbos [11]. Hu *et al.* [21] give an excitation spectrum for Eu^{2+} f-d luminescence near 450 nm from sol-gel silica. Since the lowest d-level overlaps with higher levels the excitation peak value should not be used, but rather the 15-20% onset value on the long wavelength side [11], which is about 400 nm (3.1 eV). Comparing this to the free ion value of 4.22 eV gives $D(A,2+)$ = 1.12 eV, from which all the f-d transition energies and hence the d-levels can be calculated, as shown in Figure 2(a).

Although Ce^{4+} is non-luminescent, absorption experiments can be used to determine its CT band, and a value of about 260 nm (4.8 eV) has been reported [22,23]. If E^{CT} (Ce^{4+}) is interpreted as E_{Vf} (Ce^{3+}) then the absolute f-levels of the trivalent lanthanide ions can be determined. However, there are some indications that this is not the case. Firstly, let us consider the d-levels of the trivalent ions based on this value. To do so we require $D(A,3+)$, which can be obtained by comparing an f-d transition energy in silica with that of the free ion listed in Table 1. Figure 3(a) shows the luminescence spectra of trivalent Ce^{3+} in silica. The excitation maximum occurs near 320 nm (3.88 eV), giving $D(A,3+)$ = 2.24 eV, from which the d-levels can be derived as shown in Figure 2(a). Here the d-

levels of the trivalent ions lie about equal in energy to the divalent ones, whereas they should lie slightly lower. Dorenbos [9] does tabulate a value of $D(A,3+)$ for silica, but our value is different from this results because our samples were annealed at much higher temperature to ensure that the cerium is incorporated in the silica host. To further check the value, consider the excitation spectrum of a sample doped with Tb while monitoring the emission due to Tb^{3+} ions at 545 nm (Figure 3(b)). The peak at 226 nm (5.49 eV) is the f-d absorption band, while the peak near 160 nm is due to defects as mentioned before. This f-d energy cannot, however, be compared directly to that of the free ion because the lowest f-d transition for Tb^{3+} is spin-forbidden. The experimental value corresponds to the first spin-allowed f-d transition which occurs 0.78 eV higher [8,24]; therefore the crystal field depression can be estimated as (6.97 + 0.78) – 5.49 = 2.26 eV, in excellent agreement with the value from cerium. Additionally, Dorenbos [25] has shown that the crystal field depressions for divalent and trivalent ions are related by $D(A,2+) = 0.64D(A,3+) - 0.233$, which holds reasonably well for the values obtained here. It therefore appears that the crystal field depression is accurate, so the higher than expected trivalent d-levels seem to be as a result of overestimation of E_{Vf} (Ce^{3+}). A second factor that seems to indicate this is the difference in the f-levels of trivalent and divalent Eu: generally it varies from above 7 eV in poorly polarisable compounds like the fluorides to below 6 eV in strongly polarisable compounds like bromides and sulphides, and for the metal it is 5.4 eV [15]. In the model of Figure 2(a) it is only 5.4 eV, and a realistic value is at least 1 eV higher. Decreasing E_{Vf} (Ce^{3+}) to 3.8 eV achieves this and also brings the trivalent 5d levels 1 eV below the divalent ones, creating the more realistic energy structure in Figure 2(b). Since we have no reason to doubt the accuracy of the Ce^{4+} CT absorption energy (or any of the other measurements) to the extent of the correction applied, it is concluded that the value of E_{Vf} (Ce^{3+}) cannot be associated with the Ce^{4+} CT absorption energy. Although using the CT absorption energies of tetravalent ions was suggested initially [12], to our knowledge it has not been applied before and generally a value of E_{dC} (Ce^{3+}) is estimated instead. It has been acknowledged that identifying the trivalent CT energies with the absolute energies of the divalent ions above the valence band is an assumption that can be disputed [15], and although it appears to

work well to find values of E_{Vf} (Eu^{2+}), in this work we have shown that a similar method is not as successful for determining E_{Vf} (Ce^{3+}).

To complete the energy level diagrams in Figure 2 only the bandgap of amorphous silica is required. This has been determined as 9.0 eV by photoconductivity measurements [26], with the fundamental absorption edge at 8.1 eV [27] shown by a dotted line in Figure 2.

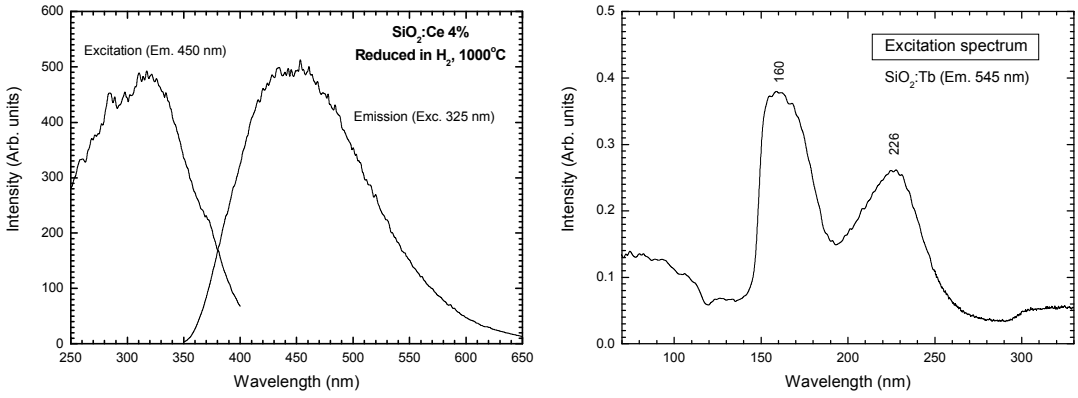

(a) (b)

Figure 3: (a) Excitation and emission spectra of 4% Ce doped silica after annealing in reducing atmosphere at 1000°C for 2 h, measured with Cary Eclipse. (b) Excitation spectrum of 0.1% Tb doped silica (annealed at 1000°C in air) measured using synchrotron radiation at SUPERLUMI.

References

[1] Tanabe S 2005 *IPAP Books* **2** 101

[2] Chiodini N, Vedda A, Fasoli M, Moretti F, Lauria A, Cantone M, Veronese I, Tosi G, Brambilla M, Cannillo B, Mones E, Brambilla G and Petrovich M 2009 *Proc. SPIE* **7136** 731614

[3] Dorenbos P 2007 Lanthanide level locations and its impact on phosphor performance. *Phosphor Handbook* 2nd ed. Ed W M Yen, S Shionoya and H Yamamoto (Boca Raton: CRC Press) p 139

[4] Dorenbos P and Bos AJJ 2008 *Rad. Meas.* **43** 139

[5] Dorenbos P 2004 *J. Lumin.* **108** 301

[6] Dorenbos P and van der Kolk E 2006 *Appl. Phys. Lett.* **89** 061122

[7] Dorenbos P and van der Kolk E 2008 *Opt. Mat.* **30** 1052

[8] Dorenbos P 2000 *J. Lumin.* **91** 91

[9] Dorenbos P 2000 *J. Lumin.* **91** 155

[10] Dorenbos P 2003 *J. Phys: Condens. Matter* **15** 575

[11] Dorenbos P 2003 *J. Lumin.* **104** 239

[12] Dorenbos P 2003 *J. Phys: Condens. Matter* **15** 8417

[13] Dorenbos P 2003 *J. Phys: Condens. Matter* **15** 2645

[14] Dorenbos P 2005 *J. Lumin.* **111** 89

[15] Dorenbos P 2009 *J. Alloys and compounds* **488** 568

[16] Bressiere A, Dorenbos P, van Eijk CWE, Yamagishi E, Hidaka C and Takizawa T 2004 *J. Electrochem. Soc.* **151(12)** H254

[17] Carnall WT 1979 The absorption and fluoresence spectra of rare earth ions in solution. *Handbook on the Physics and Chemistry of Rare Earths* vol 3 ed K A Gschneider Jr and L Eyring (Amsterdam: North Holland) p 171

[18] Yi W, Lansheng L, Huiqun Z and Ruiqin D 2006 *J. Rare Earths* **24** 199

[19] Sakurai Y and Nagasawa K 2001 *J. Non-Cryst. Solids* **290** 189

[20] Gutzov S, Ahmed G, Petkova N, Fügleinand E and Petkov I 2008 *J. Non-Cryst. Solids* **354** 3438

[21] Hu X, Fan J, Li T, Zhang D, Chen W, Bai J and Hou X 2007 *Opt. Mat.* **29** 1327

[22] Patra A, Kundu D and Ganguli D 1997 *J. Sol-Gel Sci. Techn.* **9** 65

[23] Fasoli M, Vedda A, Lauria A, Moretti A, Rizzelli E, Chiodini N, Meinardi F and Nikl M 2009 *J. Non-Cryst. Solids* **355** 1140

[24] Dorenbos P 2003 *J. Phys: Condens. Matter* **15** 6249

[25] Dorenbos P 2003 *J. Phys: Condens. Matter* **15** 4797

[26] DiStefano TD and Eastman DE 1971 *Solid State Comm.* **9** 2259

[27] Guzzi M, Martini M, Paleari A, Pio F, Vedda A and Azzoni CB 1993 *J. Phys: Condens. Matter* **5** 8105

Chapter VIII

Luminescence from Ce in sol-gel SiO_2

1. Introduction

Ce^{3+} ions have the electronic configuration of the noble gas Xe plus a single 4f electron shielded from its environment by closed 5s and 5p shells. The 5d level to which this electron can be excited is not shielded and hence depends strongly on the environment, and since this f-d transition is allowed absorption is relatively strong and the corresponding decay has a short lifetime (tens of nanoseconds). The properties of Ce^{3+} ions make them suitable for a variety of applications such as scintillators for ionizing radiation, UV absorbing filters, creation of cathodoluminescence and as a sensitizer for other emission centres in phosphors used for lighting. In addition, knowledge of the Ce^{3+} ion properties in a host serves an important fundamental role since it allows the prediction of the energy levels of other trivalent lanthanides in the same host and for this reason Dorenbos [1] compiled absorption and emission wavelengths of the Ce^{3+} f-d transition for over 300 different compounds, including silica (SiO_2). Amorphous silica has been investigated as an alternative to crystalline hosts for x-ray scintillators because of its advantageous mechanical properties (e.g. fibre drawing), its chemical stability and non-hygroscopic nature, the possibility of incorporating larger amounts of luminescent ions and the opportunity of cost reduction [2]. The sol-gel process provides an attractive low temperature alternative to the melt process for producing Ce-doped silica and several reports have been published on the properties of this material. Unfortunately, there has not been general agreement between the reported optical properties and poor luminescence has been ascribed to Ce taking the non-luminescent Ce^{4+} oxidation state or to aggregation and hence concentration quenching of Ce^{3+} ions. In this chapter studies from our laboratory using a variety of excitation sources, including cathodoluminescence which has not yet been reported by other researchers, will be compared to the earlier reports which will be reviewed briefly.

2. Previous studies

To our knowledge the earliest report on the optical properties of Ce-doped silica produced with the sol-gel method was made by Malashkevitch *et al.* [3]. Absorption near 265 and 320 nm was attributed to charge transfer from oxygen to Ce^{4+} and the f-d transitions of Ce^{3+} respectively, while emission at 380 and 450 nm was attributed to Ce^{3+}-oxygen complexes having the nearest surroundings including Ce^{4+} or Ce^{3+} ions respectively. In a follow-up paper a large increase in luminescence intensity was reported for samples that were annealed in hydrogen instead of air and this was attributed to reduction of Ce^{4+} to Ce^{3+} [4]. In another early paper, Rand *et al*. [5] studied the luminescence of unannealed Ce-doped xerogels and found a single emission at 355 nm with the corresponding excitation spectrum peak at 254 nm. In a series of papers Cai *et al*. [6-9] first prepared and annealed undoped silica xerogels, and then soaked these in $Ce(SO_4)_2$ or $CeCl_3$ solutions or a Ce-containing sol, after which they were dried. In all cases the luminescence had a wavelength around 350 nm. Xu *et al.* [10] reported that a short wavelength emission near 357 nm occurred for samples processed at temperatures up to about 450°C, but at higher temperatures above 700°C this emission was replaced by a band at 450 nm when the Ce^{3+} ions become coordinated with the oxygen ions.

In dried but unannealed Ce-doped silica, Patra *et al*. [11] measured fluorescence at 405 nm and 445 nm. In samples annealed at 1000°C and excited at 250 nm luminescence was found at 450 nm, with an additional peak at 360 nm which only occurred in samples annealed in nitrogen instead of oxygen [12]. For samples excited at 337 nm by a xenon lamp the main emission band was at 410 nm with a shoulder at 450 nm, but it is surprising that almost precisely the same emission was obtained for the undoped sample [13]. When the excitation wavelength was reduced to 308 nm the spectrum of the undoped sample was unchanged, but for the Ce-doped samples additional luminescence was found near 370-380 nm.

Radioluminescence of sol-gel Ce-doped silica has been intensively studied at the University of Milano-Bicocca. Vedda *et al*. [2] reported insignificant radioluminescence for undoped sol-gel silica in comparison to Ce-doped samples densified at 1050°C emitting near 2.75 eV (i.e. 450 nm). Although there is some variability from 415 to 475 nm in the radioluminescence peak position in later reports [14-18], a recent study claims

that for a large variety of samples the luminescence can be fitted by two Gaussians with peaks centred at 2.7 and 3.1 eV (460 and 400 nm) [19]. This separation is too large to account for the spin-orbit splitting of the f-levels (0.25 eV) – instead the high energy peak at 400 nm is attributed to Ce^{3+} ions which are not isolated in the lattice, but instead occur in or near the surface of amorphous clusters.

From the Physics Department at the University of the Free State the photoluminescence peak from Ce-doped sol-gel silica has been reported at 417 nm [20], at 423 nm [21], at 430 nm [22] and at 445 nm [23]. In addition, intrinsic photoluminescence from pure sol-gel silica has been reported at 425 nm [24], at 450 nm [25] and at 490 nm [26], while cathodoluminescence has been reported at 445 nm [27]. While different sample preparation methods may account for some variability, it is clear that intrinsic luminescence from pure SiO_2 and luminescence from Ce-doped silica may be difficult to identify unambiguously.

3. Experimental

Sol-gel silica samples were produced by allowing tetraethylorthosilicate (TEOS) to react with water. Ethanol was used as a solvent, nitric acid was added to catalyze the reaction and Ce nitrate was added to produce doped samples. After stirring for several hours, mixtures were stored in closed containers at 50°C until the formation of a gel. This was dried, annealed at 1000°C and ground to a fine powder. Some samples were annealed in a reducing atmosphere created by placing charcoal close to (but isolated from) the samples in the oven. Luminescence measurements were made using a variety of excitation sources, including a 325 nm He-Cd laser, a 248 nm Ne-Cu laser, a xenon lamp, synchrotron radiation at the SUPERLUMI station at DESY and 2 kV electrons at a current of 12 μA for cathodoluminescence.

4. Results and Discussion

Figure 1 shows the photoluminescence results obtained using a 325 nm He-Cd laser as excitation source. It is clear that samples which have been annealed in air rather than a reducing atmosphere exhibit much less luminescence, and that for these samples the undoped silica emitting at 446 nm is more luminescent than the Ce-doped samples,

indicating that the Ce acts to quench the defect luminescence. This defect luminescence was also reported by Reisfeld *et al.* [13] in undoped silica and most likely corresponds to the Si ODC(II) defect [28]. For the undoped silica annealed with charcoal the defect luminescence is greater, which may be as the result of an increase in the number of oxygen vacancy defects created by the reducing atmosphere. For the reduced sample doped with 1 mol% Ce the emission is near the same wavelength, but much stronger (this plot has been scaled down by a factor of 10 in the figure). Its emission has a prominent long wavelength shoulder and is fitted well by two gaussian peaks at energies 2.718 and 2.494 eV (456 and 497 nm respectively), separated by 0.224 eV. This is consistent with the fact that for Ce^{3+} ions the ^2F ground state is split by spin-orbit interaction into two levels separated by about 0.25 eV. The luminescence of the reduced sample doped with 4 mol% Ce is similar to that of the undoped sample - in this heavily doped sample concentration quenching probably limits the luminescence from the Ce, although it is difficult to ascertain whether the luminescence in this sample is as a result of the defects or the Ce (or both). Future measurements of decay times may be of value to distinguish these sources.

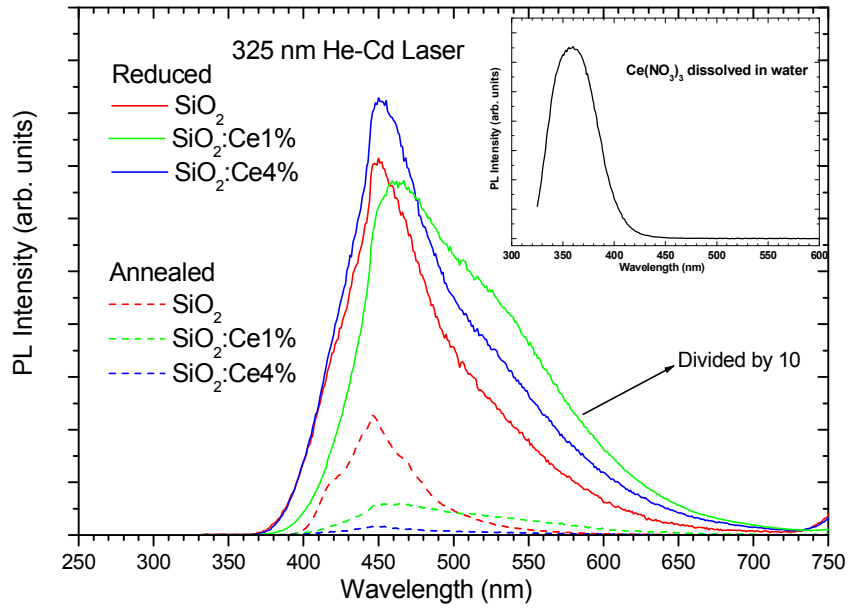

Figure 1: Photoluminescence of Ce-doped silica excited by a 325 nm He-Cd laser. The inset is the PL of $Ce(NO_3)_3$ dissolved in water excited by 305 nm Xe lamp

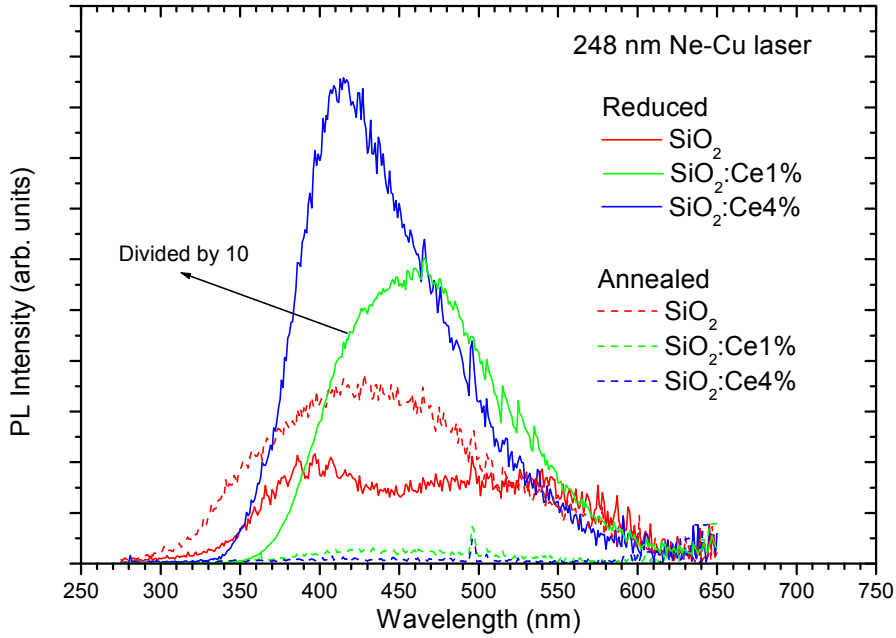

Figure 2: Photoluminescence of Ce-doped silica excited by a 248.6 nm Ne-Cu laser.

Figure 2 shows the photoluminescence from the same samples obtained using a 248.6 nm Ne-Cu laser as the excitation source. Here the luminescence spectra of the undoped samples are wider and extend to shorter wavelengths and the reduced sample shows less luminescence than the sample annealed in air. Again the 1% Ce-doped reduced sample emits most strongly and can be fitted by a single Gaussian peak at energy 2.728 eV (455 nm). The doped samples annealed in air have very poor luminescence (the feature just below 500 nm is the second order peak of the laser), while the 4% Ce-doped reduced sample shows emission peaking at 415 nm. This short wavelength emission may be associated with defects – Reisfeld *et al*. [13] measured defect emission at 410 nm in undoped samples, which we suggest may be as a result of Ge impurities (possibly from the TEOS precursor) which emit near 400 nm [29]. Nevertheless, the fact that it is more intense than the defect emission in the reduced undoped sample indicates that emission from Ce^{3+} ions in amorphous clusters occurring at 400 nm [19] also contributes, especially since such clusters are more likely to be formed in the more heavily 4% doped samples.

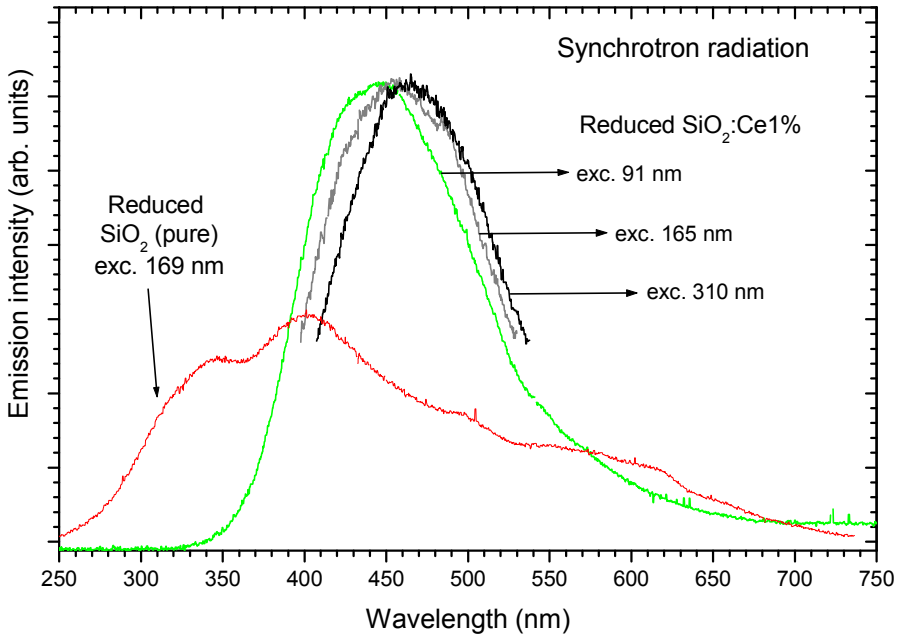

Figure 3: Photoluminescence of Ce-doped silica excited by synchrotron radiation.

Figure 3 shows the photoluminescence for reduced samples obtained using synchrotron radiation at various excitation wavelengths. For short wavelength excitation at 169 nm the emission from the undoped silica is broad, extending over the entire visible wavelength, with the dominant peak at 407 nm corresponding to the short wavelength defect emission of SiO_2 suggested earlier to be associated with Ge impurities. The 1% Ce-doped sample annealed in reducing atmosphere emits in a band which shifts in peak position from 445 nm to 465 nm as the excitation wavelength is increased. This emission is believed to be from Ce^{3+} incorporated into the silica and the lack of a short wavelength component near 400 nm from Ce in amorphous clusters may be attributed to the low Ce concentration, since in Figure 2 this component was found to occur strongly only in the 4% doped sample. Radiation at 91 nm excites the silica host since the interband gap of amorphous SiO_2 is approximately 9 eV (140 nm) [30], while excitation at 165 nm and 310 nm are believed to excite defects and the f-d transition of Ce^{3+} ions respectively. Together with the shift in emission wavelength, the lifetime of the emission measured at 460 nm was found to decrease from about 60 to 40 ns as the excitation wavelength was

increased. Both the blue-shift in emission and the longer lifetime associated with shorter wavelength excitation can be attributed to its indirect nature compared to the direct excitation of Ce^{3+} ions: some extra time elapses between indirect excitation and direct excitation of the Ce^{3+} ions, and there is the possibility of emission from higher energy levels before complete relaxation occurs.

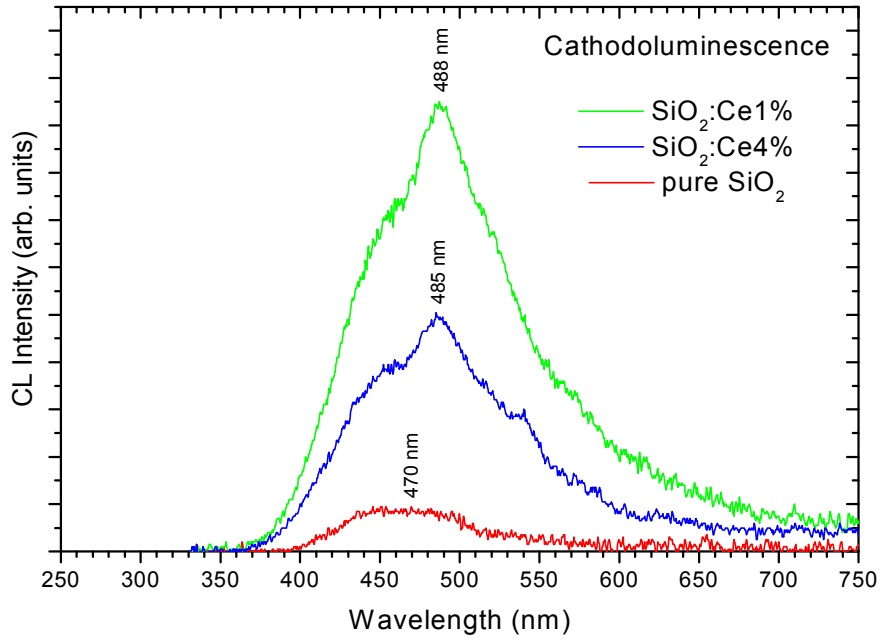

Figure 4: Cathodoluminescence of Ce-doped silica excited by a 2 keV electron beam.

Figure 4 shows the cathodoluminescence of pure and Ce-doped silica samples, all annealed in air and not a reducing atmosphere. Unlike for laser excitation where Ce-doped samples annealed in air showed very poor photoluminescence (far less than the undoped samples), under electron stimulation significant luminescence from these samples are obtained. This emission, peaking at 488 nm in the 1% Ce-doped sample, is at a significantly longer wavelength than attributed to emission from Ce in the photoluminescence results (for reduced samples). This, together with the fact that it occurs in air annealed samples which show negligible photoluminescence, suggests an alternative luminescence mechanism for these samples. According to Reisfeld *et al*. [13] a Ce^{4+} ion may capture an electron to form an excited Ce^{3+} ion according to Ce(IV) +

$e \rightarrow (Ce(III))^*$, which subsequently relaxes, emitting a photon. In air annealed samples dominated by Ce^{4+} ions under electron stimulation this process could account for the cathodoluminescence which is not observed for photoluminescence and the longer wavelength emission can be attributed to the different environment of Ce^{3+} and Ce^{4+} ions.

5. Conclusion

We have shown that reports of emission from Ce-doped silica in the literature vary widely. This represents a challenging system because of the nature of the amorphous host, its defect emissions, the variability in wavelength of cerium's f-d transitions depending on the ion's environment and the possibility of Ce occurring in either the Ce^{3+} or Ce^{4+} charge state. Several earlier reports suggested that the emission from Ce in silica occurs in the region of 350 nm and this is the value tabulated for Ce emission in silica by Dorenbos [1]. Our results show this emission for Ce^{3+} in $Ce(NO_3)_3$ dissolved in water (see the inset of Figure 1). Reports of this emission generally come from samples that have not been annealed at high temperatures and so it is suggested that this luminescence may originate from Ce that has not been incorporated in the silica. Bi *et al.* [9] have also suggested that the 350 nm emission occurs from Ce^{3+} ions that have not been "entrapped completely in the silica network", owing to the similarity of the luminescence to that from Ce^{3+} in solution. Furthermore, Xu *et al.* [10] have reported that this emission disappears for samples annealed above 700°C, but occurs for samples treated up to 400°C, and attribute it to Ce^{3+} ions coordinated to organic molecules or hydroxyl groups. Our photoluminescence results suggest that emission from Ce incorporated in the silica lattice occurs near 455 nm, similar to the wavelength of 450 nm reported by Xu *et al.* [10] for a peak that is found after high temperature processing of Ce-doped sol-gel silica and in numerous other previous studies of this material. It is also similar to the wavelength of 440 nm reported for Ce emission from silica grown by vapour-phase synthesis [31]. A second emission near 400 nm has been reported for radioluminescence measurements and associated with Ce^{3+} in amorphous clusters [19], which may account for the variability in the wavelength of the Ce peak between 400-450 nm in previous reports. Although the results presented here do not generally show evidence of such an emission, for the 4% Ce-doped reduced sample excited by the 248.6 nm laser (Figure 2)

there is a shift of emission to lower wavelengths that is consistent with it, and clusters are most likely to form in this highly doped sample. However, our results also confirm that emissions near both 400 and 450 nm also occur in undoped silica, as previously reported by Reisfeld *et al.* [13], which can make it difficult to distinguish the Ce emissions. For this reason it is important to include spectra of undoped samples for comparison, which is often neglected. Finally, we have reported new results on cathodoluminescence measurements of Ce-doped sol-gel silica. The samples used were annealed in air and show very poor photoluminescence, which is attributed to the Ce taking the non-luminescent tetravalent form. However, these samples do emit under electron beam excitation, although at a longer wavelength (around 490 nm) than that emitted by reduced samples during photoluminescence. We believe that by electron beam excitation Ce^{4+} ions can be stimulated by a process of electron capture into excited Ce^{3+} ions which are responsible for the luminescence. The change in emission wavelength can then be attributed to the different environments of the Ce^{4+} and Ce^{3+} ions.

References

[1] Dorenbos P 2000 *J. Lumin.* **9**1155

[2] Vedda A, Baraldi A, Canevali C, Capelletti R, Chiodini N, Francini R, Martini M, Morazzoni F, Nikl M, Scotti R and Spinolo G 2002 *Nucl. Instrum. & Meth. A* **486** 259

[3] Malashkevitch GE, Poddenezhny EN, Melnichenko IM and Boiko AA 1995 *J. Non-Cryst. Sol***. 188** 107

[4] Malashkevitch GE, Melnichenko IM, Poddenezhny EN and Boiko AA 1999 *J. Non-Cryst. Sol.* **260** 141

[5] Rand ER, Smuckler MB, Go E, Bradley MS and Bruno JW 1995 *Inorganica Chimica Acta* **233** 71

[6] Cai W, Zhang Y and Zhang L 1998 *J. Phys.: Condens. Matter* **10** L473

[7] Cai W, Zhou H and Zhang L 1999 *J. Mat. Sci. Lett.* **18** 1849

[8] Cai W, Zhang Y and Zhang L 1999 *J. Mater. Res.* **14** 1922

[9] Bi H, Cai C and Zhang L 2000 *Mat. Res. Bull.* **35** 1495

[10] Xu GQ, Zheng ZX, Tang WM and Wu YC 2007 *J. Lumin.* **124** 151

[11] Patra A, Kundu D and Ganguli D 1997 *J. Sol-Gel Sci. & Tech.* **9** 65

[12] Reisfeld R, Minti H, Patra A, Ganguli D and Gaft M 1998 *Spectrochimica Acta A* **54** 2143

[13] Reisfeld R, Patra A, Panczer G and Gaft M 1998 *Optical Materials* **13** 81

[14] Vedda A, Chiodini N, Di Martino D, Fasoli M, Martini MF, Moretti E, Rosetta M, Spinolo G, Nikl M, Solovieva N, Baraldi A and Capelletti R 2004 *J. Non-Cryst. Sol.* **345&346** 338

[15] Vedda A, Chiodini N, Martino D, Fasoli M, Martini M, Paleari A, Spinolo G, Nikl M, Solovieva N, Baraldi A and Capelletti R 2005 *phys. stat. sol (c)* **2** 620

[16] Canevali C, Mattoni M, Morazzoni F, Scotti R, Casu M, Musinu A, Krsmanovic R, Polizzi S, Speghini A and Bettinelli M 2005 *J. Am. Chem. Soc.* **127** 14861

[17] Vedda A, Chiodini N, Di Martino D, Fasoli M, Morazzoni F, Moretti F, Scotti R, Spinolo G, Baraldi A, Capelletti R, Mazzera M and Nikl M 2006 *Chem. Mater.* **18** 6178

[18] Scotti R, Canevali C, Polizzi S, Bettinelli M, Speghini A and Morazzoni F 2006 *Int. J. Photoenergy* Article ID 24279

[19] Fasoli M, Vedda A, Lauria A, Moretti F, Rizzelli E, Chiodini N, Meinardi F and Nikl M 2009 *J. Non-Cryst. Sol.* **355** 1140

[20] Ntwaeaborwa OM and Holloway PH 2005 *Nanotechnology* **16** 865

[21] Ntwaeaborwa OM, Swart HC, Kroon RE, Holloway PH and Botha JR 2006 *Surf. & Int. Anal.* **38** 458

[22] Ntwaeaborwa OM, Swart HC, Kroon RE, Holloway PH and Botha JR 2006 *J. Phys. Chem. Sol.* **67** 1749

[23] Koao LF, Swart HC, Obed RI and Dejene FB 2011 *J. Lumin.* **131** 1249

[24] Ntwaeaborwa OM, Swart HC, Kroon RE, Botha JR, Ngaruiya JM and Holloway PH 2008 In *"Photoluminescence Research Progress"* (Eds. H.K. Wright and G.V. Edwards, Nova Science Publishers) 287

[25] Biggs MM, Ntwaeaborwa OM, Terblans J.J and Swart HC 2009 *Physica B* **404** 4470

[26] Ntwaeaborwa OM, Swart HC, Kroon RE, Terblans J.J and Holloway PH 2009 *J. Vac. Sci. Technol.* A **27** 767

[27] Dhlamini MS, Mhlongo G and Hillie KT 2010 *Optical Materials* **33** 79

[28] Skuja L 1998 *J. Non-Cryst. Sol.* **239** 16

[29] Bredol M, Gutsov S and Jüstel Th 2003 *J. Non-Cryst. Sol.* **321** 225

[30] DiStefano TH and Eastman DE 1971 *Sol. State Comm.* **24** 2259

[31] Voropai ES, Gorbachev SM, Saedchikov VA and Cherenda NG 1988 *J. Appl. Spectroscopy* **48** 149

Chapter IX

Effect of annealing on the Ce^{3+}/Ce^{4+} ratio measured by XPS in luminescent SiO_2:Ce

1. Introduction

Ce doped silica has potential applications as a luminescent material as phosphors for cathodoluminescence, scintillators and detectors [1]. Ce ions can occur in a trivalent or a tetravalent state: only the trivalent Ce^{3+} state with a single 4f electron is optically active, while the tetravalent Ce^{4+} ion is non-luminescent. X-ray photoelectron spectroscopy (XPS) is a suitable technique to investigate the oxidation states of Ce in cerium oxides and such studies have been carried out because of the importance of CeO_2/Ce_2O_3 conversion in automotive exhaust catalysts [2]. However, the XPS Ce3d spectrum of cerium oxide is rather complex as it contains ten closely spaced and overlapping peaks on a strong background. The main challenge is to obtain accurate fits to experimental data while still maintaining a good physical basis for the fitting parameters [3]. The analysis of Ce in SiO_2:Ce is even more challenging since the Ce concentration for luminescent samples is only in the region of 1 mol%. Although it has been experimentally shown that to improve the luminescence efficiency of Ce doped silica is to anneal it in a reducing atmosphere [4], with the implication that this increases the concentration of Ce^{3+} luminescent ions, there is no evidence of XPS measurements that correlate the relative concentrations of the Ce^{3+} and Ce^{4+} ions to the luminescent properties. In this work, cerium doped silica was prepared by the sol-gel method. The effect of annealing atmosphere on the luminescent properties is correlated to XPS measurements of the oxidation state of Ce in the samples.

2. Experimental

Ce-doped SiO_2 glass was prepared by the sol–gel method using tetraethylorthosilicate (TEOS), water, ethanol (C_2H_5OH) and $Ce(NO_3)_3$ as starting materials and nitric acid (HNO_3) as a catalyst. The molar ratio of TEOS:H_2O:C_2H_5OH was 1:5:10, and the HNO_3 concentration was 0.015 M in water. TEOS was mixed with ethanol and stirred for 30 minutes after which the acidified water was added and stirring was continued for

another 30 minutes. After that $Ce(NO_3)_3$ was dissolved in a little ethanol and added to the mixture, which was stirred for a further 4 h. Then the mixture was stored in a closed container and transferred to a water bath at 50°C until a gel was formed. The gel was dried, crushed and divided into two parts, one part annealed in air at 1000°C for 2 h, and the other part annealed at flowing 4% hydrogen in argon atmosphere for the same time and temperature. XPS measuremnt were made using two different spectrometers, PHI 5400 ESCA and PHI 5000 Versaprobe both using Al x-rays. The powder sample was deposited onto a conductive carbon tape stuck to the sample holder. Charging shifts of the spectra were corrected using the known values of the C1s and/or Si2p peaks. Photoluminescence was measured at room temperature with a Cary Eclipse fluorescence spectrophotometer equipped with a xenon lamp. Diffuse reflectance spectra were recorded using a Lambda 950 UV–Vis spectrophotometer with an integrating sphere.

3. Results and Discussions

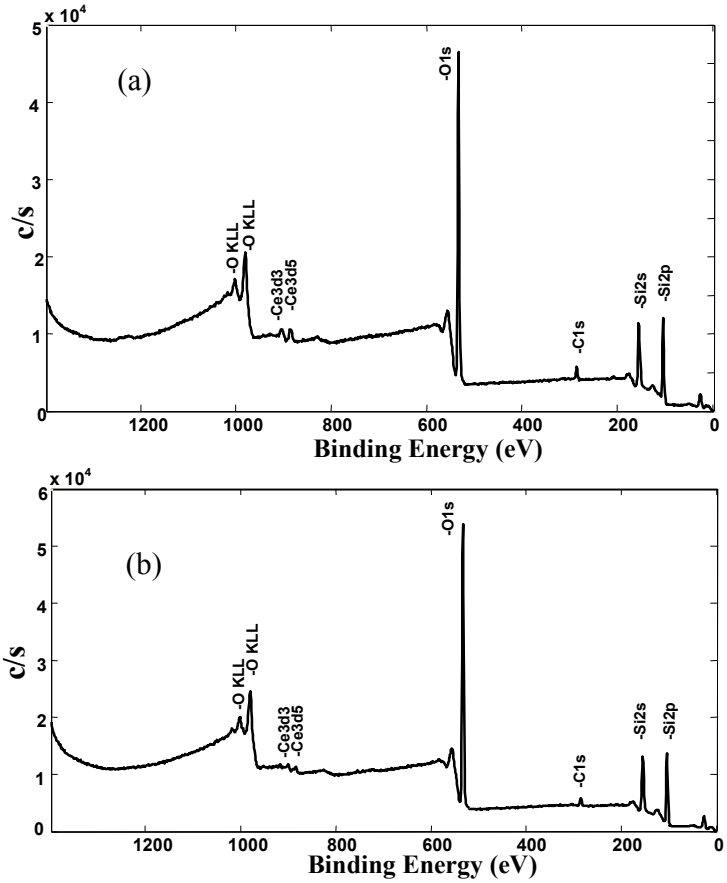

Figure 1: XPS survey scan spectrum of the (a) reduced sample, (b) annealed sample

3.1 XPS

For XPS analysis a higher dopant concentration (4 mol%) was used than what is required for good luminescence (0.5 mol%) to obtain a reasonable Ce3d signal. Figure 1 (a) shows the full range survey scan spectrum of the reduced sample. The spectrum is dominated by four photoelectron peaks, corresponding to electrons originating in the 2p orbital of the Si, 1s orbitals of the C and O and 3d orbital of the Ce atoms in the sample surface. The existence of the C atoms on the sample surface can be ascribed to three possible reasons: from adventitious hydrocarbon nearly always present, or from the precursors, or from the carbon tape used to stick the powder to the sample holder. In figure 1 (b) the survey scan spectrum of the annealed sample is presented. Small different between the reduced and annealed spectrum can be seen, such as the carbon peak in the annealed spectrum is smaller than the carbon peak in the reduced spectrum indicating less carbon in the surface of the annealed sample. Also the shape of the Ce peaks is different in the two spectra due to the oxidation state of the Ce in the two samples. To investigate this difference in more detail, high resolution scan of the Ce peaks were taken. Multipak version 8.2c software was used to fit the Ce3d pattern. The spectrum was fitted with 10 Gaussian peaks, two doublet peaks of the spin–orbit split 5/2;3/2 components attributed to the final states of Ce^{3+} and three doublet peaks of the spin–orbit split 5/2;3/2 components attributed to the final states of Ce^{4+} (see Tables 1 and 2).

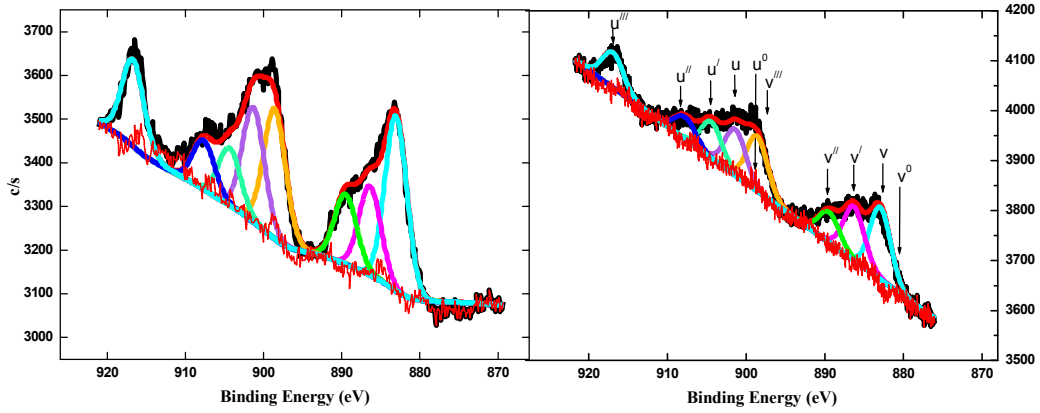

(a) (b)

Figure 2: Ce3d XPS spectra of the annealed sample obtained by (a) PHI 5000 (b) PHI 5400.

Table 1: Fit parameter of the annealed sample.

ion	$3d_{5/2}/3d_{3/2}$	Peak pos. (eV)	final state	%area	%total
Ce^{4+}	v/u	882.3/901.0	Ce $3d^9 4f^2$ O $2p^4$	36	80
	v''/u''	888.9/907.5	Ce $3d^9 4f^1$ O $2p^5$	16	
	v'''/u'''	898.2/916.8	Ce $3d^9 4f^0$ O $2p^6$	28	
Ce^{3+}	v^0/u^0	880.5/898.8	Ce $3d^9 4f^2$ O $2p^5$	0	20
	v'/u'	885.7/904.1	Ce $3d^9 4f^1$ O $2p^6$	20	

Peak position, spin–orbit splitting, area ratio and Full Width at Half Maximum (FWHM) are fitting parameters that need to be controlled in order to perform good fits with physically meaningful parameters. Figure 2(a) and (b) show the detailed Ce3d XPS spectra of the sample annealed at 1000°C obtained by PHI 5000 and PHI 5400 respectively. The spectra were fitted with 10 peaks and the FWHM of all the peaks was kept the same for each fit. The peaks positions and the spin–orbit splitting agree well with the literature [5] and the intensity ratio between $3d_{5/2}$ and $3d_{3/2}$ was taken as 3:2 [6]. Six peaks labelled as v/u , v''/u'' and v'''/u''' referring to three doublets of the spin–orbit split components are attributed to Ce^{4+} final states. The high binding energy doublet v'''/u''' at 898.2 and 916.8 eV are attributed to the final state of Ce $3d^9 4f^0$ O $2p^6$, doublet v''/u'' at 888.9 and 907.5 eV are attributed to the state of Ce $3d^9 4f^1$ O $2p^5$, and doublet v/u at 882.3 and 901.0 eV correspond to the state of Ce $3d^9 4f^2$ O $2p^4$. The other four peaks labelled as v^0/u^0 and v'/u' referring to two doublets of the spin–orbit split components are attributed to Ce^{3+} final states. The doublet v'/u' at 885.7 and 904.1 eV are corresponding to the final state of Ce $3d^9 4f^1$ O $2p^6$ and the doublet v^0/u^0 at 880.5 and 898.8 eV correspond to the final state of Ce $3d^9 4f^2$ $O2p^5$. Table 1 lists the fit parameters obtained from the spectra of the PHI 5000. The peak area percentage can be used to determine the relative concentrations [6]. From the table the relative total concentration of the Ce^{4+} is 80% while that of the Ce^{3+} is 20%. From the PHI 5400 spectrometer, the calculated relative concentrations of Ce^{4+} and Ce^{3+} are 75% and 25% respectively. The different values given by the two spectrometers can be taken as an indication of the accuracy of the technique.

Figure 3(a) and (b) shows the Ce3d XPS spectra of the reduced sample obtained by the PHI 5000 and PHI 5400 respectively. The Ce^{4+} u''' characteristic peak has almost disappeared indicating that the sample contains less Ce^{4+}. The spectra can be fitted with

the four peaks v^0/u^0 and v'/u' of the Ce^{3+} components, in addition of the doublet v/u peaks of Ce^{4+} in the valley between (v^0 and v') and (u^0 and u'). Table 2 lists the fit parameters for the spectra obtained by the PHI 5000 from the reduced sample. The total relative concentration of the Ce^{3+} is 73% which compares well with the 71% measured by the PHI 5400. There were some difficulties to fit these spectra. The software can not subtract the background well in the spectra obtained by PHI 5000, using either the Shirley or iterated Shirley algorithms. While the background was subtracted succesfully in the spectra obtained by PHI 5400, the two seperate bands could not fit well simultaneously without relaxing the physically important constraints. Ce3d XPS spectra and their fitting obviously show that reducing the sample with hydrogen can improve the Ce^{3+} concentration.

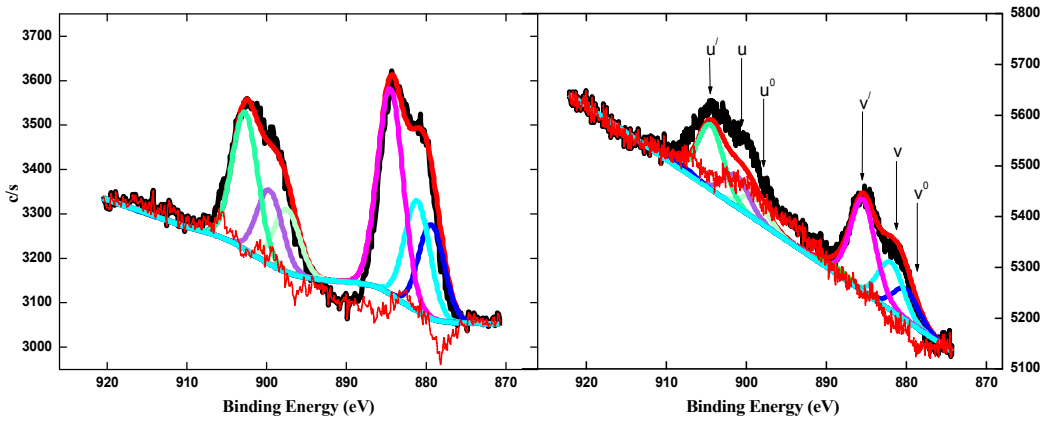

(a) (b)

Figure 3: Ce3d XPS spectra of the reduced sample obtained with the (a) PHI 5000 and (b) PHI 5400 XPS systems.

Table 2: Fit parameter of the reduced sample.

ion	$3d_{5/2}/3d_{3/2}$	Peak pos. (eV)	final state	%area	%total
Ce^{4+}	v/u	882.3/901.0	Ce $3d^9 4f^2$ O $2p^4$	27	27
	v"/u"	888.9/907.5	Ce $3d^9 4f^1$ O $2p^5$	0	
	v'"/u'"	898.2 /916.8	Ce $3d^9 4f^0$ O $2p^6$	0	
Ce^{3+}	v^0/u^0	880.5/898.8	Ce $3d^9 4f^2$ O $2p^5$	23	73
	v'/u'	885.7/904.1	Ce $3d^9 4f^1$ O $2p^6$	50	

3.2 Photoluminescence and UV–Vis spectroscopy

Figure 4(a) shows the PL of the reduced and annealed samples. The sample which was annealed in air does not show significant emission, while the reduced one exhibits a high intensity emission. The sample annealed in air may contain more Ce^{4+} which is optically in-active [7]. A significant PL emission is observed in the reduced sample which may containing more Ce^{3+} rather than Ce^{4+} and significant PL emission observed. These results are consistent with the XPS measurements done on the two samples. Figure 4(b) shows the reflectance spectra done on the annealed and the reduced samples. The optical reflectance profile from the annealed sample exhibits a wide absorption peak which corresponds to Ce^{4+} ion absorption due to charge transfer from O^{2-} to Ce^{4+} [8]. In the reduced sample an absorption peak appeared at around 338 nm, which corresponds to the 4f to 5d transition of Ce^{3+} [9,10].

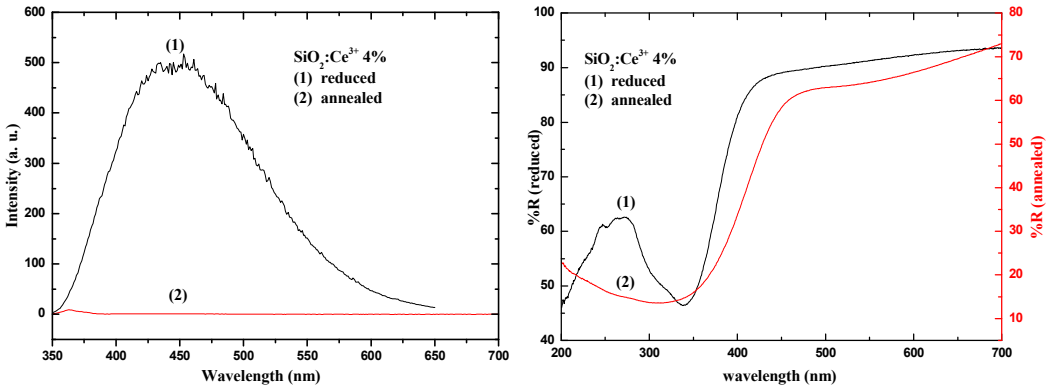

(a) (b)

Figure 4: (a) Photoluminescence and (b) diffuse reflectance of reduced and annealed samples

4. Conclusion

Ce ions were successfully incorporated into SiO_2 by the sol-gel process. Ce 3d XPS spectra analysis indicates that the concentration of the Ce^{3+} was increased in the reduced sample. This is in contrast to other published results [11] where samples subjected to rapid thermal annealing using an oxidising oxygen-hydrogen flame exhibited an increase

in luminescence despite indications that the Ce^{4+} concentration had increased. The reduced sample shows a high intensity PL emission compared to the annealed sample. UV–Vis spectroscopy done on the reduced sample shows an absorption peak associated with the Ce^{3+} ion while the annealed samples shows an absorption peak associated with the Ce^{4+} ion. The photoluminescence and UV–Vis spectroscopy results are consistent with the XPS measurements.

References

[1] Reisfeld R, Patra A, Panczer G and Gaft M 1999 *Opt. Mat.* **13** 81

[2] Larachi F, Pierre J, Adnot A, and Bernis A 2002 *Appl. Surf. Sci.* **195** 236

[3] Paparazzo E 2011 *Mat. Res. Bulletin* **46** 323

[4] Fasoli M, Vedda A, Lauria A, Moretti F, Rizzelli E, Chiodini N, Meinardi F and Nikl M 2009 *J. Non-Cryst. Solids* **355** 1140

[5] Limei Q, Fen L, Liangzhong Z, Ying M and Jiannian Y 2006 *Appl. Sur. Sci.* **252** 4931

[6] Moulder F, Stickle WF, Sobol PE and Bomben KD 1995 *Handbook of X-ray Photoelectron Spectroscopy* (Japan: Physical Electronics) p 10

[7] Xu G Q, Zheng ZX, Tang WM and Wu YC 2007 *J. Lumin.* **124** 151

[8] Ligang Z, Anxian L, Chenggang Z and Weiqun S 2011 *J. Alloys Compds* **509** 7789

[9] Paul A, Mulholland M and Zaman MS 1976 *J. Mater. Sci.* **11** 2082

[10] Weipingyz C, Yeyz Z and Lideyz Z 1998 *J. Phys Condens. Matter* **10** L473

[11] Chiodini N, Fasoli M, Martini M, Rosetta E, Spinolo G and Vedda A 2002 *Appl. Phys. Lett.* **81** 4374

Chapter X

High efficiency energy transfer in Ce,Tb co-doped silica

1. Introduction

Phosphors are widely applied in lighting, displays, lasers, scintillators, etc. Generally host materials should exhibit good optical, mechanical and thermal properties [1]. Microporous silica prepared by the sol-gel technique is considered to be an optically inert medium and its chemical and thermal stability increase its attractiveness as a host for luminescent ions [2]. Further advantages of the sol-gel process are that it can produce very pure glass at temperatures well below the melting point, and it allows incorporation of much higher concentration of dopants than the melt process [3,4]. Lanthanide group ions may be used as luminescent centres [5]. These ions have partially filled f-level electron shells, giving rise to various electron transitions in the UV, visible and IR regions of spectrum.

Energy transfer can play an important role in phosphor materials as it can be used to enhance the luminescence efficiency [6]. Ce^{3+} ions are an efficient sensitizer to Tb^{3+} ions and co-doping has been studied in a variety of hosts [7-13]. Tb ions are used as the activator because their bright green emission is suitable for many applications. Although Tb ions can be excited efficiently through their allowed 4f-5d transition, it can be advantageous to use Ce ions as a sensitizer because their allowed 4f-5d transition occurs at a longer (generally more accessible and convenient) wavelength. Ce ions can occur in a trivalent or a tetravalent state. Only the trivalent Ce^{3+} state with a single 4f electron is optically active, while the tetravalent Ce^{4+} ion is non-luminescent. Annealing in a reducing atmosphere can convert tetravalent Ce ions to the trivalent form, thus improving the Ce luminescence [14]. Ntwaeaborwa *et al.* [10] have reported some initial results on energy transfer from Ce to Tb in sol-gel silica. In this chapter we report a much greater enhancement of the Tb luminescence excited via Ce at 325 nm in co-doped samples by annealing the samples in a reducing atmosphere, instead of air, in order to convert Ce from non-luminescent tetravalent ions to optically active trivalent ions.

2. Experimental details

Ce and Tb single doped, as well as Ce,Tb co-doped, silica was produced using the sol-gel method by allowing tetraethylorthosilicate (TEOS) to react with water. Ethanol was used as a solvent, nitric acid was added to catalyze the reaction and Ce and/or Tb nitrate was added to produce doped and co-doped samples. After stirring for several hours, mixtures were stored in closed containers at 50°C until a gel was formed. This was dried, ground to a fine powder and annealed in air at 600 or 1000°C for 2 hours. The reduced samples were annealed in flowing 4% hydrogen in argon gas for the same temperatures and time. Some samples were reduced in charcoal environment. Details of the preparation procedure have been published elsewhere [15]. X-ray diffraction (XRD) measurements were performed with a Bruker D8 diffractometer. A Bruker Tensor 27 was used to perform the Fourier Transform Infrared (FTIR) absorption measurements from 4000 to 400 cm^{-1}. Diffuse reflectance spectra were recorded using a Lambda 950 UV-Vis spectrophotometer with an integrating sphere and using spectralon as a reflectance standard. Photoluminescence (PL) measurements were made at room temperature using a Cary Eclipse fluorescence spectrophotometer equipped with a xenon lamp.

3. Results and discussion

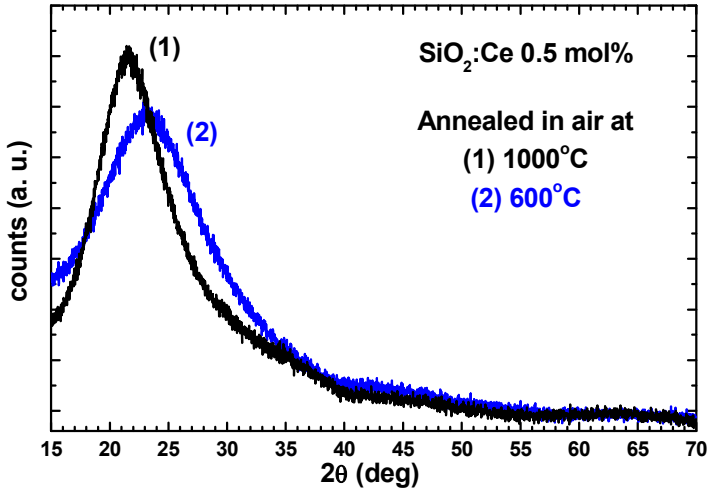

Figure 1: XRD spectra of sol-gel SiO_2:Ce 0.5 mol% (measured at room temperature after annealing at 600°C and 1000°C).

Figure 1 shows the XRD results of SiO_2:Ce 0.5 mol% annealed at 600°C and 1000°C. The sample annealed at 600°C exhibited the well known characteristics broad peaks of

amorphous silica [16,17], which narrowed slightly after annealing at 1000°C, indicating a less disordered yet still amorphous sample. This is in contrast to the results of Nagpure *et al*. [18] who reported a low-quartz crystalline phase in silica prepared by the combustion method and annealed at 1000°C, indicating the advantage of the sol-gel process for producing a single amorphous phase. There are no significant changes in the XRD spectra for the samples due to the dopants, nor for those heated in a reducing atmosphere instead of air.

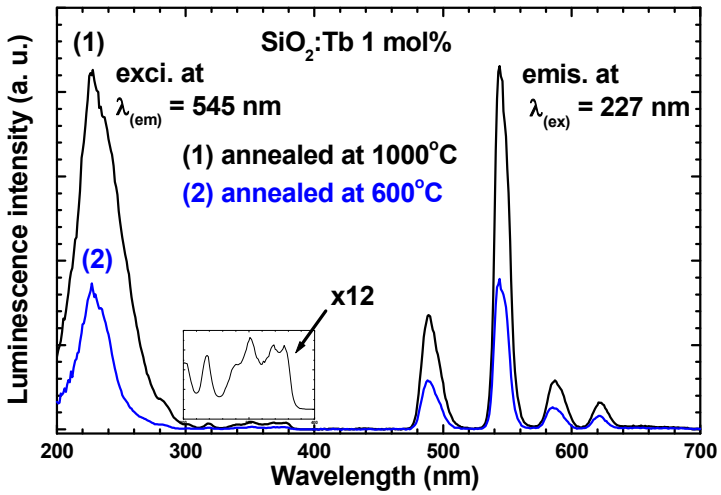

Figure 2: Excitation and emission spectra of SiO_2:Tb 1 mol% annealed at 600°C and 1000°C in air. The inset shows the f-f absorption bands of Tb

Figure 2 shows the excitation and emission spectra of SiO_2:Tb 1 mol% annealed at 600°C and 1000°C. The optimum excitation wavelength of 227 nm is associated with the 4f-5d transition of Tb^{3+} ions [19]. The emission spectra showed the characteristic emission bands attributed to the $^5D_4$-^7F_J transitions (J = 6,5,4,3), with the dominant green band of the $^5D_4$-$^7F_5$ transition at 544 nm. Blue luminescence from $^5D_3$-^7F_J transitions of Tb is not observed. The relatively high Tb concentration (1 mol%) allows cross relaxation which quenches emission from the $^5D_3$ level, whereas for a lower Tb concentration of 0.1 mol% in silica the $^5D_3$-^7F_J transitions are observed [20]. The sample annealed at 1000°C exhibited higher luminescence intensity compared to the sample annealed at 600°C. FTIR spectra (Figure 3) indicate that annealing at 600°C could not effectively remove all water and hydroxyl ions present in the sol-gel process, which can then quench the luminescence. The absorption near 3447 cm^{-1} is attributed to the stretching vibration of

hydroxyl ions (O-H), while the absorption near 1636 cm^{-1} is attributed to water molecules. The three bands near 460, 798 and 1094 cm^{-1} are attributed to the silica host Si-O-Si, O-Si-O and Si-O asymmetric stretching respectively [21]. In fact, the FTIR spectra of Figure 3 are for Ce (not Tb) doped samples, but the absorption bands observed are associated either with the host silica or the water and hydroxyl ions rather than the dopants which are present in low concentration. It is expected that similar results would be obtained for Tb doped samples, consistent with the PL results, and therefore all subsequent annealing was performed at the higher temperature of 1000°C.

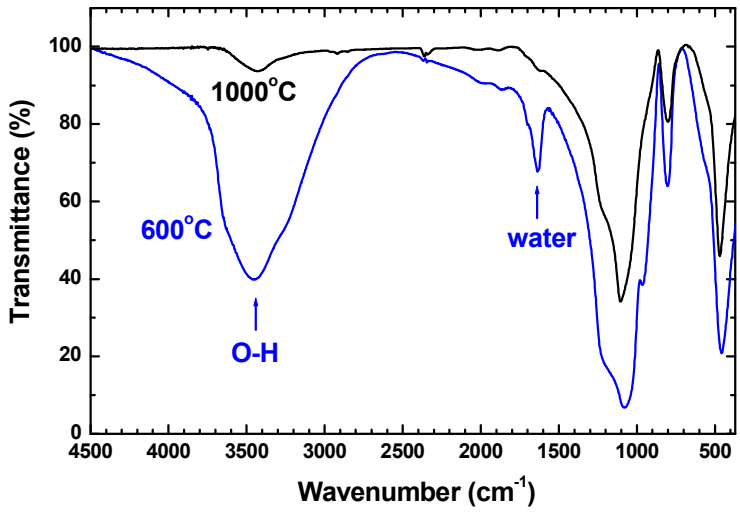

Figure 3: FTIR spectra of SiO_2:Ce 0.5 mol% annealed at 600 and 1000°C in air. The unlabeled bands below 1200 cm^{-1} are characteristic of silica.

Figure 4 shows the PL emission spectra of the Tb single doped and Ce,Tb co-doped samples annealed in air at 1000°C using 325 nm as the excitation wavelength. Note that although 325 nm is not the optimum excitation wavelength of the Tb doped samples (see the excitation spectra in Figure 2), nevertheless Tb emission is observed due to weak excitation within the f-levels of the Tb ions. Although the luminescence scale is much enlarged for Figure 4 compared to Figure 2, the spectrum of the Tb luminescence is

similar. The 325 nm was expected to excite the Ce ions in the co-doped samples and lead, through energy transfer to enhanced Tb emission. Unexpectedly, the PL emission intensity from the Tb ions was less in the Ce,Tb co-doped sample relative to the Tb single doped sample. This is in contrast to the result of Ntwaeaborwa *et al.* [10] where an enhancement in the Tb luminescence by a factor of about 4 times was reported. Sol-gel silica single doped with Ce and annealed in air did not show significant PL emission (Figure 5). UV-Vis diffuse reflectance measurements (Figure 6) gave absorption which is characteristic of non-luminescent Ce^{4+} ions and is attributed to charge transfer from O^{2-} to Ce^{4+} [22]. The incorporation of Ce in the tetravalent state rather than the trivalent state means energy transfer will not occur in Ce,Tb co-doped samples, and in addition the terbium emission may be reduced since a fraction of the incident light will be absorbed by the non-luminescent Ce^{4+} ions. However, in practice a mixture of Ce^{4+} and Ce^{3+} occurs [15] and the ratio could depend on the details of the sol-gel preparation method. It is suggested that the samples of Ntwaeaborwa *et al.* [10] may have contained a higher proportion of Ce^{3+} ions than those prepared in this study, which may have lead to the small enhancement of the Tb emission after co-doping with Ce.

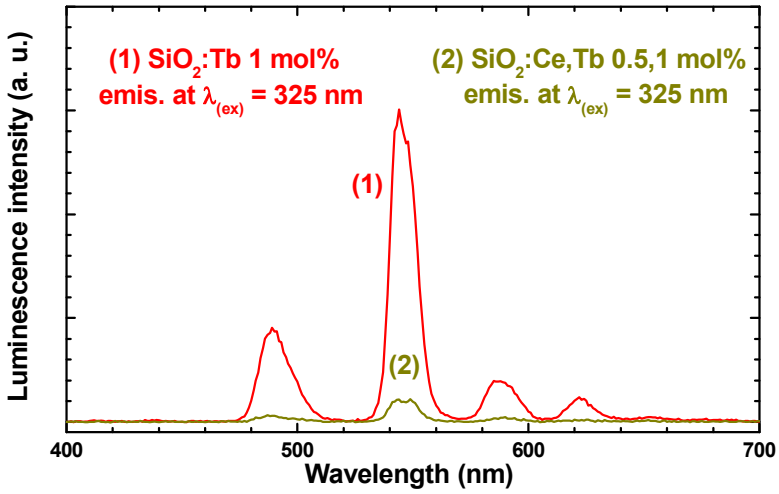

Figure 4: Emission spectra of SiO_2:Tb 1 mol% and of SiO_2:Ce,Tb 0.5,1 mol% annealed in air at 1000°C.

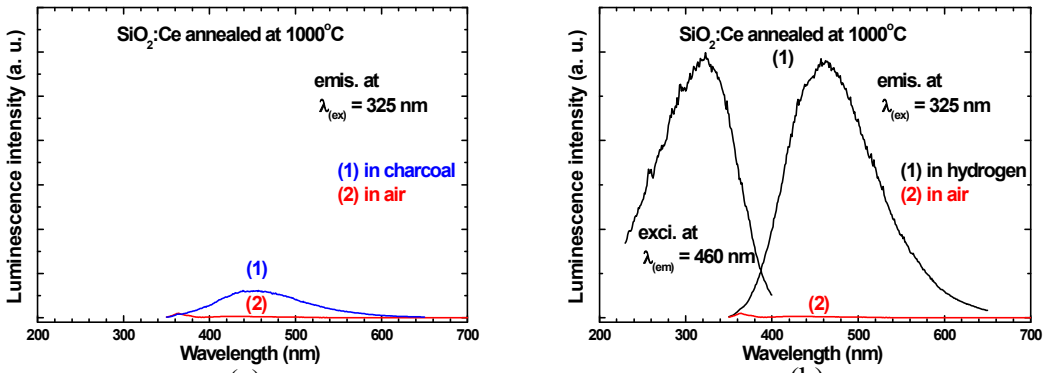

Figure 5: (a) Emission spectrum of SiO_2:Ce 1 mol% reduced with charcoal at 1000°C compared to the emission spectrum of the same sample annealed in air at 1000°C. (b) Excitation and emission spectra of SiO_2:Ce 0.5 mol% reduced with hydrogen at 1000°C compared to the emission spectrum of the same sample annealed in air at 1000°C.

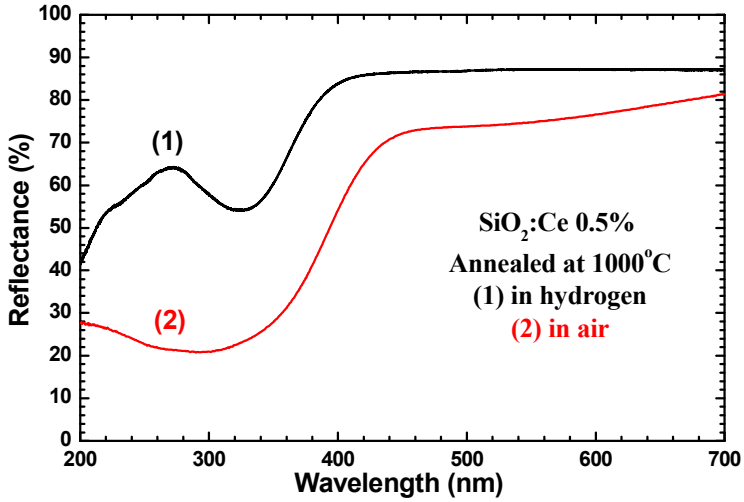

Figure 6: Diffuse reflectance of SiO_2:Ce 0.5 mol% annealed at 1000°C in air and a reducing atmosphere (4% hydrogen in argon).

To favour the formation of optically active Ce^{3+} ions, the Ce single doped samples were annealed in the presence of charcoal to create a reducing atmosphere. Such samples exhibited improved Ce luminescence (a broad blue emission band centred near 460 nm and attributed to 5d-4f transitions, with the excitation spectrum maximum near 325 nm) (Figure 5 (a)), but much better results were obtained by heating in flowing 4% hydrogen in argon gas. Such reduced Ce single doped samples now exhibited intense PL emission

(Figure 5 (b)) and the UV-Vis diffuse reflectance spectrum (Figure 6) was characteristic of Ce^{3+} ions [24,25]. The conversion of Ce^{4+} to Ce^{3+} was also confirmed using x-ray photoelectron spectroscopy and the details have been published elsewhere [15]. Heating in the reducing atmosphere instead of air did not have a significant effect on the FTIR results discussed earlier and a temperature of 1000°C was still required for good luminescence results. Silica samples doped singly with Tb gave the same PL luminescence results irrespective of whether they were annealed in air or the reducing atmosphere, indicating that the Tb is incorporated in the host as Tb^{3+} ions. Figure 7 shows the overlap region between the Tb excitation spectrum and the reduced Ce emission spectrum for singly doped silica samples, which is similar to that reported by Caldiño *et al.* for a zinc–sodium–aluminosilicate glass [12]. The Ce emission completely overlaps the $^5D_4$-$^7F_6$ excitation band of Tb near 480 nm, while its energy edge also overlaps higher excitation bands of Tb, e.g. $^5D_3$-$^7F_6$ near 380 nm, indicating that energy transfer may occur.

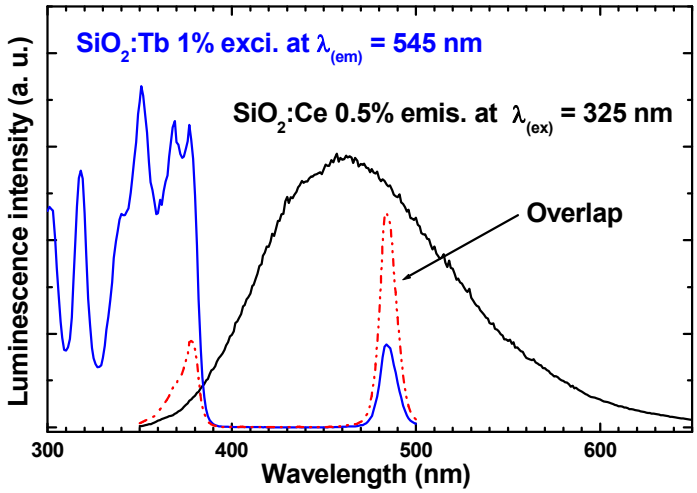

Figure 7: Overlap region of the excitation spectrum of Tb and the emission spectrum of reduced Ce for singly doped silica samples.

Figure 8 shows the PL spectrum of the Ce,Tb co-doped samples reduced at 1000°C using 325 nm as the excitation wavelength. The emission spectrum for the single doped Tb sample from Figure 4 is included for comparison, and now rather than the Tb emission of the co-doped sample being less than the singly doped sample, an enhancement due to

energy transfer from the Ce ions of about 240 times is obtained. Similar enhancement of Tb emission by co-doping with Ce has been reported by Liu *et al.* [23], although in their case the Ce emission occurred at about 375 nm rather than the 460 nm reported here. Fasoli *et al.* [14] have reported from radioluminescence measurements that the dominant Ce emission is found near 2.7 eV (i.e. 460 nm), while emission near 3.1 eV (i.e. 400 nm) is found only in samples sintered in a reducing atmosphere which they suggest originates from Ce near the surface of amorphous Ce-rich clusters. From the excitation spectrum of Figure 8 for the reduced co-doped sample measured for Tb emission at 545 nm one can see that the sample has excitation bands at 227 nm (Tb) as well as 325 nm (Ce). These excitation peaks are of similar height, and the Tb can be excited slightly more effectively via the Ce with energy transfer as when excited directly through the Tb f-d transition. The emission spectrum of the co-doped sample reveals that the Ce emission intensity is only about 3% of the value obtained without Tb being present, giving a value for the quantum efficiency for energy transfer from Ce to Tb of 97%.

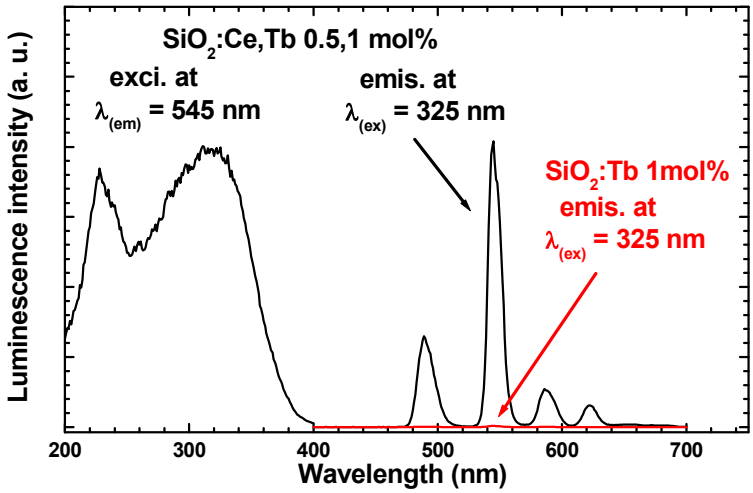

Figure 8: Excitation and emission (at λ_{ex} = 325 nm) spectra of SiO_2:Ce,Tb 0.5,1 mol% reduced in hydrogen at 1000°C compared to the emission (at λ_{ex} = 325 nm) spectrum of SiO_2: Tb 1 mol%.

To determine the optimum concentration of Ce which can give a high emission from Tb using 325 nm excitation, the concentration of Tb ions was kept constant at 1 mol% and the concentration of Ce ions was varied from 0 up to 4 mol%. Figure 9 shows the

relative intensity of Tb emission associated with the $^5D_4$-$^7F_5$ transition near 544 nm as a function of Ce concentration, normalized with respect to the sample containing no Ce, i.e. the Tb single doped sample. The results revealed that the Tb emission increased as the Ce concentration increased up to 0.5 mol% and then decreases at higher concentrations. This optimal concentration is in agreement with that given by Ntwaeaborwa *et al.* [10]. However, the enhancement of luminescence due to co-doping has been increased dramatically compared to these earlier results. We attribute this to the effective conversion of Ce^{4+} ions to Ce^{3+} ions in our samples through annealing in a reducing atmosphere.

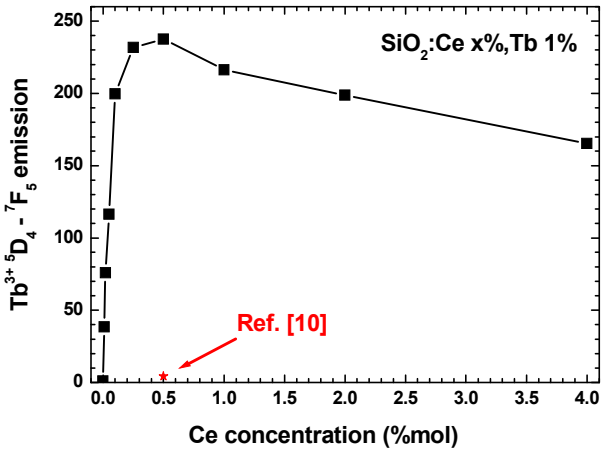

Figure 9: Relative intensity of Tb emission associated with $^5D_4$-$^7F_5$ transition as a function of Ce concentration using an excitation wavelength of 325 nm.

4. Conclusion

From these results it is clear that the details of how Ce-doped silica is produced using the sol-gel method can affect how much Ce is incorporated in the trivalent or tetravalent charge state. It may be possible to obtain a small but effective concentration of Ce^{3+} even when annealing in air as demonstrated by Ntwaeaborwa *et al.* [10], or almost all the Ce may be incorporated as non-luminescent Ce^{4+} as in this study. However, for good Ce luminescence in single doped samples, and for enhanced Tb emission via energy transfer from Ce in co-doped samples, it is important to anneal the samples at a higher temperature (1000°C) than 600°C as widely reported for sol-gel silica samples and to use

a reducing atmosphere instead of annealing in air. The Tb emission in co-doped Ce,Tb silica samples prepared in such a way can be excited as effectively, via absorption of Ce^{3+} ions at 325 nm together with energy transfer, as by direct excitation of the Tb f-d absorption band near 227 nm. For a Tb concentration of 1 mol%, the optimum concentration of Ce co-doping was found to be 0.5 mol%.

References

[1] Yehoshua Y 2006 *The physics and engineering of solid state lasers* (Washington: International society for optical engineering)

[2] Guodong Q, Minquan W, Mang W, Xianping F and Zhanglian H 1997 *J. Lumin.* **75** 63

[3] Jan T, Johannes Z and Rolf C 2006 *J. Mater. Sci.* **41** 8173

[4] Silversmith AJ, Boye DM, Brewer KS, Gillespie CE, Lu Y and Campbell DL 2006 J. *Lumin.***121** 14

[5] Claire P, Anders H and Mikael L 2005 *J. Lumin.* **111** 265

[6] Nakazawa E and Shionoya S 1967 *J. Chem. Phys.* **47** 3211

[7] Tshabalala KG, Cho SH, Park JK, Pitale SS, Nagpure IM, Kroon RE, Swart HC and Ntwaeaborwa OM 2011 *J. Alloys Compd.* **509** 10115

[8] Xiou L, Xie Y, He M, Chen Y, Li W and Yu W 2010 *J. Rare Earths* **28** 225

[9] Zhenxiao F and Wenbo B 2008 *Solid State Sci.* **10** 1062

[10] Ntwaeaborwa OM, Swart HC, Kroon RE, Holloway PH and Botha RJ 2006 *J. Phys. Chem. Solids* **67** 1749

[11] Malashkevich GE, Semkova GI, Stupak AP and Sukhodolov AV 2004 *Phys. Solid State* **46** 1425

[12] Caldiño U, Speghini A, Álvarez F, Berneschi S, Bettinelli M, Brenci M and Righini GC 2011 *Opt. Mat.* **33** 1892

[13] Caldiño U, Speghini A and Bettinelli M 2006 *J. Phys. Condens. Matter* **18** 3499

[14] Fasoli M, Vedda A, Lauria A, Moretti F, Rizzelli E, Chiodini N, Meinardi F and Nikl M , 2009 *J. Non-Cryst. Solids* **355** 1140

[15] Seed Ahmed HAA, Roos WD, Ntwaeaborwa OM, Swart HC and Kroon RE 2011 in Proceedings of SAIP2011, the 56th Annual Conference of the South African Institute of Physics, edited by I. Basson and A.E. Botha (University of South Africa, Pretoria, 2011), p. 280. ISBN: 978-1-86888-688-3. Available online at http:\\www.saip.org.za.

[16] Lijuan W, Anhuai L, Changqiu W, Xishen Z, Dongjun Z and Rui L 2006 *J. Colloid Interface Sci.* **295** 436

[17] Kalapathy U, Proctor A and Shultz J 2000 *Bioresour Technol.* **73** 257

[18] Nagpure IM, Pitale SS, Tshabalala KG, Kumar V, Ntwaeaborwa OM, Terblans JJ and Swart HC 2011 *Mater. Res. Bull.* **46** 2359

[19] Kroon RE, Seed Ahmed HAA and Gusowski MA 2011 in Proceedings of SAIP2011, the 56th Annual Conference of the South African Institute of Physics, edited by I. Basson and A.E. Botha (University of South Africa, Pretoria, 2011), p. 162. ISBN: 978-1-86888-688-3. Available online at http:\\www.saip.org.za.

[20] Seed Ahmed HAA, Ntwaeaborwa OM, Gusowski MA, Botha JR and Kroon RE 2012 *Physica B* **407** 1653

[21] Hofman R, Westheim JGF, Pouwel I, Fransen T and Gellings PJ 1996 *Surf. Interface Anal.* **24** 1

[22] Ligang Z, Anxian L, Chenggang Z and Weiqun S 2011 *J. Alloys Compds* **509** 7789

[23] Liu Z, Dai N, Luan H, Sheng Y, Peng J, Jiang Z, Li H, Yang L and Li J 2010 *Optics Express* **18** 21138

[24] Paul A, Mulholland M and Zaman MS 1976 *J. Mater. Sci.* **11** 2082

[25] Weiping C, Ye Z and Lide Z 1998 *J. Phys. Condens. Matter* **10** L473

Chapter XI

Interaction mechanism for energy transfer from Ce to Tb ions in silica

1. Introduction

Energy transfer phenomena can play an important role in the development of luminescence materials. For example, the green luminescence from Tb^{3+} doped silica can be excited efficiently using a very short wavelength UV light near 227 nm [1]. However, the excitation wavelength can be shifted to a more accessible value of 325 nm by co-doping Tb^{3+} with Ce^{3+} ions. At this wavelength Ce^{3+} ions absorb and then transfer the energy to the Tb^{3+} ions. Many theoretical and experimental studies have been done on non-radiative energy transfer since Forster first treated it theoretically [2-7]. The process involves excitation of a donor followed by transfer of the excitation energy to an acceptor. Non-radiative energy transfer can be distinguished from radiative energy transfer, for which the acceptor absorbs the radiation (photon) emitted by the donor, by the fact that in the first case energy transfer is associated with a decrease in the donor lifetime, while in the second case the donor lifetime is not affected.

Forster developed a theory for the rate of non-radiative energy transfer by electric dipole-dipole interaction [2]. This was later extended by Dexter to involve the higher multipole interactions [3]. Dexter also created a model for shorter donor-acceptor distances based on the exchange interaction [3]. The transfer mechanisms differ according to the dependence of the transfer rate on the donor-acceptor distance. Inokuti and Hirayama [8] developed numerical methods on energy transfer that determine the mechanism responsible. Nakazawa and Shionoya [9] used these calculations to study the energy transfer between unlike trivalent rare-earth ions in glass. They found that the dipole-quadrupole interaction gave the best fit between theory and experiment. Mares *et al.* [10] investigated the mechanism of the energy transfer between Ce and Nd in YAG:Nd,Ce by fitting the decay curves of Ce to the theory of Inokuti and Hirayama [8] and reported that

both dipole-dipole and dipole-quadrupole mechanisms contribute to energy transfer. In this study, the theoretical calculations of Inokuti and Hirayama [8] are implemented in MATLAB and compared to experimental data to investigate the mechanism of the energy transfer from Ce to Tb in sol-gel silica.

2. Experimental

A series of 14 Ce,Tb co-doped silica samples with a fixed concentration of Ce (0.5 mol%) and varying concentration of Tb from 0 up to 0.8 mol% were produced by the sol-gel method. Tetraethylorthosilicate (TEOS), water, $Ce(NO_3)_3.6H_2O$, and $Tb(NO_3)_3.6H_2O$ were used as starting materials, ethanol (C_2H_5OH) as a solvent, and nitric acid (HNO_3) as a catalyst. An amount of 11.15 ml of TEOS (0.05 M) was mixed with 10 ml of ethanol and stirred for 30 minutes, after which 9 ml of water (containing 0.15 M HNO_3) was added. Stirring then continued for another 30 minutes, after which the appropriate amount of dissolved $Ce(NO_3)_3.6H_2O$ and $Tb(NO_3)_3.6H_2O$ in ethanol was added to the mixture, which was stirred for a further 4 h. The mixture was then stored in a closed container and transferred to a water bath at 50°C until a gel was formed. The gel was dried, crushed and annealed at 1000°C in flowing 4% hydrogen in argon gas for 2 hours. To control the concentration of the dopants accurately, an appropriate amount of $Ce(NO_3)_3.6H_2O$ was dissolved in 75 ml of ethanol so that each 5 ml contained the required concentration (0.5 mol%) of Ce ions. An appropriate amount of $Tb(NO_3)_3.6H_2O$ was also dissolved in 10 ml of ethanol. Of this mixture, 5 ml was added to produce the highest concentration of Tb ions. The remainder was diluted to 10 ml by adding ethanol, of which half was used to produce the next concentration of Tb ions (half of the first one). This process was repeated until the lowest concentration of Tb ions was reached.

Photoluminescence (PL) measurements were made at room temperature using a Cary Eclipse fluorescence spectrophotometer equipped with a xenon lamp. Fluorescence lifetime measurement was performed on a time-resolved fluorescence confocal microscope (MicroTime-200, PicoQuant, Germany). A single-mode pulsed diode laser (375 nm) with a pulse width of ~240 ps in full-width at half maximum and an average power less than 1 μW was used as an excitation source. Data acquisition was based on a time-correlated single-photon counting (TCSPC) technique.

3. Theoretical considerations

The non-radiative transfer of an electronic excitation from a donor to an acceptor can be represented by

$$D^* + A \rightarrow D + A^* \tag{1}$$

where D represents the ground state of the donor and A the ground state of the acceptor, and D^* and A^* represent their excited states. It has been shown that the transfer rate between the initial and final states is given by [11]

$$W_{DA} = \frac{2\pi}{\hbar} |\langle DA^*|\mathcal{H}_{DA}|D^*A\rangle|^2 \int f_D(E) f_A(E) dE \tag{2}$$

where $\langle DA^*|$ is the final state, $|D^*A\rangle$ is the initial state and $\mathcal{H}_{DA}$ is the interaction Hamiltonian. The integral represent the spectral overlap between the donor (D) emission spectrum and the acceptor (A) absorption spectrum. The normalised emission spectrum of the donor is $f_D(E)$ and the normalised absorption spectrum of the acceptor is $f_A(E)$. The mechanism for energy transfer depends on the interaction Hamiltonian.

If the wavefunctions of the donor and acceptor overlap, the quantum mechanical exchange interaction results in a transfer rate [4]

$$W_{DA} = \frac{1}{\tau_0} \exp\left(\frac{2R_0}{L}\left[1-\frac{r}{R_0}\right]\right) \tag{3}$$

where τ_0 is the donor lifetime in the absence of the acceptor, r is the distance between donor and acceptor, R_0 is the so-called critical separation distance for which energy is transferred at the same rate as which it decreases via luminescence when no acceptors are present, and L is a scaling factor corresponding to an effective Bohr radius. The corresponding decay function $\phi(t)$ after pulse excitation is given by [8]

$$\phi(t) = \exp\left[\frac{-t}{\tau_0} - \gamma^{-3}\frac{c}{c_0}\mathrm{g}\left(\frac{t}{\tau_0}e^{\gamma}\right)\right] \tag{4}$$

where the exchange constant γ is related to the scaling factor L by $\gamma = 2R_0/L$ and $g\left(\frac{t}{\tau_0}e^{\gamma}\right)$ is a function that can be evaluated numerically [8], while c is the acceptor concentration and c_0 is the critical concentration related to the critical radius by

$$c_0 = 3/(4\pi R_0^3). \tag{5}$$

For larger separation distances non-radiative energy transfer may occur via electric multipole interactions, resulting in an energy transfer rate [3]

$$W_{DA} = \frac{1}{\tau_0}\left(\frac{R_0}{r}\right)^S \tag{6}$$

where s = 6 for dipole-dipole, 8 for dipole-quadrupole and 10 for quadrupole-quadrupole interactions. The corresponding decay function is [8]

$$\phi(t) = \exp\left[\frac{-t}{\tau_0} - \Gamma\left(1 - \frac{3}{s}\right)\frac{c}{c_0}\left(\frac{t}{\tau_0}\right)^{3/s}\right]. \tag{7}$$

As a result of energy transfer, the luminescence intensity as well as the lifetime of the donor decreases. Inokuti and Hirayama [8] developed numerical methods to simulate these changes for the different interactions mechanisms. The relative emission intensity of the donor can be calculated from

$$\frac{I}{I_0} = \frac{1}{\tau_0}\int_0^{\infty}\phi(t)dt \tag{8}$$

where I is the donor emission intensity in the presence of the acceptor, and I_0 the corresponding intensity in the absence of acceptors. Similarly, the mean decay time τ_m can be calculated from

$$\tau_m = \int_0^{\infty} t\phi(t)dt \Big/ \int_0^{\infty}\phi(t)dt. \tag{9}$$

MATLAB was used to calculate the theoretical decay functions $\phi(t)$ as well as the relative emission intensities $\frac{I}{I_0}$ and the reduced mean decay times $\frac{\tau_m}{\tau_0}$ as a function of the concentration c/c_0 for the different energy transfer mechanisms in order to compare these theoretical results to experimental data.

4. Results and discussion

For luminescence measurements all the samples were excited at the Ce absorption band near 325 nm [12]. The Ce luminescence with a short lifetime (in the ns order) was

recorded with the Cary Eclipse spectrometer in fluorescence mode, while the Tb luminescence with a long lifetime (in the ms order) was recorded in the phosphorescence mode. Figure 1 presents the PL emission of Ce and Tb for the samples having Tb concentrations of 0.0100 and 0.800 mol%. The reduction of the Ce emission and increase of the Tb emission while exciting the Ce shows that energy transfer occurs. Table 1 (columns 2 and 3) lists the emission intensity (I) and the relative emission intensity ($\frac{I}{I_0}$) of the Ce donor for all the samples.

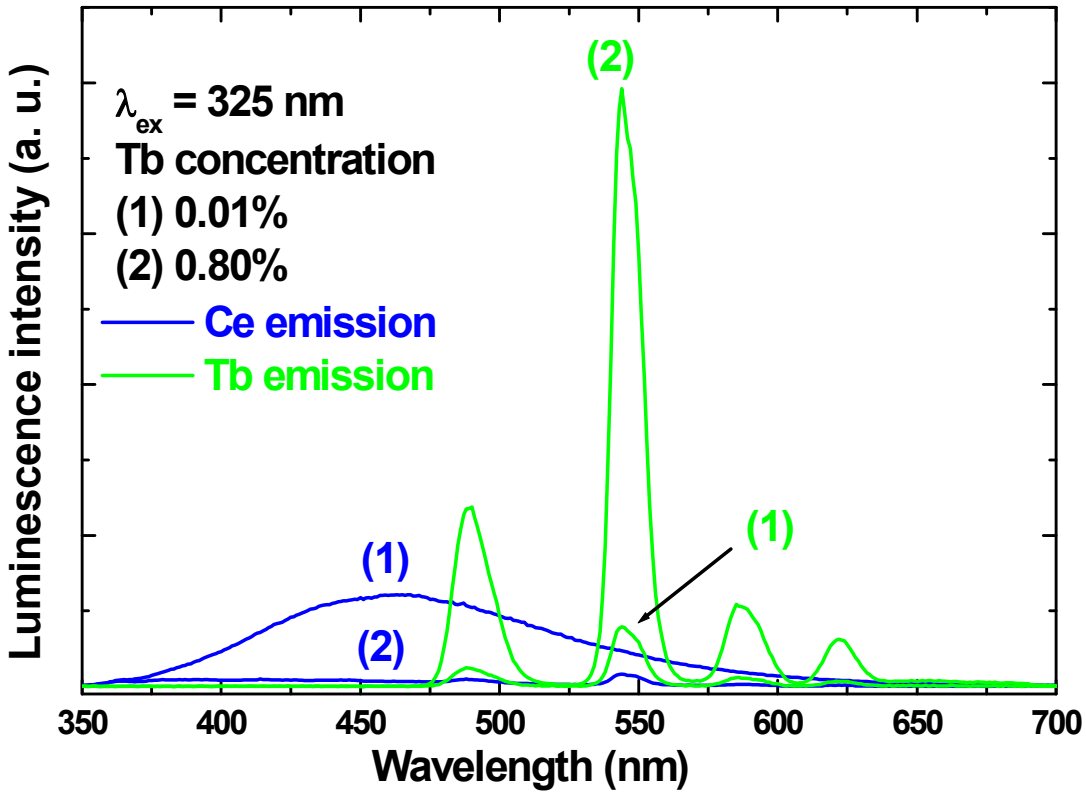

Figure 1: PL emission of (1) SiO_3:Ce(0.5%),Tb(0.01%) and (2) SiO_3:Ce (0.5%),Tb(0.80%). The Ce emission was recorded in fluorescence mode while the Tb emission was recorded in phosphorescence mode from the same samples.

Table 1: Acceptor concentration, Donor emission intensity and lifetime of the all series.

Acceptor concentration (mol%)	Donor emission intensity		Donor lifetime	
	I (a.u.)	$\frac{I}{I_0}$	τ_m (ns)	$\frac{\tau_m}{\tau_0}$
0	64.6	1	50	1
0.0100	60.2	0.932	42	0.84
0.0160	54.6	0.845	41	0.82
0.0200	52.9	0.819	42	0.84
0.0310	44.8	0.693	39	0.78
0.0400	39.7	0.615	38	0.76
0.0630	31.1	0.481	31	0.62
0.0800	22.4	0.347	22	0.44
0.125	17.3	0.268	25	0.50
0.200	11.0	0.170	17	0.34
0.250	9.18	0.142	15	0.30
0.400	6.00	0.093	16	0.32
0.500	5.84	0.090	10	0.20
0.800	3.38	0.052	8.0	0.16

The experimental values of $\frac{I}{I_0}$ were fitted to Eq. 8 using the least squares method in MATLAB. For the multipole interaction mechanisms (dipole-dipole, dipole-quadrupole and quadrupole-quadrupole) the fitting parameter is the critical concentration c_0, while for the exchange interaction mechanism the exchange constant γ is fitted in addition to

c_0, . The results are shown Figure 2 and the fit parameters are listed in Table 2. The standard deviation (σ) of the experimental data from its theoretical value was also calculated for each interaction. The best fit was obtained for the exchange model, but it should be noted that for this fit there are two fitting parameters. The best fit amongst the multipole interaction models was for the dipole-dipole interaction. For all the models the critical distance R_0 was around 20 Å. The exchange interaction requires an overlap of wavefunctions and is only realistic for very small critical distances ($R_0 \leq 10$ Å) [13]. Therefore, although the fit is good, the energy transfer cannot be attributed to the exchange interaction and the dipole-dipole interaction seems most probable mechanism.

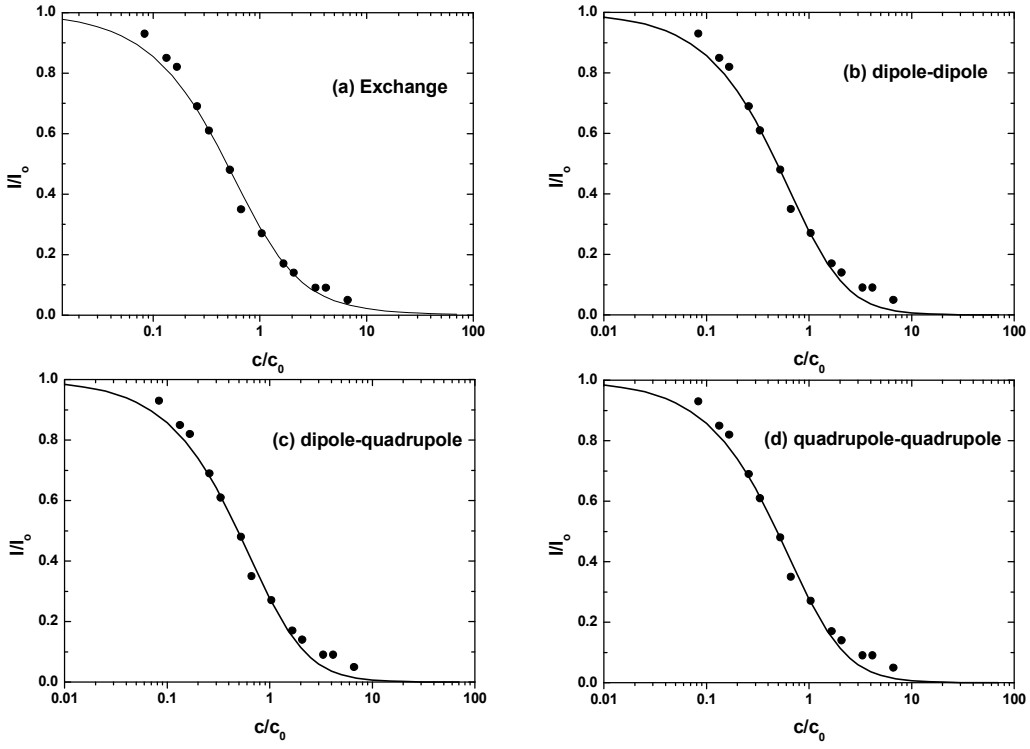

Figure 2: Experimental data of the relative emission intensity of the donor $\frac{I}{I_0}$ (circles) vs acceptor concentration $\frac{c}{c_0}$ fitted to Eq. 8 (theoretical curve) for the case of (a) exchange, (b) dipole-dipole, (c) dipole-quadrupole, and (d) quadrupole-quadrupole interaction models.

Table 2: Parameters obtained from the fitted data

Type of interaction	γ or s	c_0 (mol%)	R_0 (Å)	$\sigma(\times 10^{-2})$
Exchange	4	0.12	19. 6	2.9
Dipole-dipole	6	0.12	19.6	3.3
Dipole-quadrupole	8	0.11	20.8	3.7
Quadrupole-quadrupole	10	0.10	21.5	4.0

Lifetime decay curves of the Ce donor emission are presented in Figure 3 after excitation with a pulsed laser at 375 nm. The f-d excitation peak for Ce in silica is at 325 nm (which was used for the PL measurements), but it is very broad and extends to the wavelength used for the lifetime measurements. The Ce emission was monitored using a bandpass filter (450 ± 20 nm). Although blue emission from the $^5D_3$ levels of Tb can occur in this region, blue emission from the Tb after energy transfer from the Ce was not observed in the samples, even for the low Tb concentrations when cross-relaxation would not occur [14]. It is suggested that this is because the energy transfer from the Ce to Tb excites the $^5D_4$ level rather than the higher $^5D_3$ level.

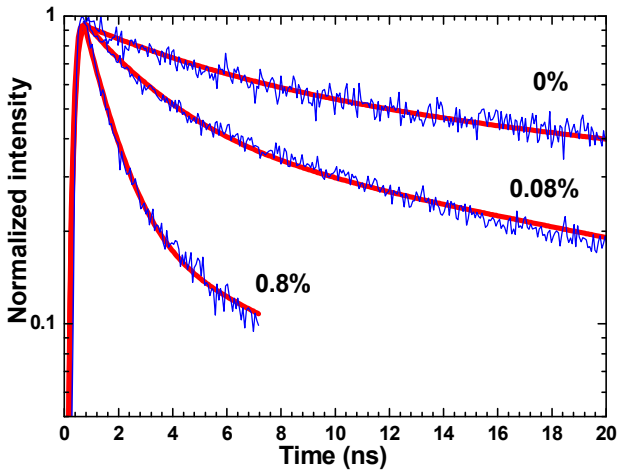

Figure 3: The decay curve of the samples SiO_3:Ce (x%) where x is 0%, 0.08% and 0.8%. The blue curve is the measured data and the red points are the convolution of the fitted data.

Although the decay curve of the Ce singly doped sample (Figure 3) is not simple exponential, a dramatic shortening of the lifetime was measured for samples co-doped with Tb, as expected for non-radiative energy transfer. Possible reasons for the deviation from simple exponential decay for the Ce singly doped sample are that the Ce occupies more than one site in the amorphous host, or that there is some contribution to the emission from defects in the silica. The measured decay data for a period until the curve had decayed to 10% of its maximum value was fit to a multiexponential function (two exponentials were found to be adequate) that had been convoluted with the instrument response function, using least squares fitting in MATLAB. The fitted multiexponential functions were then used to compute the mean lifetimes, which are given in Table 1 (column 4). The mean lifetime of the Ce singly doped sample was 50 ns and this value was used for τ_0.

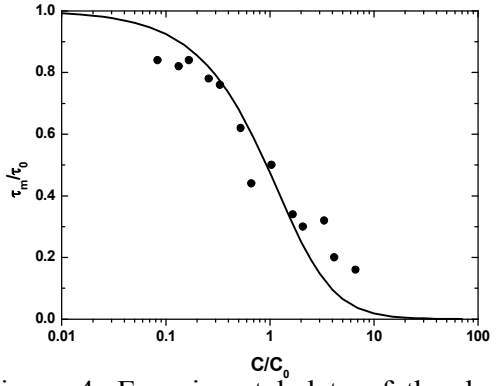

Figure 4: Experimental data of the decay lifetime τ_m/τ_0 of the donor (circles) vs acceptor concentration c/c_0 fitted to Eq. 9 (the dipole-dipole theoretical curve)

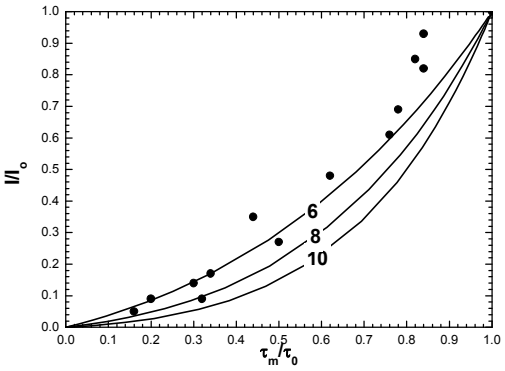

Figure 5: The relative emission intensity I/I_0 vs the decay lifetime τ_m/τ_0 of the donor (circles) compared to the multipole interaction theoretical curves

The experimental values of τ_m/τ_0 were fit to Eq. 9 for the dipole-dipole interaction mechanism and the result in shown in Figure 4. Although the experimental decay data shows some scatter, the critical concentration for the fit was 0.12 mol% which corresponds exactly to what was found from the relative intensity data (Table 2). Figure 5 shows the plot of the experimental values of I/I_0 versus τ_m/τ_0 compared to the theoretical curves for the different types of multipole interaction, and from this data one can also see that the dipole-dipole interaction mechanism is the most probably mechanism for energy transfer between Ce and Tb in silica.

5. Conclusion

The mechanism of the energy transfer from Ce to Tb in sol-gel silica was investigated using the Inokuti and Hirayama models. The relative emission intensity of the donor ($\frac{I}{I_0}$) as a function of the acceptor concentration was found to fit well to the theoretical models associated with the exchange interaction and the dipole-dipole interaction, with the critical distance R_0 around 20 Å for both models. The obtained value of R_0 leads us to exclude the exchange interaction model, which requires shorter distances ($R_0 \leq 10$ Å). The decay lifetime of all the samples in the series was not a single exponential, even for the single Ce doped sample (which is not expected). This complex behaviour in decay lifetime caused inadequate fitting of the experimental data to the theoretical curve.

References

[1] Kroon RE, Seed Ahmed HAA and Gusowski MA 2011 *Proc.* in Proceedings of SAIP2011, the 56th Annual Conference of the South African Institute of Physics, edited by I. Basson and A.E. Botha (University of South Africa, Pretoria, 2011), p. 162. ISBN: 978-1-86888-688-3. Available online at http:\\www.saip.org.za.

[2] Forster Th. 1948 *Ann. Physik* **2** 55

[3] Dexter DL 1953 *J. Chem. Phys.* **21** 836

[4] Walter JCG 1971 *Phys. Rev.* B **4** 648

[5] Lenth W and Huber G 1981 *Phys. Rev.* B **23** 3877

[6] Bojarski C, Grabowska J, Kulak L and Kusba J 1991 *J. Fluoresc.* **1** 183

[7] Morita M, Buddhudu S, Rau D and Murakami S 2004 *Struct. Bonding* **107** 115

[8] Inokuti M and Hirayama F 1965 *J. Chem. Phys.* **43** 1978

[9] Nakazawa E and Shionoya S 1967 *J. Chem. Phys.* **47** 3211

[10] Mares J, Jacquier B, Pedrini C and Boulon G 1987 *Revue Phys. Appl.* **22** 145

[11] Vasquez SO 1999 *Physical Rev. B* **60** 8575

[12] Xu GQ, Zheng ZX, Tang WM and Wu YC 2007 *J. Lumin.* **124** 151

[13] Sensitised photoluminescence and Förster-Dexter theory [online]. Available from http://members.multimania.co.uk/lucarz/Projects/ErSRSO/Chapter3.pdf [Accessed 30 June 2012]

[14] Blasse G 1983 *Rev. Inorg. Chem.* **15** 319

Chapter XII

Luminescence from Ce and Tb in LaF_3 and the energy transfer mechanism in Ce,Tb co-doped LaF_3

1. Introduction

Developing the efficiency of luminescent materials has attracted much interest in the last five decades due to their wide application in modern technologies. One way to enhance the luminescence efficiency is through energy transfer between a donor and an acceptor. Among lanthanide ions, Ce^{3+} is an excellent donor candidate due to its allowed f-d absorption and its broad emission band which can overlap an acceptor absorption band. The bright green emission of Tb^{3+} makes this ion a popular acceptor of the lanthanide group. Lanthanum fluoride (LaF_3) is considered to be an ideal host material due to its superior thermal and environmental stability, as well as its low vibrational energy (~350 cm^{-1}) which minimizes non-radiative phonon-assisted quenching of the excited states of the dopant ions [1]. During the past decade there have been a significant number of reports focussing on nanoparticles with the specific composition $La_{0.4}F_3$: $Ce_{0.45}$,$Tb_{0.15}$ [2-8]. The composition $La_{0.8}F_3$:$Ce_{0.15}Tb_{0.05}$ has also been considered [9], while recently the properties of lanthanum fluoride nanocrystals produced using the hydrothermal method with varying amounts of Ce and Tb have been reported [1]. The quantum efficiency of these phosphors has been an important consideration, and although the energy transfer from Ce to Tb is evident from the previous reports, the mechanism for the energy transfer has not been examined. A recent report [1] states that the critical transfer distance for energy transfer from Ce to Tb has been estimated at ~ 0.5 nm in LaF_3, but this calculation was actually made for $Ce_{0.85}Tb_{0.15}F_3$ (containing no La) and assumes that energy transfer occurs via the dipole-dipole interaction mechanism [10]. In this chapter, the mechanism responsible for the energy transfer between Ce and Tb in LaF_3 was investigated by fitting both the luminescence intensity and the lifetime of the donor (Ce) as a function of the acceptor (Tb) concentration to the Inokuti and Hirayama theoretical models [11].

2. Experimental

LaF_3 pure host, LaF_3:Ce, LaF_3:Tb as well as co-doped LaF_3:Ce,Tb phosphors were synthesized by the hydrothermal method. $La(NO_3)_3.6H_2O$ and NaF were used as starting materials and $Ce(NO_3)_3.6H_2O$ and $Tb(NO_3)_3.6H_2O$ were added for doping. Cetyltrimethylammonium bromide $C_{19}H_{42}BrN$ (CTAB) served as a surfactant to control the particle size. Each prepared sample contained 5 mmol of the lanthanide ions (including dopants), 15 mmol of NaF and 1 mmol of CTAB. The nitrates, dissolved in 30 ml of water, were added to the CTAB in 10 ml water. After stirring for 20 min, NaF dissolved in 10 ml of water was added drop by drop. After further stirring for 40 min, the mixture was transferred into a 125 ml autoclave lined with teflon and heated at 150°C for 12 h. The product was collected by centrifugation and washed first with water, and then with ethanol, each three times. The powder was finally dried in an oven at 80°C. By repeated dilution of a terbium nitrate solution, a series of LaF_3:Ce(1 mol%),Tb(x mol%) where x = 20, 10, 5, 2, 1, 0.5, 0.2, 0.1, 0.05 was prepared for the analysis of the energy transfer mechanism. The structure of the prepared samples was characterised by X-ray diffraction (XRD) using a Bruker D8 diffractometer. Auger spectra and scanning electron microscopy (SEM) images were collected with a PHI 700 Scanning Auger Nanoprobe. Photoluminescence (PL) spectra were obtained with a Cary Eclipse fluorescence spectrophotometer, using the fluorescence mode for measuring the Ce emission and the phosphorescence mode for measuring the Tb emission. The luminescence decay curves were recorded at the SUPERLUMI station at HASYLAB, DESY using synchrotron radiation. All reported measurements were made at room temperature.

3. Results and discussion

Figure 1 shows the XRD patterns of undoped and doped LaF_3, together with the standard data for LaF_3 from JCPDS card 32-0483. The patterns for samples doped with 5 mol% of either Ce or Tb have almost no difference from the pure host, showing that the Ce and Tb ions were incorporated successfully and were well dispersed in the LaF_3 lattice. The heavily doped LaF_3:Ce(1%),Tb(20%) sample shows a slight shift in the diffraction peaks toward greater angles, implying that the lattice parameter has decreased, which is

reasonable in terms of the smaller Tb ionic radius (0.0923 nm) compared to the La ions (0.1061 nm) that are substituted [6].

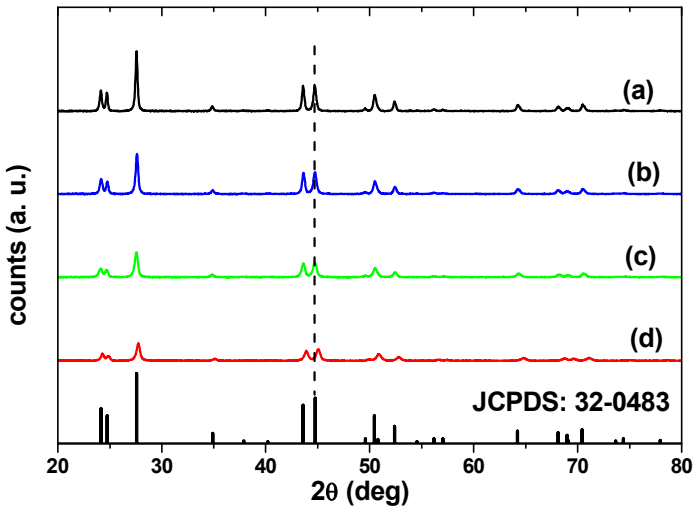

Figure 1: XRD pattern of (a) LaF_3, (b) LaF_3:Ce(5%), (c) LaF_3:Tb(5%), and (d) LaF_3:Ce(1%)Tb(20%). The bottom vertical lines are the standard data of LaF_3 from JCPDS card 32-0483.

The particle size was estimated from the Scherrer [12] equation

$$\tau = \frac{K\lambda}{\beta \cos\theta} \tag{1}$$

where K is the shape factor (0.9), λ is the wavelength and β is the FWHM of the x-ray peak at the Bragg angle θ (corrected for the instrument response). The average particle size of the undoped LaF_3 nanoparticles was 36 nm. For the doped samples the x-ray peaks were slightly wider than for the undoped sample, but this can be explained by impurity broadening instead of a decrease in particle size.

Figure 2 presents a SEM image and Auger profile of pure LaF_3. Charging on the insulating samples limits the resolution of the images, so the particle shape is not clear, but it can be seen that that the particle size is less than 50 nm which is in agreement with the estimate from the XRD data. The Auger peaks at 83, 528, 634 and 732 eV are associated with the La while the peak at 659 eV corresponds to F. The peak at 273 eV is associated with C, and this contamination is attributed to adventitious hydrocarbons which are known to be always present.

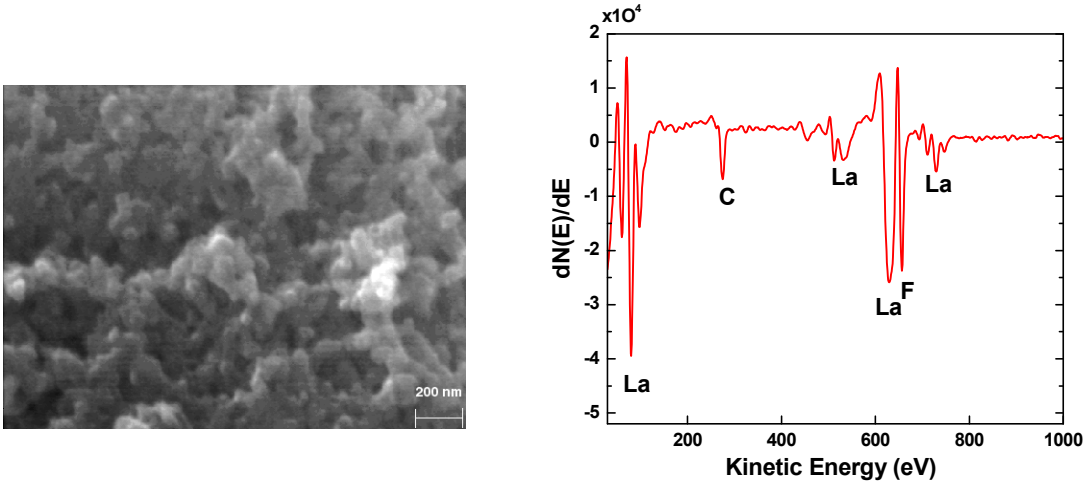

(a) (b)

Figure 2: (a) SEM image and (b) Auger spectrum of pure LaF_3

Figure 3 shows the PL excitation and emission spectra for the LaF_3:Ce(1%). The excitation spectrum has a broad peak with a maximum at 247 nm corresponding to the 4f-5d absorption band of the Ce^{3+} ions. The broad emission spectrum exhibits two peaks centred at 287 and 301 nm which are attributed to the transitions from the lowest 5d excited state to the 4f ($^2F_{7/2}$ and $^2F_{5/2}$) ground state. Both the excitation and emission spectra are in agreement with reported data [13].

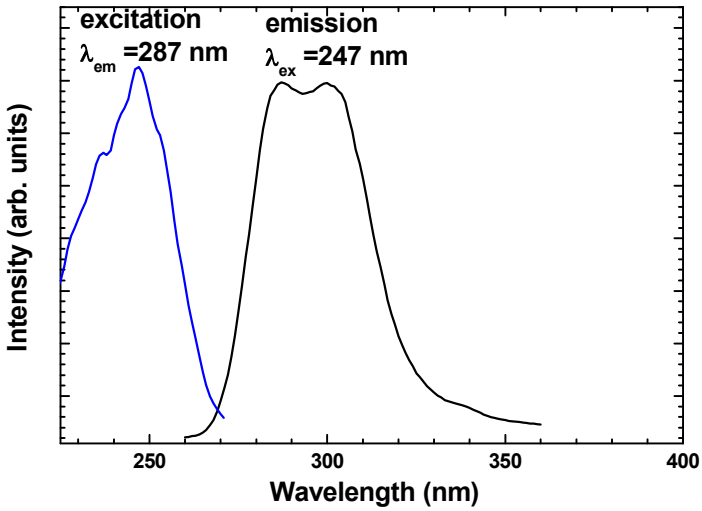

Figure 3: Excitation and emission for the LaF_3:Ce(1%)

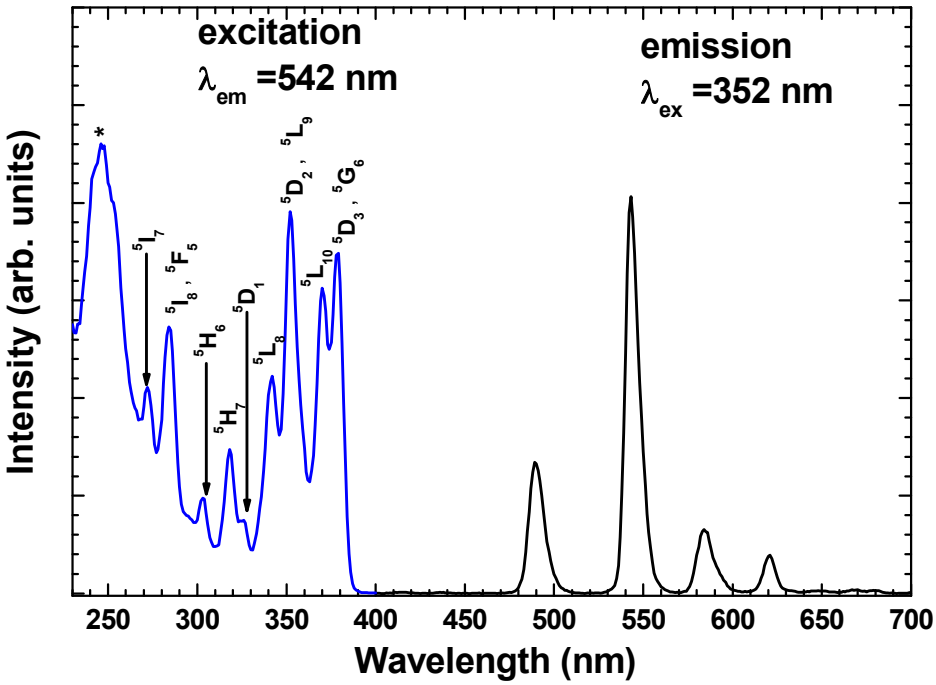

Figure 4: Excitation and emission spectra for LaF_3:Tb(5%). Label for f-f transition are from $^7F_6$ ground state. The absorption peak marked with (*) is attributed to small amounts of Ce impurity.

Excitation and emission spectra for LaF_3:Tb(5%) are shown in Figure 4. The excitation spectrum was recorded using the 542 nm green emission of Tb^{3+} ions. Nine absorption bands are found to correspond to f-f transitions of Tb^{3+}, from the $^7F_6$ ground state to: $^5I_7$ at 272 nm; $^5I_8$,$^5F_5$ at 284 nm; $^5H_6$ at 303 nm; $^5H_7$ at 318 nm; $^5D_1$ at 326 nm; $^5L_8$ at 342nm; $^5D_2$,$^5L_9$ at 352 nm; $^5L_{10}$ at 370 nm and $^5D_3$,$^5G_6$ at 379 nm [14]. Although Wang *et al.* [1] state that 4f-5d absorption bands of Tb^{3+} ions in LaF_3 occur from 250–280 nm, the lowest energy f-d absorption actually occurs near 200 nm [15]. The absorption band at 247 nm does not appear to be due to f-f or f-d absorption of Tb^{3+} and is most likely caused by very small amounts of Ce^{3+} impurity (the wavelength matches the f-d absorption of Ce in Figure 3) which could come from the porous teflon liner used for sample preparation with other samples containing Ce. The emission spectrum obtained from the Tb doped samples by exciting with 352 nm showed the characteristic green emission bands attributed to the $^5D_4$-^7F_J transitions (J=6,5,4,3) of Tb^{3+}, with the dominant green band at 542 nm.

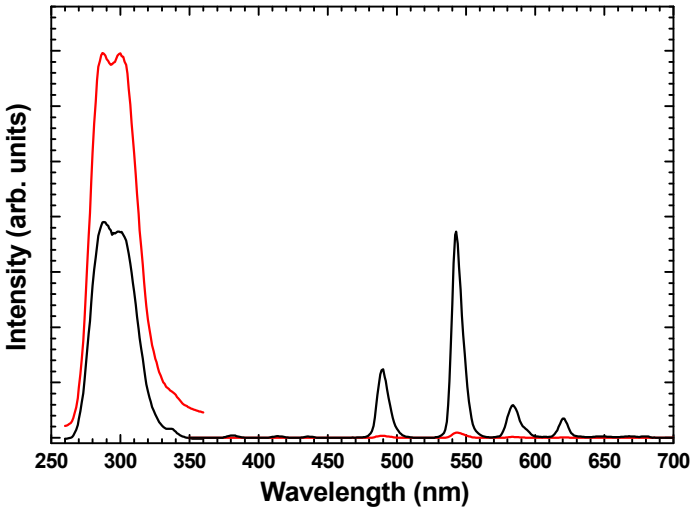

Figure 5: PL spectrum of the LaF_3:Ce(1%),Tb(5%) sample excited with 247 nm (black) comparing with the PL of LaF_3:Ce(1%) and LaF_3:Tb(5%) samples (red)

Figure 5 shows the PL emission spectrum of the LaF_3:Ce(1%),Tb(5%) co-doped sample excited at 247 nm, compared to the emission spectra for the singly doped samples. The Ce emission in the co-doped sample was quenched and an enhancement of the Tb emission was observed. This can be attributed to energy transfer from the Ce^{3+} ions to Tb^{3+} ions. Figure 6 shows the overlap of the emission spectrum of LaF_3:Ce(1%) and the excitation spectrum of LaF_3:Tb(5%). The Ce emission overlaps several of the Tb f-f excitation bands, which is the essential condition for energy transfer to occur (without the need for phonons). The Tb excitation spectrum of the co-doped sample monitored at 542 nm (see Figure 6) showed a prominent peak at 247 nm, corresponding to Ce^{3+} f-d absorption, and relatively weak peaks associated with the Tb f-f excitation bands

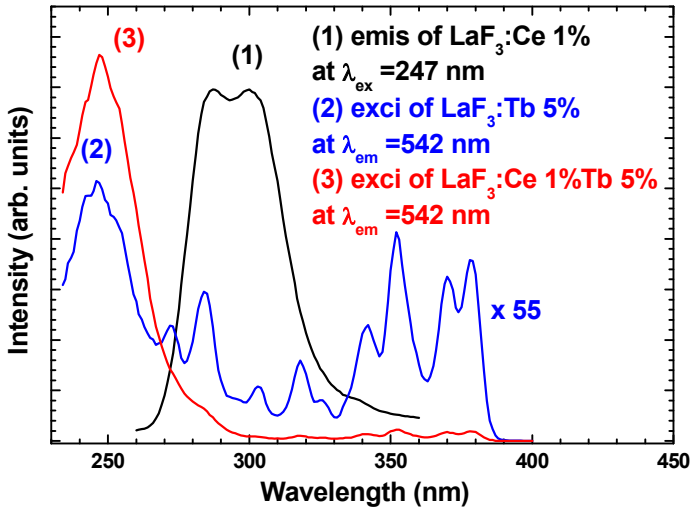

Figure 6: The emission spectrum of LaF_3:Ce(1%) , the excitation spectrum of LaF_3:Tb(5%), and the excitation spectrum of LaF_3:Ce(1%),Tb(5%)

To investigate the influence of the Ce concentration on the emission intensity from Tb in the co-doped samples, the concentration of Tb^{3+} ions was kept constant at 5 mol% and the concentration of Ce^{3+} ions was varied from 0 up to 5 mol%. Figure 7 shows the relative intensity of Tb emission associated with the $^5D_4$-$^7F_5$ transition near 542 nm as a function of Ce concentration, normalized with respect to the sample containing no Ce, i.e. the Tb single doped sample. It was found that the Tb emission increased as the Ce concentration increased up to 5 mol%. Although the concentration of Ce corresponding to a maximum was not reached, the rate of increase became relatively low. It was decided to study the transfer mechanism using a fixed Ce concentration of 1 mol%, as a compromise between obtaining strong Tb emission through energy transfer, but not introducing more Ce than was necessary into the host. This also avoids possible interaction between Ce-Ce ions which may occur at high concentration, although it has been reported that practically no concentration quenching occurs in $La_{1-x}Ce_xF_3$, implying that energy migration between Ce ions is not significant, even for very high Ce concentrations [16].

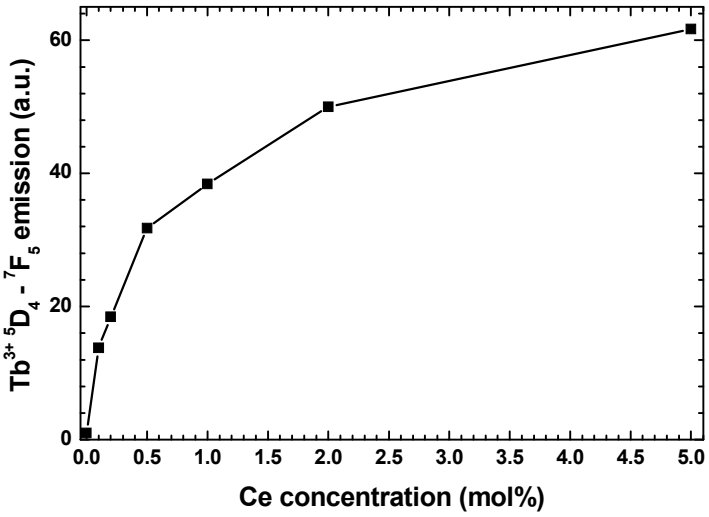

Figure 7: The relative intensity of Tb emission associated with the $^5D_4$-$^7F_5$ transition as a function of Ce concentration

The luminescence intensity and decay lifetime of the Ce donor as a function of the Tb acceptor concentration in co-doped LaF_3 samples were studied to determine the mechanism of the energy transfer from the Ce to the Tb ions. Inokuti and Hirayama [11] illustrated how the values of I/I_0 where I_0 is the donor emission intensity in the absence of the acceptor and I is the corresponding intensity in the presence of an acceptor, as well as τ_m/τ_0 where τ_m is the mean decay time and τ_0 is the lifetime of the donor when the acceptor is absent, depend on the acceptor concentration for different types of multipole as well as the exchange mechanism of energy transfer. . Inokuti and Hirayama [11] calculated the relative emission intensity of the donor as

$$\frac{\mathrm{I}}{\mathrm{I}_0} = \frac{1}{\tau_0}\int_0^\infty \phi(\mathrm{t})\mathrm{dt} \tag{2}$$

and the mean decay time τ_m as

$$\tau_m = \int_0^\infty t\phi(t)dt \Big/ \int_0^\infty \phi(t)dt \tag{3}$$

where $\phi(t)$ is the decay function after pulse excitation .

For multipole interactions the decay function is given by

$$\phi(t) = \exp\left[\frac{-t}{\tau_0} - \Gamma\left(1 - \frac{3}{s}\right)\frac{c}{c_0}\left(\frac{t}{\tau_0}\right)^{3/s}\right] \tag{4}$$

where s = 6, 8 or 10 for dipole-dipole, dipole-quadrupole and quadrupole-quadrupole interactions, c is the acceptor concentration and c_0 is some critical concentration at which the energy transfer rate from the donor equals its emission rate. The critical concentration can be related to a critical distance using $c_0 = 3/(4\pi R_0^3)$. For the exchange interaction the decay function is given by

$$\phi(t) = \exp\left[\frac{-t}{\tau_0} - \gamma^{-3}\frac{c}{c_0}\mathrm{g}\left(\frac{t}{\tau_0}e^{\gamma}\right)\right] \quad (5)$$

where $\mathrm{g}\left(\frac{t}{\tau_0}e^{\gamma}\right)$ is a function that can be evaluated numerically [11]. The exchange constant γ is related to an effective Bohr interaction radius L between the ions by

$$\gamma = 2R_0/L. \quad (6)$$

Values of I/I_0 for a fixed Ce donor concentration of 1 mol% and a range of Tb acceptor concentrations were measured with the Cary-Eclipse fluorescence spectrophotometer and the results are given in Figure 8 and Table 1.

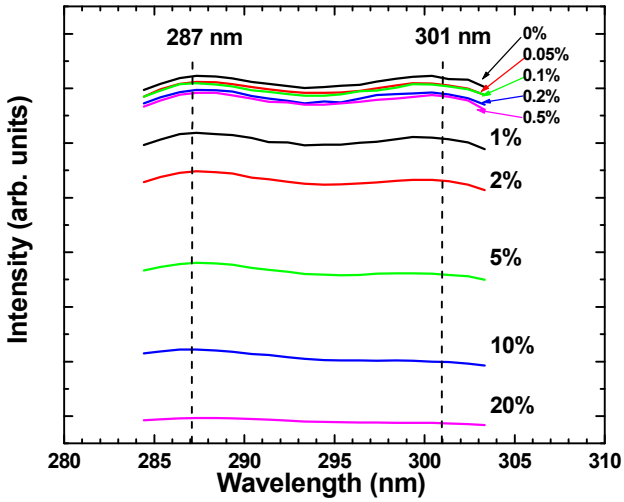

Figure 8: The intensity of Ce emission for a range (0%-20%) of Tb concentration

The quantum efficiency of the energy transfer is given by[11]

$$\eta_T = 1 - I/I_0 \quad (7)$$

and a value of 87% was obtained for LaF_3:Ce(1%),Tb(20%).

The Ce donor lifetime curves were measured using synchrotron radiation at SUPERLUMI using photon counting with a photomultiplier tube detector, with an excitation wavelength of 247 nm. The time between bunches limited the measuring period to about 70 ns. The experimental curves were fitted (using the linear least squares routine in MATLAB) to multi-exponential functions (3 exponentials were found to be adequate) which were convoluted with the stray light signal measured on the system, and the fitted multi-exponential curves were used to calculate the mean decay times τ_m. The decay curve for singly doped LaF:Ce 1 mol% was processed in the same way as for the co-doped samples, but with only a single-exponential function, and the lifetime was found to be 29 ns for the 287 nm emission and 31 ns for the 301 nm emission. These values are similar to the lifetime reported for smaller Ce-doped LaF_3 nanoparticles coated with undoped LaF_3 shells [17]. The decay time was slightly longer for the longer wavelength emission, as has been reported for Ce doped $NaCaPO_4$ [18]. Figure 9 presents several of the processed lifetime decay curves. The blue curve is the measured data and the red points are the convolution of the fitted data.

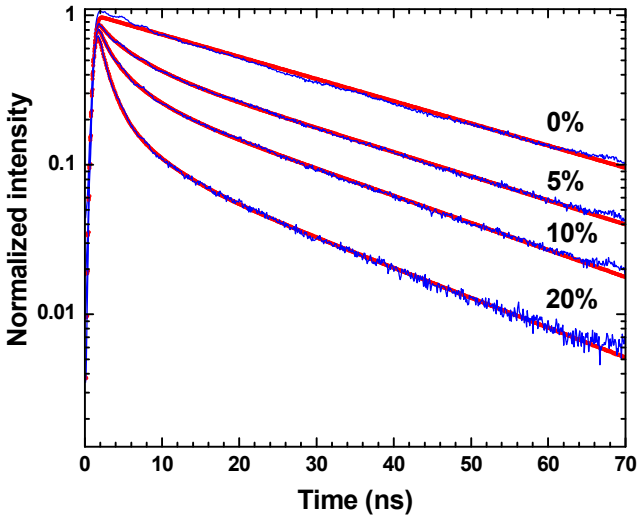

Figure 9: The processed lifetime decay curves of the samples LaF_3:Ce(1%),Tb(x%) where x is 0%, 5%, 10%, and 20%. The blue curve is the measured data and the red points are the convolution of the fitted data.

Table 1: Luminescence intensity and lifetime for the LaF_3:Ce,Tb

Acceptor concentration (mol%)	peak at 287 nm			peak at 301 nm		
	$\frac{I}{I_0}$	τ_m (ns)	$\frac{\tau_m}{\tau_0}$	$\frac{I}{I_0}$	τ_m (ns)	$\frac{\tau_m}{\tau_0}$
0	1	29.23	1	1	30.94	1
0.0500	0.984	28.63	0.979	0.981	30.37	0.982
0.100	0.981	28.58	0.978	0.978	30.32	0.980
0.200	0.964	28.50	0.975	0.958	30.17	0.975
0.500	0.956	28.25	0.966	0.951	29.93	0.967
1.00	0.855	27.87	0.954	0.844	29.51	0.954
2.00	0.758	27.62	0.945	0.737	29.17	0.943
5.00	0.526	24.24	0.829	0.500	25.97	0.839
10.0	0.306	19.79	0.677	0.277	20.22	0.653
20.0	0.134	14.09	0.482	0.121	14.63	0.473

Figure 10 (a) shows the experimental data I/I_0 and τ_m/τ_0 associated with the peak at 287 nm (closed shape) and the peak at 301 nm (open shape) plotted against one another and compared to the theoretical curves expected for different types of multipole interactions, which were calculated using the method of Inokuti and Hirayama [11]. The results match what one may expect if the energy transfer occurs due to quadrupole-quadrupole interaction, and is not consistent with either dipole-dipole or dipole-quadrupole interactions. To determine the critical concentration c_0, least squares fits were made for the quadrupole-quadrupole interaction of I/I_0 against c/c_0 and τ_m/τ_0 against c/c_0 with c_0 as the fit parameter, giving values of 8.58 and 9.77 mol% respectively. These were averaged and the result was converted to a volume concentration (using a molar volume of 33 cm^3/mol for LaF_3), and used to calculate the critical distance R_0 of 0.52 nm. Despite the fact that this value is obtained on the basis of quadrupole-quadrupole interaction, its value is almost the same as that reported before using a calculation based on the dipole-dipole interaction [1,10].

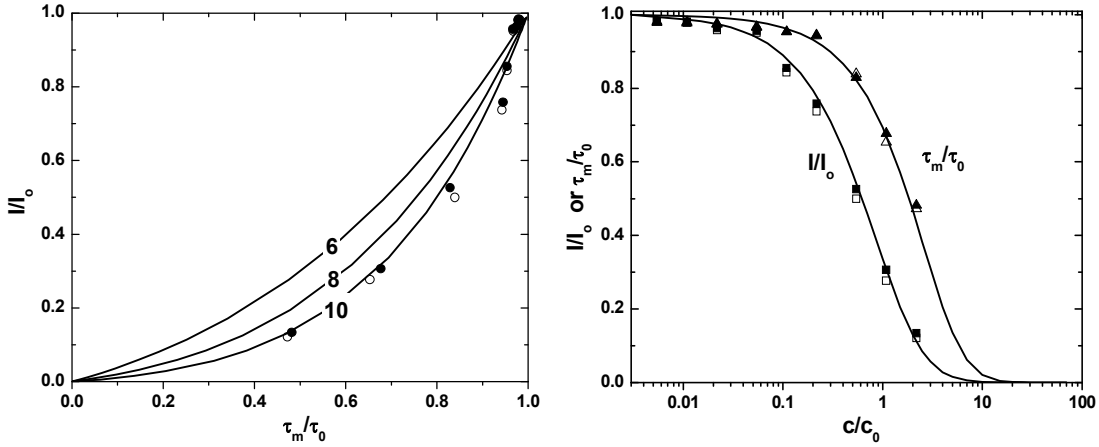

(a) (b)

Figure 10: (a) Experimental data of $\frac{I}{I_0}$ vs $\frac{\tau_m}{\tau_0}$ (closed and open circle) fitted to the theoretical curves (solid lines) of dipole-dipole (s=6), dipole-quadrupole (s=8), and quadrupole-quadrupole (s=10) interaction. (b) Experimental data of $\frac{I}{I_0}$ (closed and open square) vs $\frac{c}{c_0}$ and $\frac{\tau_m}{\tau_0}$ (closed and open triangle) vs $\frac{c}{c_0}$ fitted Eq. (2) and Eq. (3) (theoretical curves) of quadrupole-quadrupole interaction. Note that closed and open shape correspond to the peak at 287 nm and 301 nm respectively.

The experimental data was also fitted to the exchange interaction model for energy transfer. For this model, in addition to c_0, the exchange constant γ is also a parameter. The experimental data of I/I_0 and τ_m/τ_0 were plotted against one another and compared to the theoretical curves of several values of γ as computed using the method of Inokuti and Hirayama [11]. The experimental data corresponds well to the exchange interaction for γ =11.6 (see Figure 11(a)). This value for γ was fixed and least squares fits of I/I_0 against c/c_0 and τ_m/τ_0 against c/c_0 with c_0 as the fit parameter were made for exchange model in order to determine the critical concentration c_0, giving values of 8.02 and 7.97 mol% respectively.

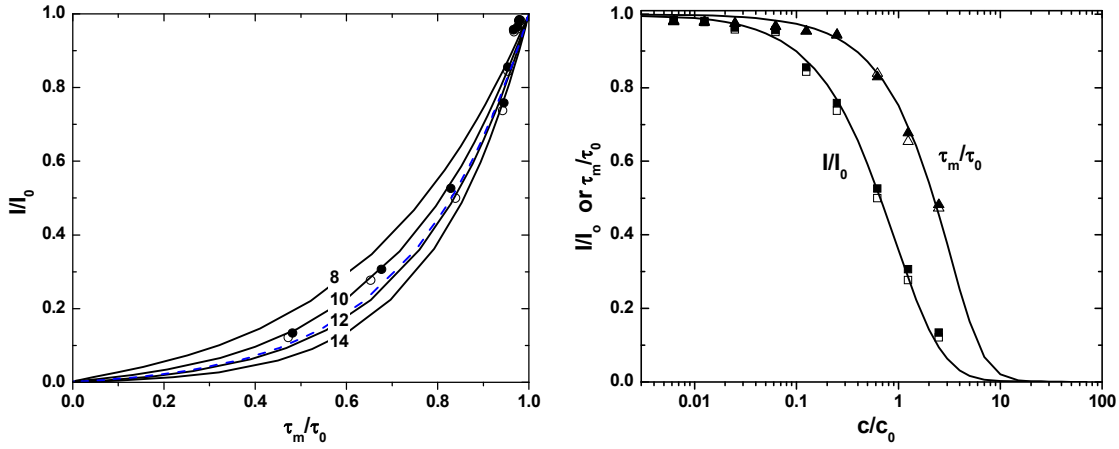

Figure 11: (a) Experimental data of $\frac{I}{I_0}$ vs $\frac{\tau_m}{\tau_0}$ (closed and open circle) fitted to the theoretical curves (solid lines) of exchange interaction (γ = 8, 10, 12 and 14). The blue dashed line gives the best fit (γ = 11.6). (b) Experimental data of $\frac{I}{I_0}$ (closed and open square) vs $\frac{c}{c_0}$ and $\frac{\tau_m}{\tau_0}$ (closed and open triangle) vs $\frac{c}{c_0}$ fitted to Eq. (2) and Eq. (3) (theoretical curves) of exchange interaction. Note that closed and open shape correspond to the peak at 287 nm and 301 nm respectively.

The average critical concentration was used to calculate the critical distance R_0 of 0.55 nm, which is similar to that obtained for the quadrupole-quadrupole interactions. As pointed out by Nakazawa and Shionoya [19], it can be difficult to distinguish between the higher order multipole interactions and the exchange interaction by analysing the luminescence intensity and lifetime of the donor emission. To check if the exchange mechanism is feasible, the effective average Bohr radius L should be similar to the ionic radii of the interaction ions, i.e. 0.1 nm for the lanthanides. In the present case the values of R_0 and γ give an effective average Bohr radius L = 0.095 nm, which means the exchange interaction mechanism can contribute the energy transfer between Ce and Tb, although quadrupole-quadrupole interaction cannot be eliminated.

Using a similar method to that in this study, Nakazawa and Shionoya [19] found that energy transfer between unlike lanthanide ions in calcium metaphosphate glass was governed by dipole-quadrupole interactions. However, cerium was not one of the dopants considered. Wang *et al.* [20] found the dipole-dipole interaction was responsible for energy transfer from Ce to Tb in $CaAl_2SiO_6$. To our knowledge, energy transfer from

Ce to Tb has not been attributed to quadrupole-quadrupole interaction before. This mechanism has been reported for energy transfer from Eu to Pr in $K_5Li_2GdF_{10}$, although the exchange mechanism was not considered in that study [21]. In contrast to a recent report on Ce,Tb co-doped $LaPO_4$ nanoparticles [22] in which energy transfer is suggested to not affect the decay kinetics of the Ce emission, in this study changes in the Ce decay curves could be observed and correlated to energy transfer from Ce to Tb.

4. Conclusion

Ce and Tb have been successfully incorporated singly, as well as together, in LaF_3 nanoparticles via the hydrothermal method. The crystal structure of LaF_3 remained unchanged after being doped with Ce^{3+} and Tb^{3+} ions, with a slight decrease in the lattice parameter in the samples having a heavy dopant concentration. The estimated particle size was 36 nm. The excitation and emission spectra of the single doped samples are in a good agreement with the reported values. Energy transfer from Ce to Tb was achieved in the co-doped samples with a quantum efficiency for energy transfer around 87% for the LaF_3:Ce(1%),Tb(20%) sample. The data associated with the luminescence intensity and lifetime of the donor as a function of the acceptor concentration fitted well to the Inokuti and Hirayama nonradiative energy transfer models corresponding to the quadrupole-quadrupole mechanism and the exchange interaction mechanism. Due to the short effective average Bohr radius *L* calculated from the obtained fitted parameters, the exchange interaction could not be excluded and it may contribute to the energy transfer together with quadrupole-quadrupole interaction.

References

[1] Wang Q, You Y, Ludescher RD and Ju Y 2010 *J. Lumin.* **130** 1076

[2] Stouwdam JW, Hebbink GA, Huskens J and van Veggel FCJM 2003 *Chem. Mater.* **15** 4604

[3] Stouwdam JW and van Veggel FCJM 2004 *Langmuir* **20** 11763

[4] Wang F, Zhang Y, Fan X and Wang M 2006 *J. Mater. Chem.* **16** 1031

[5] Zhu X, Zhang Q, Li Y and Wang H 2008 *J. Mater. Chem.* **18** 5060

[6] Liu Y, Chen W, Wang S, Joly AG, Westcott S and Woo BK 2008 *J. Appl. Phys.* **103** 063105

[7] Xie M-Y, Yu L, He H and Yu X-F 2009 *J. Solid State Chem.* **182** (2009) 597

[8] He H Xie MY Ding Y and Yu XT 2009 *Appl. Surface Scie.* **255** 4623

[9] Zhang T, Guo H and Qiao Y 2009 *J. Lumin.***129** 861

[10] Wang ZL, Quan ZW, Jia PY, Lin CK, Luo Y, Chen Y, Fang J, Zhou W, O'Connor CJ and Lin, J 2006 *Chem Mater.* **18** 2030

[11] Inokuti M and Hirayama F 1965 *J. Chem. Phys.* **43** 1978

[12] Scherrer, P 1918 *Göttinger Nachrichten Math. Phys.* **2** 98

[13] Pedrini C, Moine B, Gacon JC and Jacquier B 1992 *J. Phys. Condens. Matter* **4** 5461

[14] Carnall WT, Crosswhite H and Crosswhite HM 1978 Argonne National Laboratory Report ANL-78-XX-95

[15] Dorenbos P 2003 *J. Phys. Condens. Matter* **15** 6249

[16] Blasse G and Bril A 1969 *J. Chem. Phys* **51** 3252

[17] Jacobsohn LG, Toncelli A, Sprinkle KB, Kucera CJ and Ballato J 2012 *J. Appl. Phys.* **111** 074315

[18] Wang Y Zhang J Hou D Liang H Dorenbos P Sun S and Tao Y 2012 *Opt. Mater.* **34** 1214

[19] Nakazawa E and Shionoya S 1967 *J. Chem. Phys.* **47** 3211

[20] Wang B, Sun L and Ju H 2010 *Solid State Comm.* **150** 1460

[21] Solarz P and Romanowski WR 2007 *Radiat. Meas.* **42** 759

[22] Pankratov V, Popov AI, Chernov SA, Zharkouskaya A and Feldmann C 2010 *Phys. Stat. Sol.* B **247** 2252

Chapter XIII

Conclusion

A wide variety of lanthanide ions were incorporated successfully in silica using the sol-gel method. Luminescence measurements produced by photons (photoluminescence or PL) and electrons (cathodoluminescence or CL) were made and compared for all the prepared samples. Samples doped with Tb and Eu showed bright emission under both types of excitation. Weak PL and CL emission from the samples doped with Sm and Dy were very similar. Samples doped with Pr exhibited weak PL and CL emission while sample doped with Tm showed only CL emission. No emission was found for samples doped with Nd, Gd, Ho, Er and Yb for either type of excitation. Interesting differences in luminescence from the samples doped with Tb and Ce were observed depending on the type of excitation. The cathodoluminescence can cause emission which was not produced by the UV irradiation, and this was attributed to the additional luminescence of ions in the 4+ valence state that captured electrons and then emitted in a similar fashion as ions in the 3+ state. For Ce and Pr doped samples photoluminescence emission could also be induced by annealing the samples in a reducing atmosphere, with very bright emission from the Ce but only poor results from the Pr.

Tb with 0.1 mole% and 1 mole% were embedded in silica by the sol-gel method. The $^5D_3 \rightarrow ^7F_J$ blue emission observed in the 0.1 mole% sample excited with different UV sources (xenon lamp, laser and synchrotron radiation) was found to have been quenched through cross-relaxation in the sample containing 1 mole%. However, the CL measurement showed the $^5D_3 \rightarrow ^7F_J$ blue emission even for 1 mole% sample. A simple calculation of the quantum efficiency for the 325 nm laser UV source used for PL compared to that for CL indicated that the presence of the $^5D_3 \rightarrow ^7F_J$ blue emission is not due to the high quantum efficiency of the CL, but to the nature of the type of the excitation (i.e. electrons versus photons). During electron bombardment Tb^{4+} ions can be convert into an excited $(Tb^{3+})^*$ state, which do not experience concentration quenching, possibly because Tb^{4+} ions have a lower concentration on a different site compared to the

Tb^{3+} ions. It is clear that whether the blue $^5D_3 \rightarrow {}^7F_J$ emission of terbium occurs in doped silica depends not only on the terbium concentration, but also on the nature of the excitation source.

A scheme for the energy levels of both the divalent and trivalent lanthanide ions in amorphous silica was proposed, based on a recent model. The value of the charge transfer excitation energy for Eu^{3+} was taken as the energy from the valence band to the f-level of Eu^{2+}, and the levels for other lanthanides were obtained by their known shifts relative to this. The suggested use of the charge transfer energy for Ce^{4+} to find the f-levels for Ce^{3+} and hence the other trivalent lanthanide ions did not yield good results.

Emission from Ce-doped silica was compared to the reported literature. Due to the nature of the amorphous host a wide variation was recognised. This represents a challenging system because of its defect emissions, the variability in wavelength of cerium's f-d transitions depending on the ion's environment and the possibility of Ce occurring in either the Ce^{3+} or Ce^{4+} charge state. The samples annealed in air showed emission under electron beam excitation, but not UV excitation. It is suggested that by electron beam excitation Ce^{4+} ions can be stimulated by a process of electron capture into excited Ce^{3+} ions which are responsible for the luminescence. The change in emission wavelength can then be attributed to the different environments of the Ce^{4+} and Ce^{3+} ions.

The influence of annealing atmosphere on the relative concentration of Ce^{4+} and Ce^{3+} ions was studied by x-ray photoelectron spectroscopy (XPS) and related to the PL characteristics. The XPS spectra analysis showed an increase of the Ce^{3+} concentration in the samples annealed in reducing atmosphere of 4% H_2 in Ar. Reducing the samples at 1000°C is much more efficient than 600°C. The PL and UV-vis reflectance measurements were consistent with the XPS results, confirming the successful conversion of non-luminescent Ce^{4+} to luminescent Ce^{3+}.

For Ce,Tb co-doped silica the quantum efficiency of the energy transfer from Ce to Tb can be maximised by annealing the samples in a reducing atmosphere. The optimum concentration of Ce ions giving a high emission from 1% Tb ions was found to be 0.5%, which is in a good agreement with the reported result from samples annealed at 600°C in

air. However, the enhancement of luminescence due to co-doping has been increased dramatically compared to these earlier results, indicating that the energy transfer quantum efficiency was strongly depended on the annealing atmosphere. Using such co-doped silica samples exhibiting energy transfer, it is possible to obtain effective luminescence from the Tb^{3+} ions via excitation of Ce^{3+} ions at 325 nm, instead of exciting the Tb^{3+} ions directly which requires a shorter wavelength of about 227 nm.

A series of Ce,Tb co-doped silica samples with a fixed concentration of Ce (0.5 mol %) and varying concentration of Tb from 0 up to 0.8 mol% were produced for studying the energy transfer mechanism. The measured donor emission characteristics (both intensities and lifetimes) as a function of co-doping concentration were fitted to the theoretical models, and the best fits were found for the exchange interaction model and the dipole-dipole interaction model. Due the large critical distance R_0 obtained from the fitting, the exchange interaction model was excluded and the energy transfer was attributed to dipole-dipole interactions.

Ce and Tb doped as well as Ce,Tb co-doped LaF_3 nano phosphor was produced successfully by the hydrothermal method. The XRD patterns exhibited no change in the crystal structure, except a small shift in the diffraction peaks to higher 2θ values in the samples having a heavy dopant concentration (due to the smaller size of the dopant ions than those they substitute). The estimated particle size was 36 nm. In the co-doped samples Ce emission was quenched and an enhancement in Tb emission was detected. Energy transfer from Ce to Tb was achieved in the co-doped samples with maximum quantum efficiency for energy transfer around 87% for the LaF_3:Ce(1%),Tb(20%) sample.

The intensity and lifetime of the donor as function of the acceptor concentration were analysed according to the theoretical models. On the basis of the analysis among the multipole interactions, the best fit was achieved if the energy is transferred via the quadrupole-quadrupole interaction. Due to the short enough effective average Bohr radius L calculated from the obtained fit parameters, the exchange interaction could not be excluded and it may contribute to the energy transfer together with quadrupole-quadrupole interaction.

The mechanism of the energy transfer found between Ce and Tb is different in the amorphous silica host and the crystalline LaF_3 host, indicating it is not simply dependant on the type of donor and the acceptor, but also their environment.

For future work, an effort can be made to solve the complication of the lifetime analysis in the sol-gel silica by trying to dope it with a smaller concentration of Ce, and also trying to control the host defects by preparing a crystalline phase of silica. This might be done using the combustion method.

From our analysis, the energy transfer mechanism differs in the two studied hosts, suggesting that the mechanism is not only dependent on the kind of the donor and acceptor. This suggests further investigations of other combination of donors and acceptors to confirm whether the mechanism is host dependant or not.